INTEGRATION OF SPECTRAL REMOTE SENSING DATA AND AIRBORNE GAMMA-RAY SPECTROMETRY FOR LITHOLOGICAL MAPPING OF VOLCANIC SEQUENCES IN EAST PILBARA GRANITE GREENSTONE TERRANE IN AUSTRALIA

DENSON MAKWELA

February, 2015

SUPERVISORS:
Dr. F.J.A, (Frank) van Ruitenbeek
Drs. J.B, (Boudewijn) de Smeth

INTEGRATION OF SPECTRAL REMOTE SENSING DATA AND AIRBORNE GAMMA-RAY SPECTROMETRY FOR LITHOLOGICAL MAPPING OF VOLCANIC SEQUENCES IN EAST PILBARA GRANITE-GREENSTONE TERRANE OF AUSTRALIA

DENSON MAKWELA
Enschede, The Netherlands, February, 2015

Thesis submitted to the Faculty of Geo-Information Science and Earth Observation of the University of Twente in partial fulfilment of the requirements for the degree of MASTER of Science in Geo-information Science and Earth Observation.
Specialization: Earth Resources Exploration

SUPERVISORS:
Dr. F.J.A, (Frank) van Ruitenbeek
Drs. J.B, (Boudewijn) de Smeth

THESIS ASSESSMENT BOARD:
Prof. Dr. F.D, van der Meer (Chair)
Dr. M.W.N, (Mike) Buxton (External Examiner, University Delft)

ABSTRACT

ASTER images and airborne gamma-ray data have been used in mineral exploration and geological mapping for many years. The full potential of its application in the greenstone terrane is not certain. This research aims at determining chemical and mineralogical variation that can be mapped by integration of ASTER and airborne gamma-ray datasets in the East Pilbara Granite Greenstone Terrane. The results will be useful in application of ASTER and airborne gamma-ray for similar terranes

In this research, chemical variations of potassium (K), thorium (Th) and uranium (U) that airborne gamma-ray could map, were assessed by comparing with whole-rock laboratory geochemical data produced by Smithes et, al., (2007) from same sampling points using box plots and spatially using deviation analysis. Ternary images were used to map out variations between lithology and integration with ASTER.

Furthermore, mineralogical variations that ASTER images could map were identified by measuring and studying reflectance spectra of wavelength 350nm to 2500nm on fresh and weathered rock samples collected by Smithes, et al., (2007) and Thuss, (2005) respectively from same area. Fresh samples were used to identify spectral detectable minerals while weathered samples were used to understand the effects of weathering. Mineralogical mapping was done using band ratio composite images. The ratios were selected based on its ability to highlight spectrally detectable minerals and discriminate lithological classes well. This was achieved by comparing band ratio pixel values of laboratory spectral that was resampled to ASTER.

The methods were applied to Coonterunah and Duffer transects as training samples for the study because of their good lithological variation while Apex, Panorama, Euro, North Star, Mt Ada and Charteris transects were used for validation. Results from transect were used to develop colour threshold for ASTER and airborne gamma-ray that were used to map the volcanic sequence. Integration of ASTER and airborne gamma-ray results used overlay analysis.

The results of this research show that K and Th better separate lithology classes than U. Variation in these radioelements enabled airborne gamma-ray to map the volcanic sequences into ultra-mafic, mafic, intermediate/felsic and intermediate/felsic altered. Although airborne gamma-ray was able to discriminate the volcanic sequences it is also being affected by survey parameter, pre-processing steps, instrument calibration and lithology surface area coverage.

Spectral analysis shows that detectable minerals are hornblende, actinolite, Mg-chlorite, epidote, intermediate chlorite, halloysite and illite. Hornblende can be linked to lithology characterisation. Weathering was found to be responsible for the formation of halloysite, illite, iron oxides and hydroxides. ASTER band ratios (5/3) + (1/2), (6+9)/8 and (7+9)/8 which highlight ferrous iron, amphibole and MgOH, and carbonate, chlorite and epidote respectively were found useful in mapping mineralogy. ASTER could map the volcanic sequence into ultra-mafic, intermediate/felsic and intermediate/felsic altered. Though ASTER was able to map mineralogical variation weathering affects its maximum potential to properly map lithology.

Integration of the two datasets proved that more precise lithological mapping could be achieved. Effects of weathering on ASTER lithological boundary could be corrected with airborne gamma-ray which improved the results. At a regional scale combined ASTER and airborne gamma-ray datasets can map the

East Pilbara Granite Greenstone Terrane into four classes; ultra-mafic, mafic and intermediate/felsic and intermediate/felsic altered.

ACKNOWLEDGEMENTS

All praise to God almighty who is faithful and merciful. I have no words to express my deepest sense of gratitude and numerous thanks to God who enabled me to complete my studies and this thesis work.

I am very thankful to my supervisors dr. Frank van Ruitenbeek and drs. Boudewjin de Smeth for their encouragement, tireless guidance and fruitful discussion that help me to shape my ideas and think scientifically. The knowledge they imparted will be put to practice.

To staff members of Applied Earth Science and ITC hotel I say thank you for making my study a success. I am greatly indebted to all my colleagues for being friends always and time we shared together during our study. Your company was a blessing.

I always feel the freshness in life due to the love of my parents as well as inspiration from the reminiscence and elevated wishes of my brothers and sisters and in-laws.

Finally I would like to thank my wife Elizabeth for love, encouragement, moral and spiritual support she has always given me. I dedicate this to her.

TABLE OF CONTENTS

LIST OF FIGURES

LIST OF TABLES

1. INTRODUCTION

1.1. Research Background

Reliable geological information is crucial for successful operations and development of mineral resource. Mining companies prefer investing in areas where geological information is up-to-date and readily available. This is aimed at increasing chances of mineral deposit discovery and optimizing exploration expenditure (Pablo and Palomera, 2004). Several tools have been used to gather geological information to optimize exploration expenditure since the 1900's. For example between 1994 and 2004, Geological Survey of Australia (GSWA) and Geoscience Australia (GA) undertook a mapping exercise of the East Pilbara Granite-Greenstone Terrane (EPGGT) at 1:100,000 scale. The study used conventional mapping techniques for this area of 40,040km^2. Tools used were field mapping, aerial photo interpretation, magnetics, radiometric, petrographic study and whole-rock laboratory geochemistry data analysis.

Studies have shown that in well exposed areas remote sensing techniques can be used for lithological mapping and their application reduces time and cost. (van der Meer et al., 2012). Furthermore, availability of digital image in remote sensing enables image enhancement and data integration there by extracting more information. For example Advanced Spaceborne Thermal Emission and reflection Radiometer (ASTER) is a multi-spectral sensor with 14 bands 3 bands (between 0.52 - 0.86µm with spatial resolution 15m) in Visible Near Infrared (VNIR), 6 bands (between 1.6 to 2.43µm with spatial resolution 30m) in Shortwave Infrared (SWIR) and 5 bands (between 8.125 to 11.65µm with spatial resolution 90m) in Thermal Infrared (TIR) (Abrams and Hook, 2001). Its images are used in geological studies because of its ability to distinguish Al-OH, Fe, Mg-OH, H-O-H, and carbonate absorption features using the SWIR and high spatial resolution compared to LANDSAT (van der Meer et al., 2012). Furthermore, the increased number of bands of ASTER allows for the extraction of more lithological detail (Zhang, et al., 2007).

Another remote sensing technique is airborne gamma-ray spectrometry. It makes use of gamma radiation levels of K, Th and U to evaluate lithology chemical variation and surface geomorphological processes. It also provides for image enhancement and integration. It has the ability to penetrate up to 30cm for rocks and 50cm for soil (Milsom and Eriksen, 2007) thus provide opportunity to overcome shallow overburden on lithology that may affects satellite imagery application. Interpretation of airborne gamma-ray works well in combination with mineralogical and geochemical data. This can provide insight in the mode of occurrence of radiometric elements and their heterogenetic association (International Atomic Energy Agency, 2003).

1.2 Problem Statement

Presence and discovery of volcanic-hosted base metals sulphides in the EPGGT has made greenstone belts (volcanic sequences) target for exploration (Barley, 1998). This influenced detailed studied of different rock units for alteration facies and metamorphism. Most studies use either conventional or remote sensing techniques. For example, alteration facies studies integrated remote sensing data and whole-rock laboratory geochemistry data to identify alteration minerals and zones (Anderson, 2003; Bayanjargal, 2004; van Ruitenbeek et.al., 2005; 2006) while geological mapping of the area used aerial photo interpretation, field notes and whole-rock laboratory geochemistry data (Van Kranendonk, 2003). In addition most of alteration studies were done to the Strelley belt.

Though remote sensing techniques have been used for mineral exploration in EPGGT, the extent to which airborne gamma-ray and ASTER datasets could be used to map chemical and mineralogical variation is not certain. Data integration is one of the commonly used means of extracting information. It has been used in many applications (Dickson et al., 1996; Eberle and Paasche., 2012; Ehlers et al, 1991). It is also not known whether integration of gamma-ray and ASTER and can improve chemical or mineralogical composition mapping of the volcanic sequence of EPGGT.

1.3 Motivation

The EPGGT are well exposed and lithology formation history is preserved. The rocks fractionates from mafic to felsic. These provide opportunity to test application of ASTER and gamma-ray datasets for chemical and mineralogical variation mapping.

1.4 Research Objectives

The main objective of this research is to determine whether ASTER satellite data and airborne gamma-ray spectrometry data can map chemical and mineralogical variation within the greenstone that are observed from rock samples collected in the field.

1.4.1 Specific Objectives:

1) To determine the variation in potassium, thorium and uranium in whole-rock laboratory geochemical data and compare this with airborne gamma ray data for these three elements.
2) To define to what extent airborne gamma-ray data can help in mapping chemical composition of the lithological formations in the EPGGT.
3) To determine the variation in spectral mineralogy of field measurement and ASTER satellite data.
4) To determine the added value of integrating airborne gamma-ray and ASTER data in the EPGGT for lithological mapping.

1.5 Research Questions

1) What correlation exists between airborne gamma-ray data and whole-rock laboratory geochemical data?
2) Which mineral significant for lithological characterization can be mapped using ASTER images in the volcanic sequence(s) of the EPGGT?
3) What geochemical details can airborne gamma-ray provide for mapping volcanic sequence of EPGGT?
4) Can more detailed information be obtained by integrating ASTER and airborne gamma-ray data for chemical and mineralogical mapping in the EPGGT?

1.6 Hypothesis

Integration of ASTER and airborne gamma-ray data can reduce part of the uncertainty in mapping mineralogy and chemical variations by providing complementary information on mineralogical and chemical composition and enhances mapping accuracy.

1.7 Datasets, Technical Aspects

This research uses airborne gamma-ray data collected by Australian Geological Survey Organisation (AGSO), laboratory whole-rock geochemical data collected by Smithes., (2007). ASTER images were collected by ASTER sensor on board Terra satellite and obtained from United States Geological Survey (USGS). Reflectance spectra measured from weathered and fresh surface of samples collected by Thuss (2005) from same location Smithies collected. Geological maps with explanatory notes produced by Geological Survey of Australia, Reflectance spectra collected by Abweny, (2012) from samples of Smithes et al., (2007) were used for interpretation.

1.7.1 Airborne Gamma-ray Spectrometry

Airborne gamma-ray spectrometry datasets are 50m cell size single element grids georeferenced in geographic coordinate WGS 84. The grid elements are Th, K and U. Grid is in ER Mapper format. Elements units of measurement are percentage for K and part per million (ppm) for Th and U. Each element grid was a combination of four airborne surveys that were flown and processed by Australian Geological Survey Organization (AGSO) in 1996. The project numbers were 648, 649, 651 and 656 covering Middle Pilbara, Marble bar Goldsworthy and east Pilbara respectively (Richardson, 2004). All surveys were semi detail and had following specifications;

Project number	**648**	**649**	**651**	**656**
Lines spacing	400m	400m	400m	400m
Tie spacing	4000m	4000m	4000m	40000m
Line direction from true north	180	90	180	180
Datum	WGS84	WGS84	AGD66	WGS84
Above Sea Level (ASL)	150m	280m	130m	300m
Above Ground level (AGL)	80m	80m	60m	80m

Table 1-1: Technical specification of airborne survey

1.7.2 ASTER Images

ASTER images were obtained as level 1B (pre-processed up to radiance values). The images had three wavelength regions of Visible and Near Infrared Region (VNIR), Shortwave Infrared Region (SWIR) and Thermal Infrared Region (TIR).

1.7.3 Laboratory Whole-rock Geochemical Data

206 rock samples were collected from different transect and analysed by Smithes, (2007). Samples are fresh and collected across lithological strike to identify geochemical characteristic. This research used 178 samples from Coonterunah, Duffer, Euro, Mt Ada, Apex North star, Chateris and Panorama transects (Figure 1-1). Analysis was made for major and trace elements. Major element compositions were determined using wavelength dispersive XRF spectrometry. Precision is better than 1%. Loss on ignition (LOI) was determined by weighing after heating at 1100^{o}C. FeO was determined by titration. The major elements reported and used are; SiO_2, TiO_2, Al_2O_3, FeO, Fe_2O_3, MgO, CaO, Na_2O, K_2O, P_2O_5 in percentage.

Trace elements used for this research are Th, U, Nb, Y and Zr and were analysed using Inductively Coupled Plasma Mass Spectrometry (ICP-MS) after four steps of acid decomposition. Units are given in part per million (ppm) (Smithes et al., 2007).

1.7.4 Rock Reflectance Spectra

A total of 178 samples were studied measuring 271 rock reflectance spectra of which 171 were measured from fresh surface and 100 from weathered surface of samples collected by Thuss, (2004) and by Smithes, (2007) form transects where lithologies formations are well exposed (Figure 1-1 and 1-2). Furthermore, reflectance spectra measured by Abweny (2012) from samples collected by Smithies were used for comparison and interpretation. Both dataset measurements were done using Analytical Spectral Device (ASD) Fieldspec Pro spectrometer with a spectral wavelength of 350nm - 2500nm (VNIR – SWIR). Each spectrum is an average of three measurements from same sample on different locations.

1.7.5 Geological Maps and Explanatory Notes

Geological maps originally prepared at a scale of 1:100,000 with explanatory notes were used in interpretation. The notes account for general geology, stratigraphy, orogenic revolution, geochronology and mineral occurrence.

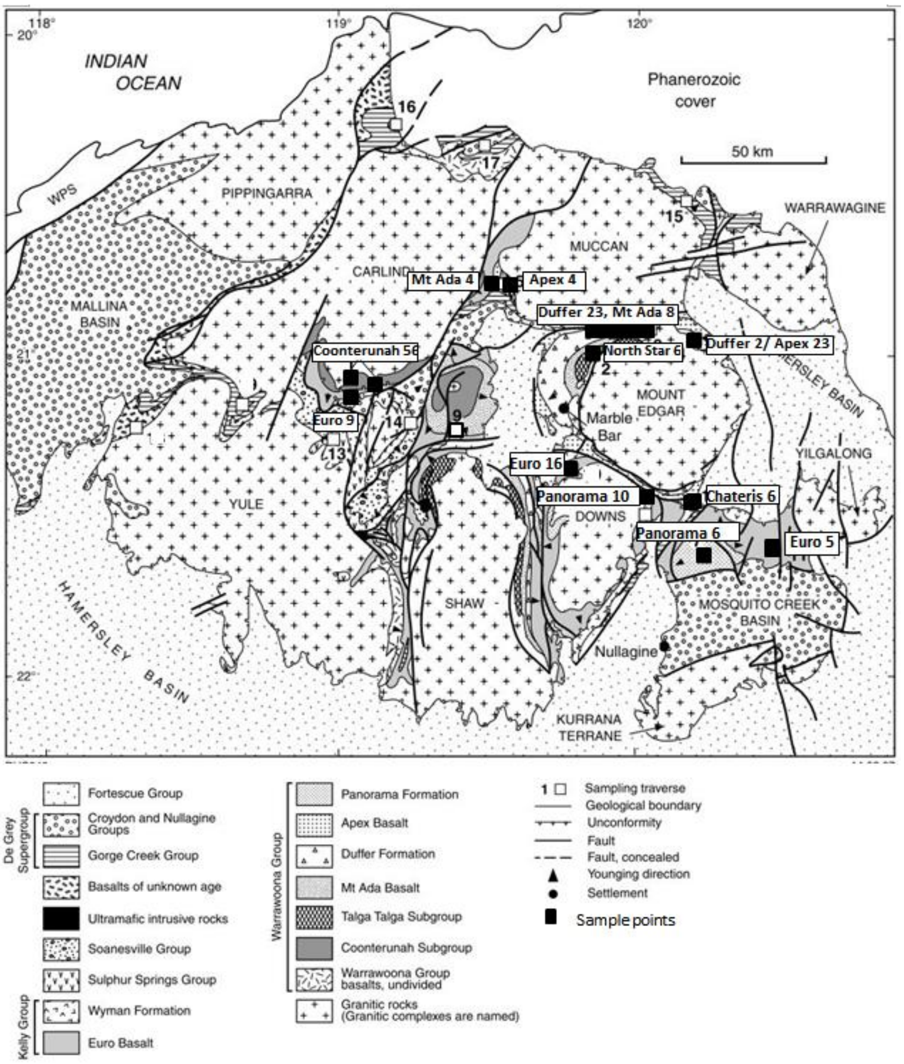

Figure 1-1: Study area location and sampling points (modified after Smithes et al., 2007)

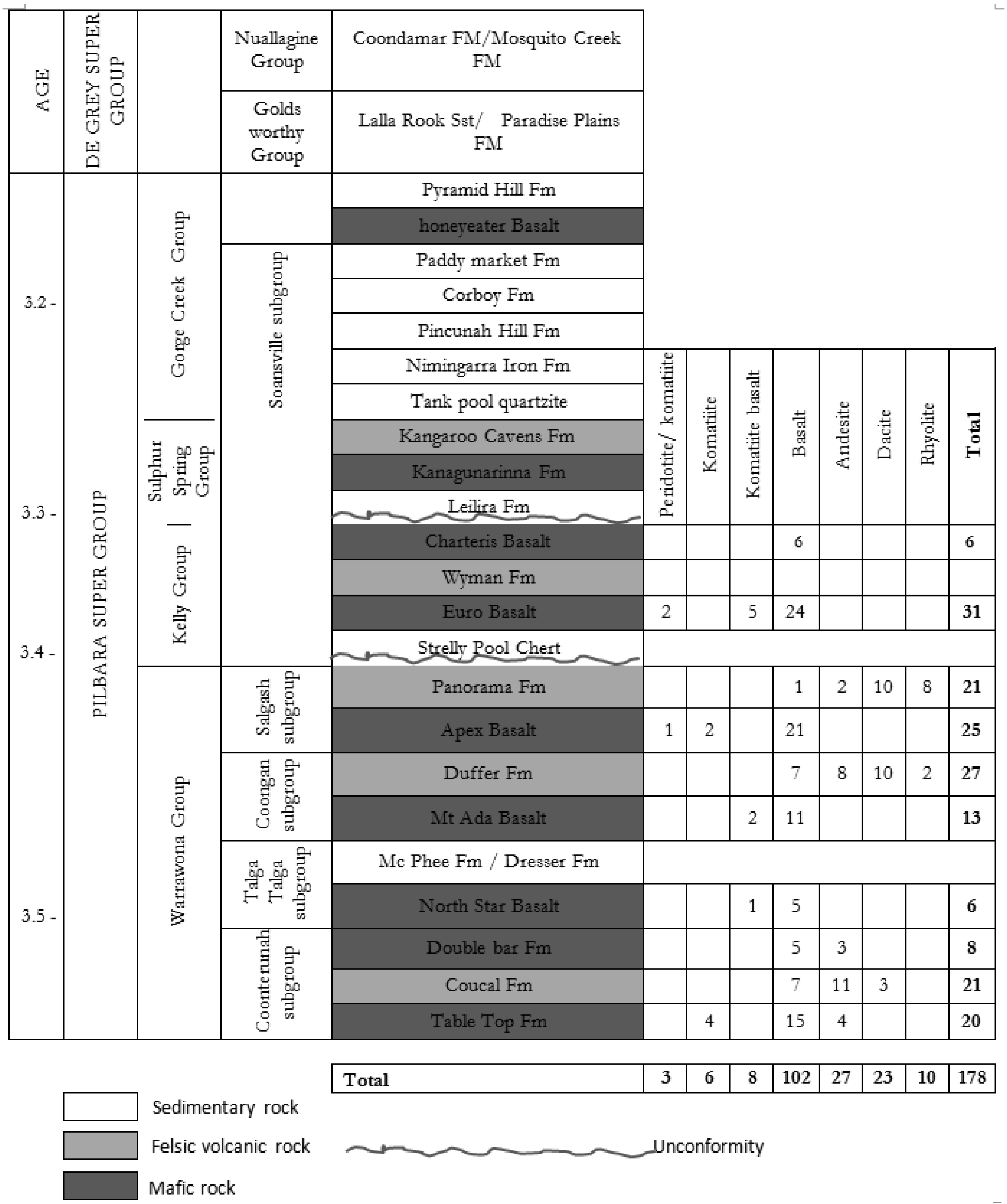

Formation	Peridotite/ komatiite	Komatiite	Komatiite basalt	Basalt	Andesite	Dacite	Rhyolite	Total
Charteris Basalt				6				6
Wyman Fm								
Euro Basalt	2		5	24				31
Panorama Fm				1	2	10	8	21
Apex Basalt	1	2		21				25
Duffer Fm				7	8	10	2	27
Mt Ada Basalt			2	11				13
North Star Basalt			1	5				6
Double bar Fm				5	3			8
Coucal Fm				7	11	3		21
Table Top Fm		4		15	4			20
Total	3	6	8	102	27	23	10	178

Figure 1-2 Generalised lithostratigraphy of EPGGT with rock name and number (modified after Abweny, 2012)

1.8 Thesis Structure

CHAPTER 1: Introduction

- Describes the background, problem definition, objectives, questions, and dataset of the research

CHAPTER 2: Literature Review

- Describes previous works done in the study area with regards geology and remotes sensing, methods and techniques.

CHAPTER 3: Methodology

- Describes methods used in data analysis in this research.

CHAPTER 4: Results and Discussion

- Show and discuss the results of the analysis.

CHAPTER 5: Conclusion and Recommendation

- It synthesise the research findings and make recommendation to the findings of the research.

2. LITERATURE REVIEW

2.1. Regional Geology.

The Pilbara craton is divided into three major Archean terranes that show distinct geological features. The East Pilbara granite-greenstone terrane (3.72 to 2.85 Ga), West Pilbara granite-greenstone terrane (3.27 – 2.92 Ga) compose of Karratha, Sholl, and Regal terranes and Kurrana terrane <3.29 Ga (Figure 2.1) (Hickman and Kranendok, 2006; Van Kranendonk et al., 2002). All terranes are overlain by De grey super basin (3.02 to 2.93 Ga). The carton is believed to have formed from mantle plume events that resulted in eruption of thick dominantly basaltic volcanic after melting the crust (Hickman and Kranendonk, 2006; Van Kranendonk et al., 2007). This was accompanied by uplift and crustal deformation. The East Pilbara granite-greenstone terrane forms the nucleus of the craton and was formed in three distinct mantle plumes 3.4, 3.35 - 3.29 and 3.27 – 3.24 Ga. Uplift and crustal deformation were as a result several tectonic activities including granitoid intrusions between 3.500 – 3.165 Ga.

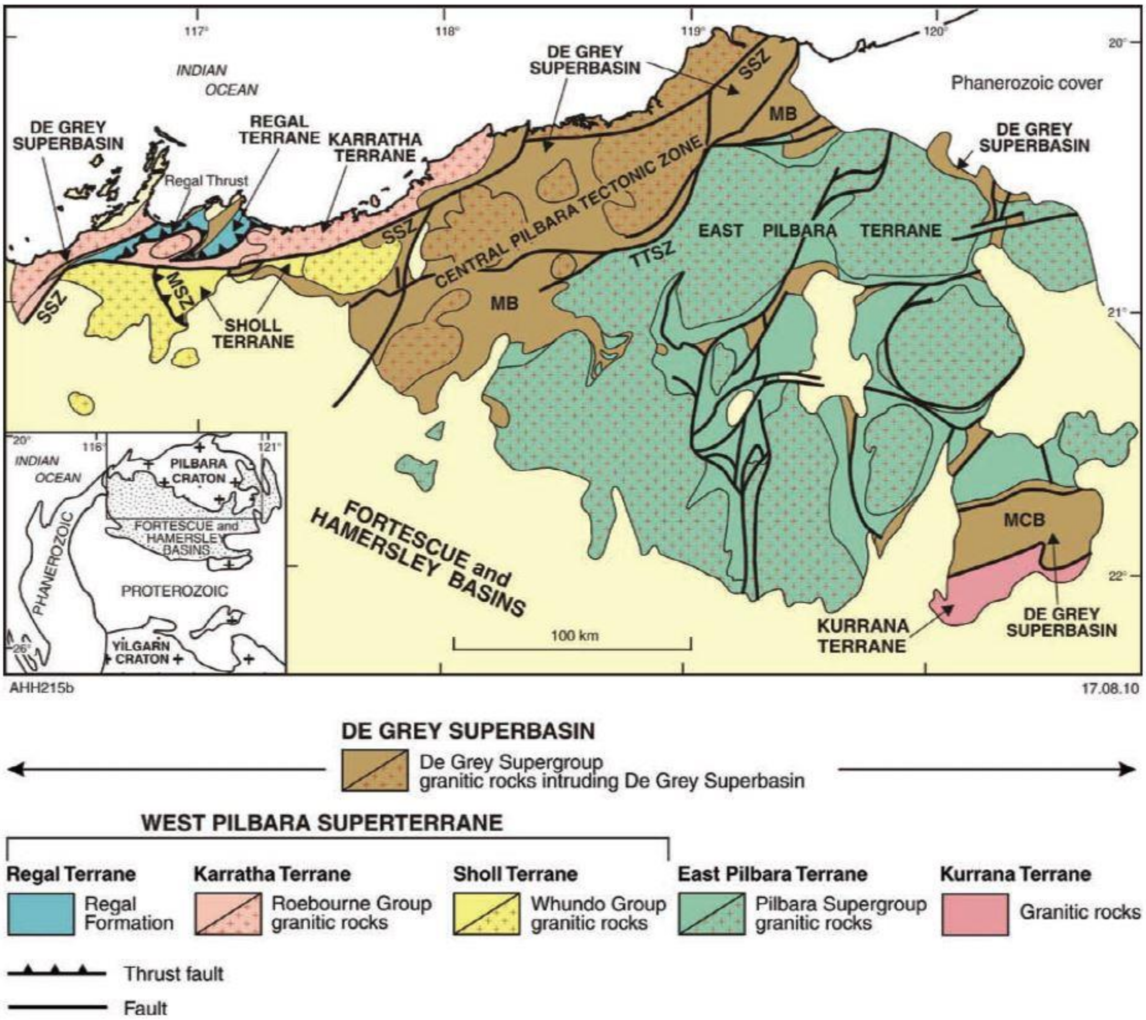

Figure 2-1: Simplified geology of the northern Pilbara carton, showing terranes and the De Grey super basin (after Hickman and Kranendonk, 2006).

2.2 Geologic Setting and Stratigraphy of the East Pilbara Granite-Greenstone Terrane (EPGGT) Volcanic Sequence.

The East Pilbara granite-greenstone terrain volcanic sequences are bounded by fault, intrusive and sheared intrusive contacts with five major granitic super suites (Figure 2.2) and are grouped into four sub group; Warrawoona, Kelly, Sulphur Spring and Soanesville (Hickman, 2006). These groups are composed of interlayered mafic and felsic rock. In addition, Warrawoona and Kelly are separated by Strelley Pool Formation while the Kelly and Sulphur Spring are separated by Leilira Formation. Both Strelley and Leilira formation were aerial deposited signifying a pause in volcanism. (Figure 2.3) In both cases, the pause in volcanic activity was followed by folding causing deformation and metamorphism. Metamorphism reached conditions of the amphibolite and greenschist facies (Van Kranendonk et al., 2006).

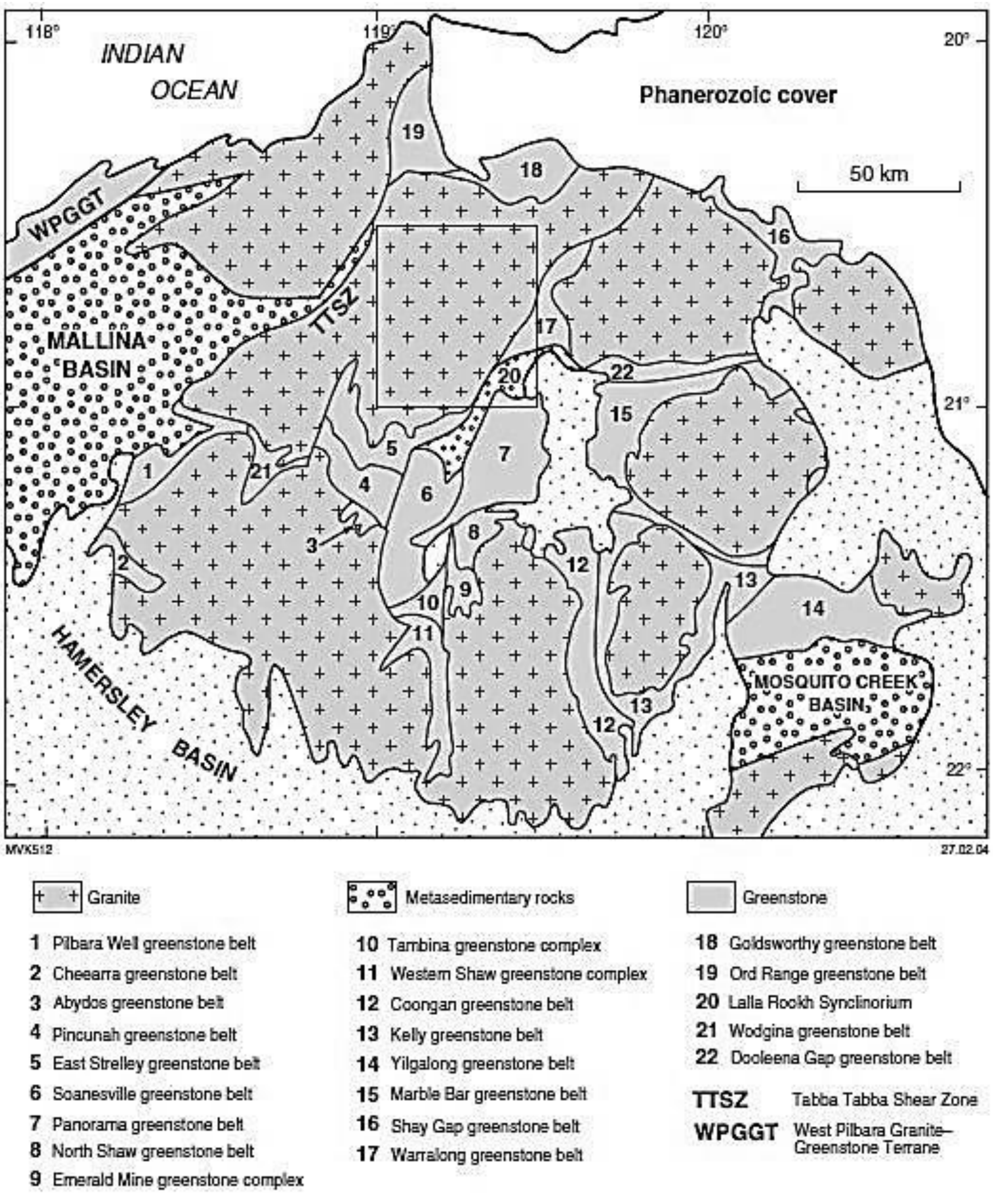

Figure 2-2: Greenstone belts (Pilbara supergroup) granitic complexes and sedimentary supergroup of East Pilbara granite-greenstone terrane (After Van Kranendonk et al., 2002).

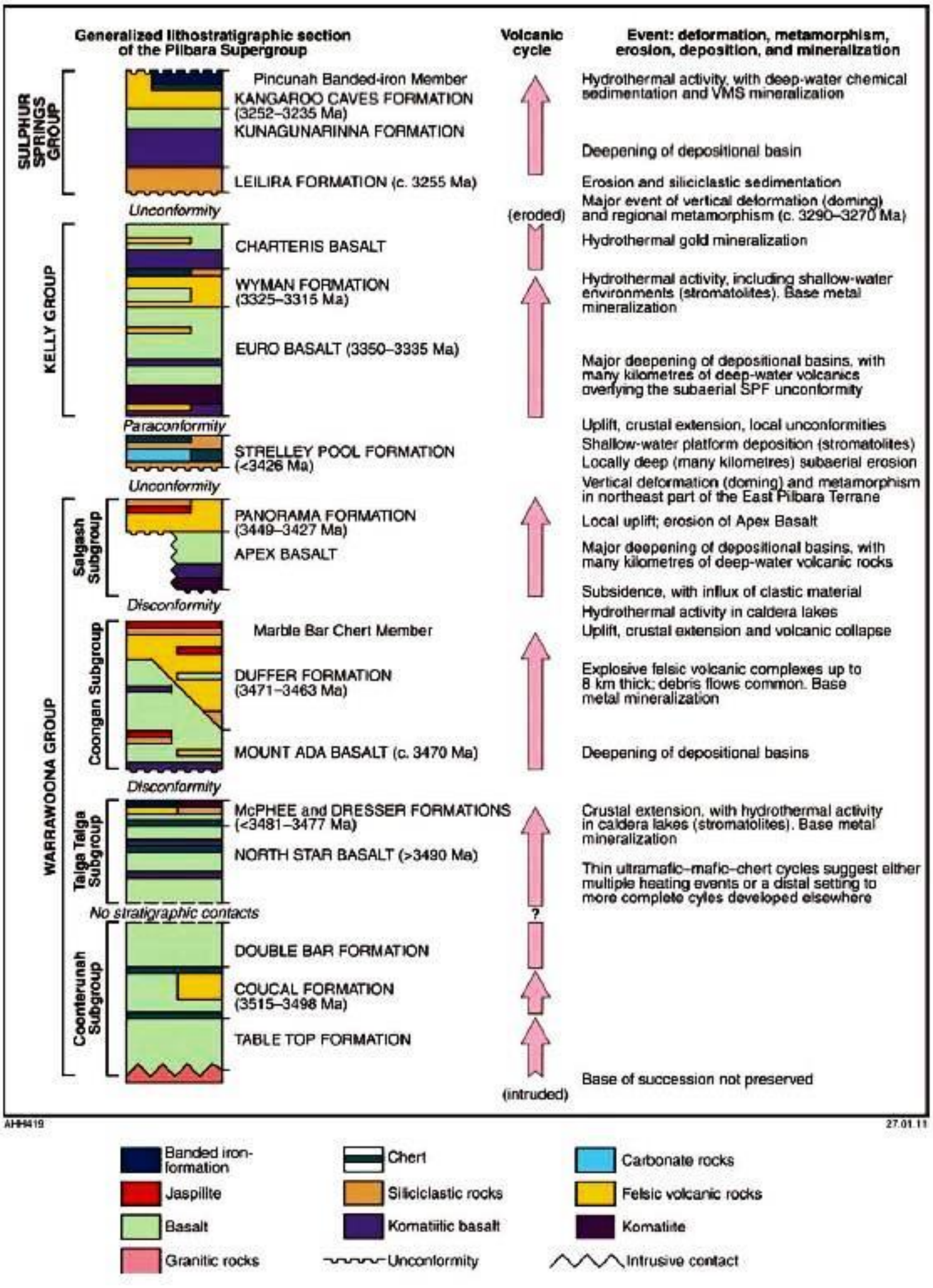

Figure 2-3: Generalise stratigraphy of the predominantly volcanic Pilbara Supergroup, which is represented in almost all greenstone belts of the East Pilbara Terrane (after Hickman, 2011).

2.3 Formation Description

In this research, only the Warrawona and Kelly groups will be described in detail per subgroup and formation together with granitoid intrusions that affected the groups.

2.3.1 Warrawona Group

The Warrawona group is sub-grouped into four; Coonterunah, Talga Talga, Coongan and Salgash. The subgroups are further grouped into formations.

2.3.1.1 Coonterunah Subgroup

The Coonterunah subgroup (3515 Ma) forms the oldest rock in the study area. It is at the bottom of the Warrawoona group. Coonterunah subgroup is composed of mafic and felsic volcanic that were intruded by the Carlindi granitoid batholith. It is located to the southern margin of the Carlindi granitoid batholith within the East Strelley greenstone belt (Van Kranendonk, 2000). The rocks are at amphibolite to upper-greenschist metamorphic grade due to intrusion of the Carlindi granitoid. The Carlindi granitoid complex is a calc-alkaline (TTG) suite that is largely composed of homogeneous, strongly foliated and folded intrusion of hornblende monzogranite (AgLmh) representing final stages of cratonisation (Bickle et al., 1989; Van Kranendonk, 2000, 2004). Within the Coonterunah formation the granitoid intrusion composition vary from hornblende monzodiorite to hornblende monzodiorite to hornblende monzogranite. The hornblende is retrogressed to epidote-chrolites and minor titanite and plagioclase is altered to sericite and epidote. (Van Kranendonk, 2004)

Structurally and stratigraphically the Coonterunah subgroup has three formations, Table Top Formation (AOt), Coucal Formation (AOci, and AOcbi) and Double Bar Formation (AOd) (Appendix 1). The Table Top Formation is the oldest and composed of fine grained doleritic to gabbroic intrusion (AOt) with subordinate pillowed and variolitic flows, gabbro and thin flow of high Mg basalt near its base. The base of the formation is in contact with the Carlindi granitoid that intruded it forming amphibolite schist's with well-developed foliation and lineation defined by elongated crystals metamorphosed hornblende and plagioclase. The schist's exhibit screens of bleached and silicified metabasalts near the contact with Carlindi granitoid. The formation is also intruded by massive feldspar and quartz-porphyritic rhyodacite (AOcfrp) representing sub volcanic sill (Van Kranendonk, 2000).

Overlying conformably the Table Top formation is the Coucal Formation whose base is composed of thick beds of cherty iron–formation (AOci). Along the southern margin of the Carlindi granitoid complex the Coucal Formation is composed of fine grained doleritic andesite and basalt (AOcbi). It is considered a transition zone between Table Top and Coucal Formations. The felsic volcanics rocks of the Coucal Formations are dacite and pumiceous rhyolite which were affected by metamorphic recystallisation and carbonate-sericite alteration. Amygdales in dacitic rocks are filled with carbonates and epidotes (Van Kranendonk, 2000).

The Double Bar Formation (AOd) is the youngest in the Coonterunah Formation. It is mainly composed of fine-grained tholeiitic basalt and basaltic pillowed tholeiitic basalt and interbedded volcanic clastic rocks. Almost all mafic minerals in this formation were recrystallised to metamorphic mineral assemblage of chlorite or actinolite-chlorite-ziosite- epidote- opaque minerals (Van Kranendonk, 2000).

2.3.1.2 Talga Talga Subgroup

The Talga Talga subgroup dates between 3490 and 3477Ma and overlays the Coonterunah subgroup. It is also a bimodal mafic and felsic volcanic and sedimentary deposit thus; North Star Basalt (349 ±15 Ma) and McPhee/Dresser Formation respectively. The North Star Basalt Formation forms the base of the subgroup and is exposed in the Warralong greenstone belt. It is composed of tholeiitic, massive and pillowed metabasalt, metakomatitic basalt, sepentinised peridotite, thin sedimentary layers of chert including siliceous iron formation. The North Star Basalt also has numerous dolerites and gabbro sills. It is intruded by Muccan and Mount Edgar granitoids in Warralong and Marble Bar greenstone belts respectively. Both granitoids are sub calc-akaline suites (Van Kranendonk, 2010).

The McPhee/Dresser Formation overlay the North Star Basalts in Marble Bar, Warralong and Panorama Formations. The formation is metamorphosed to greenschist facies at the top part, whereas the bottom is amphibolite facies. The major rock units are fine to medium grained meta basalt (AWhba), medium to coarse grained talc-chlorite carbonate schists (AWhu), and carbonate altered chlorite meta basalt (AWhbc) (Van Kranendonk, 2010 and 2000).

2.3.1.3 Coongan Subgroup

The Coongan subgroup overlay the Talga Talga subgroup and is composed of Mount Ada Basalt (3469 ±3 Ma) and Duffer (3474 – 3463 Ma) Formations which are mafic and felsic deposit respectively (Van Kranendonk et al., 2006). Mount Ada Basalt Formation is 2460m thick and composed of pillowed, massive basalt (AWmb) and komatiitic basalt (AWmbk) with pyroxene spnifex texture, felsic and mafic meta-volcanoclastic and thin chert rocks. The basalt is weakly metamorphosed to greenschist facies. The upper part of the Mount Ada Basalt Formation in the Marble Bar greenstone belt is marked by mafic rock with less felsic volcaniclastics (AWmbt) intercalated with milky grey chert. Furthermore, the formation overlies either the McPhee or Dresser Formation in different greenstone belts (Van Kranendonk et al., 2007).

The Duffer Formation conformably overlies Mount Ada Basalt Formation and is composed of metamorphosed volcaniclasitcs and flow of dacitic to rhyolitic rocks (AWdfx). The lower half of the formation from the bottom it has thin beds of fine grained felsic volcanic rocks (AWdft), coarse grained phyric dacite-andesite sills (AWdfdp) and pillowed andesitic basaltic rocks (AWdb). It also has pillowed-tholeiitic basalt and layered sedimentary metachert belonging to Marble Bar and Chanaman Pool Chert member. Furthermore, Feldspar-porphyritic sub volcanics intrusions are also common (Van Kranendonk, 2010).

2.3.1.4 Salgash Subgroup

The Salgash subgroup dates between 3458 Ma and 3426 Ma (Van Kranendonk et al., 2006) and overlies the Coongan subgroup marking the end of the Warrawona group. It is comprised of mafic Apex Basalt Formation and felsic Panorama Formation. The Apex Basalt appears in the Marble Bar and Warralong belts disconformably overlaying the Duffer Formation of the Coongan subgroup. The Apex Basalt Formation is overlain by either Panorama or Euro Basalt Formations in the Marble Bar greenstone belt and is intruded by Mount Edgar granitoid. The Apex Basalt rocks are fine grained tholeiitic and high Mg basalt (AWa) interlayered with metasedimentary rocks. The rocks are actinolite-plagioclase assemblage with minor chlorite and epidote. In the Warralong greenstone belt it consists of metamorphosed pillowed komatiitic basalt (AWabk) characterised by pale green schists composed of tremonlite–chlorite-serpentine mineral assemblage (Van Kranendonk, 2010).

The Panorama Formation (3456 Ma) forms the basement of the Kelly greenstone belt and is intruded by the Corunna Downs granitoid. It overlies the Apex Basalt Formation marking the close of Warrawona group. The formation consists of a succession of metamorphosed felsic volcanoclastic rocks with silicified tuffaceous volcaniclastic rocks and volcanic breccia. The top of the formation has tuffaceous units (AWpft) which are crosscuted by hydrothermal veins and dykes of black chert. In the Marble Bar greenstone belt the Panorama Formation thin eastwards and is marked by discontinuous lenses. The felsic rocks are altered, siliceous, porphyritic and fine grained rhyolite to dacite tuffaceous. Quartz and altered feldspar occurs as phenocryst where as rutile, zircon, chlorite and leucoxene are accessories. In the McPhee greenstone belt the formation consists of felsic volcaniclastics rocks with felsic lava and chert and interbedded with andesitic basalt (AWpfa) the main secondary minerals are sericite, carbonates, epidote and chlorite after hornblende. In the Panorama greenstone belt it is composed of massive weathered rhyolite (AWpr) (Van Kranendonk, 2000 and 2010).

2.3.2 Kelly Group

The Kelly group has no subgroup but rather formation. It is separated from the Warrawona and Sulphur Spring groups by aerial deposits, Strelley Poor Chert and Leilira Formations. The Strelley Formation conformably overlay the Panorama Formation and is composed of white and grey layered cherts (AWs). Its silicification is recent evidenced by identical textual features (Van Kranendonk, 2000).

The Euro Basalt Formation (3350 – 3325 Ma) conformably overlay the Strelley Pool Formation in the East Strelley, Panorama and North Shaw greenstone belts while in the Kelly greenstone belt, the Euro basalt unconformably overlies the Panorama Formation. The Euro Basalt Formation is composed of pillowed basalt of interbedded tholeiitic units and high Mg-basalt (AWebm). It also has basaltic komatitie and thin beds of intercalated chert with felsic volcaniclastics. In the Kelly and McPhee greenstone belts, the Euro Basalt is composed of metamorphosed komatiitic basalt, metadolerite and pillowed tholeiitic basalt (A-KEe-bbo). The base is mostly komatiitic (A-KEe-bk) with tholeiitic basalt consisting of albite, tremolite, epidote, chlorite, quartz and titanite with clinopyroxenes. The Euro Basalt consists of mainly basalts and mafic schist, gabbro chert clastic sediments and ultramafic rocks. Intrusion of Yalgalong granitoid on the Euro basalt resulted in metamorphism of the komatiitic basalt (AWebk) and formation of mafic schist (AWbs) (Van Kranendonk, 2000).

Charteris Basalt Formation overlays the Wyman Formation and is located in the Kelly greenstone belt and only appears in the Charteris creek. It is also overlain by the Budjan Creek Formation; the Charteris is composed of metamorphosed tholeiitic basalt (AWcbk) with interlayered thin dolerite and komatiitic basalt containing chlorite after pyroxenite.

2.4 Spectral Remote Sensing Studies

Most of the work done in the volcanic sequences of EPGGT has showed that it is possible to use spectral remote sensing techniques. Abweny, (2012) used reflectance spectra data of wavelength range 350-2500nm measured from fresh surfaces to characterize metamorphic grade. His results shows three subfacies within the greenschist facies based on spectral mineral assemblages such as Fe-chlorite; intermediate chlorite + epidote; and intermediate chlorite + actinolite + hornblende. The study also identifies that Hornblende, Mg-chlorite and sericite relates to lithological composition discriminating ultramafic, high Mg-content basalt and felsic rocks respectively.

Bayanjargal, (2004) showed that integration of satellite imagery and airborne gamma-ray can be used for alteration mapping while Anderson, (2003) showed that Th and K can be used to differentiate rocks of volcanic sequences in the EPGGT. Most of spectral techniques applied in the volcanic sequences were meant to study different alteration facies mainly to the Strelley greenstone belt (Anderson, 2003; Bayanjargal, 2004; van Ruitenbeek et al., 2006; van Ruitenbeek et al., 2012).

2.5 Geochemical Studies

Smithes, (2007) studied the chemical composition of the rocks in EPGGT to characterize the lithological composition range of the volcanic rock types and determine if there is any systematic composition. Samples were collected from fresh surfaces across lithological formations. The results of the study suggest large chemical overlap for lithology with regards to major elements studies. Trace elements were used to classify the rocks as Ultramafic (komatiite/komatiitic basalt), mafic (basalt) and intermediate and felsic (andesite/dacite rhyolite).

In the Warrawona group komatiite at the lower part of Table Top Formation have high SiO_2 values ranging between 45% to 49.4 wt%, MgO from 22 to 30 wt% and a flat normalised trace element. Al is undepleted (Nesbitt et al., 1977). The upper part of Table Top formation is dominated by basalt with higher concentration of more highly incompatible trace elements (Th, U, Nb, and Zr) and light rare earth elements. This is considered as transition zone with the Coucal formation (Smithes et al., 2007).

The Coucal Formation is composed of two mafic to felsic series of rocks which are not readily distinguished in the field. It has andesite to dacite (C-F1) with silica range of 55 – 65 wt% and basalt to andesite (C-F2) with silica range 47.5 to 57.5 wt%.

North Star, Apex and Mt Ada Basalts are high in Ti and they overlap extensively with the Coonterunah basalts. The North Star basalt values for La/Yb and La/ Nb extends more than 1.74 and 1.65 respectively (Smithes et al., 2007).

Duffer Formation is characterised by minor rhyolite which is highly fractionated tholeiite (D-F1) with silica range of 68 to 75 wt%. It has highest Fe_2O_3 ranging from 2.7 to 4.6 wt%. Other subclasses of the Duffer Formation are voluminous mafic to felsic rock series (D-F2) with silica range 51.8 to 65 wt% and voluminous mafic to felsic rock with enriched trace elements (D-F3) with silica range of 52.4 to 68.8 wt%. Almost all major elements overlap for D-F2 and D-F3 except Al_2O_3 which is high for rocks with silica value more than 55 wt% and are sodic (Smithes et al., 2007).

Panorama formation has the highest silica range within Warrawona main group. Silica ranges from 72.7 to 87.5 wt%.

3. METHODOLOGY

3.1 Introduction

This research used whole-rock laboratory geochemistry data to classify lithology and study chemical variation of K, Th and U for airborne gamma-ray data. Ternary composite images of K, Th and U were used to map chemical variation of the volcanic sequence of the EPGGT. Laboratory rock reflectance spectra were used to identify spectrally detectable minerals that ASTER can detect and study the effects of weathering on the volcanic sequences. ASTER images were used to establish mineralogical variation that could be mapped. Mapping product from ASTER and airborne gamma-ray were integrated to determine extra information that could be generated. Visual interpretation was used to assess the added values. Geological map was used a base for mapping (Figure 3-1).

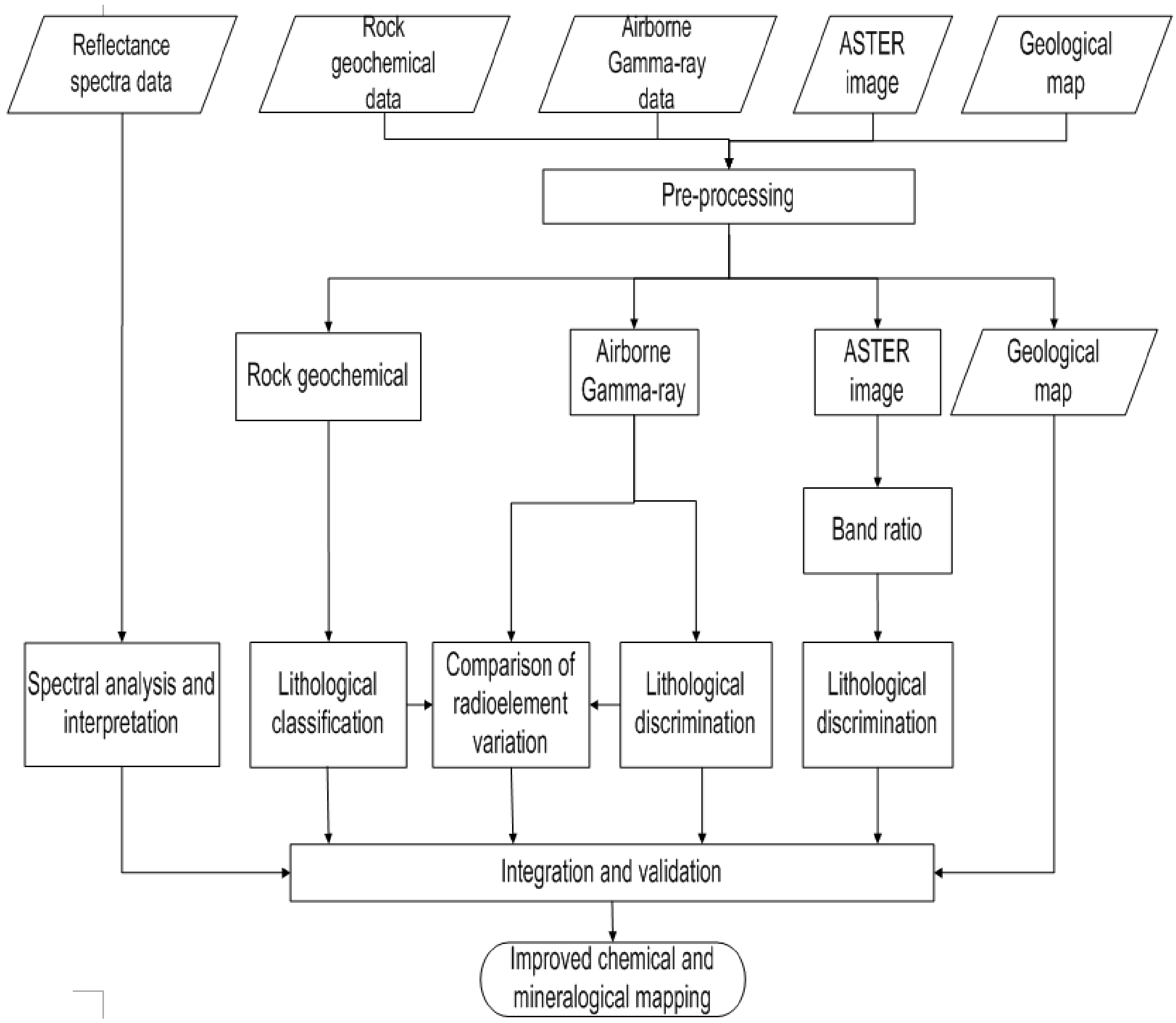

Figure 3-1: Research methodology flow chart.

3.2 Laboratory Whole-rock Geochemical Data.

Rock samples were available which were originally collected and analysed by Smithes, (2007). These samples are fresh and collected across lithology. Analysis was made by Smithies for major and trace elements. Major element compositions were determined using wavelength dispersive XRF spectrometry with a precision better than 1%. Loss on ignition (LOI) was determined by weighing after heating at 1100^{o}C. FeO was determined by titration. Trace elements were analysed using Inductively Coupled Plasma Mass Spectrometry (ICP-MS) after four steps of acid decomposition. (Smithes et al., 2007)

3.2.1 Exploratory Data Analysis

Firstly, exploratory data analysis was done to each transect to understand the nature of the dataset. Raw data was inspected for measurements error. Outliers were replaced with averages from its surrounding measurements for each variable. Data distribution was assessed through histogram and summary statistics.

3.2.2 Lithological Classification

Field classification and description of the lithology were verified by computing lithological indices. There are several lithological indices that are commonly used to classify igneous rocks. Some of them are K_2O - SiO_2, Na_2O + K_2O and Log Zr/TiO2 vs Log Nb/Y. These indices classify igneous rocks into basalt, basaltic andesite, andesite, dacite and rhyolite and volcanic series of tholeiitic calc-alkaline, and high-K calc-alkaline (Hastie, et al,. 2007). This research used Na_2O + K_2O plot to classify lithology as it is suitable in low grade metamorphic environment (Ghatak, et al,. 2012). This was done using Statistical Package for the Social Sciences (SPSS). Furthermore, this indices was suitable for the area because silica variation are reported to be higher than normally expected (Smithes, et al., 2007). This provides good visualization of variation among lithology classes (Figure 4-1).

3.3 Airborne Gamma-ray.

Airborne gamma-ray grids of Th, K and U were firstly, projected to Australian datum (GDA94_zone 50 and 51) and re-gridded from 50m to 15m cell size in Oasis Montaj 6.4.2. Gridding used nearest neighbour interpolation function to preserve cell values. Using ARGIS 9.2 point values measurement for Th, K and U were extracted from each element grid using laboratory whole-rock geochemical sampling points coordinates for proper comparison with laboratory whole-rock geochemical measurements. As mention earlier in section 1.1 that airborne gamma-ray can penetrate up to 50cm, proper interpretation of data also depend on understanding of surface processes and relief influence. This was achieved by comparing measurement values along transect with relief.

3.3.1 Ternary Map

Ternary composite images of K, Th and U were computed for mapping chemical variation between lithologies and data integration this was done using Oasis Montaj 6.4.2 software. Tone variation was the main feature that was used for lithological discrimination when mapping. Histogram equalisation was applied when computing maps for a good tone variation. The red, green and blue channels were assigned to K, Th and U respectively. This implied that high areas in red, green and blue on a map would mean high concentration of K, Th and U respectively while those in White would mean high concentration of all three radioelements.

3.4 Laboratory Whole-rock Geochemical and Airborne Gamma-ray Chemical Variation

Box plots, Scatter plots, and linear regression were used to study K, Th and U variations between measurements from whole-rock laboratory geochemistry and airborne gamma-ray spectrometry using Statistical Package for the Social Sciences (SPSS). Reported K measurement units were unified by converting whole-rock laboratory geochemical weighted percentage (w%) to molar percent by dividing measured value of K_2O for each sample by a conversion factor 1.205. Box plots were used to study how well K, Th and U measured from airborne gamma-ray could separate lithology classes compared to whole-rock laboratory geochemical data. Box plots were chosen because of it provide good visualisation.

Scatter plots were used to assess spatial association of each variable for the two data sets. Bivariate correlation was computed for each element using a Pearson product moment with a correlation coefficient at 95% confidence interval. Linear regression of 1:1 at 45 degrees was use to establish how much of airborne gamma-ray could be explained by laboratory whole-rock geochemical data and possible causes of discrepancies in measurement values of airborne gamma-ray. In this case laboratory whole-rock geochemical data is considered a true measurement value. Furthermore, profiles are used to assess the effects of relief of airborne gamma-ray measurements.

3.5 Rock Reflectance Spectra

The research uses Laboratory rock reflectance spectra as ground thruthing tool to properly understand what ASTER images could map. Reflectance spectra from fresh rock surface samples were used to identify mappable mineral while weathered rock surface spectra was used to study the effects of weathering (Figure 3.2).

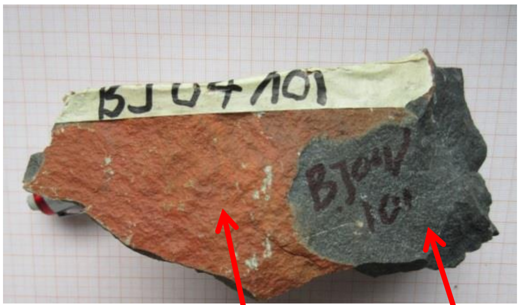

Weathered surface in brownish due to goethite and hematite

Fresh surface

View of Panorama area (source: google earth)

Figure 3-2: Sample with weathered and fresh surface and topographic view of part of the study area.

Six measurements were taken on each rock sample surface using ASD Field-spec-pro spectrometer (wavelength 350 to 2500 nm) (VNIR – SWIR), splice corrected and exported to ENVI. Three of the measurements were from fresh surface and another three from weathered surface. Average spectra for each surface were computed. Spectral libraries for fresh and weathered spectra were generated and exported to The Spectral Geologist (TSG), version 3 for mineral identification.

The Spectral Geologist software uses a wave form analysis to identify minerals automatically by matching sampled spectra with its library spectra. It normally gives out two possible results. The results from TSG were verified by manually re-interpreting spectra in ENVI basing on ENVI spectral library and the GMEX booklet associated with TSG. Furthermore, fresh surface results were also compared with those produced by Abweny, (2012) for the same area using the same method.

Characteristics that were studies were wavelength position of diagnostic position, shape of diagnostic or absorption feature (relative depth of absorption, relative peak of reflectance, width of the feature and deflection in main absorption feature). These features reflect on chemical composition and mineralogy of a rock (Clark, 1999). Interpreted spectra were further resampled to ASTER to identify spectral absorption features that persisted ASTER for further processing.

3.6 Advanced Spaceborne Thermal Reflectance Radiometer (ASTER)

ASTER image analysis for mineralogical mapping was mainly based on band and composite ratios. Ratios of laboratory spectra that were resampled to ASTER were computed and compare its band pixel values using box plots. Comparison using pixel values was best because ASTER and ASD calibration are different making their spectral curves not comparable. Ratio that highlighted well detectable minerals and separate lithology classes were selected for mineralogical mapping. Mapping used band ratio composite images.

Commonly used band ratios adapted from Kanlinowsk and Oliver, (2004) were computed for the VINR and SWIR region to highlight Al-OH and Fe and Mg-OH minerals.. TIR ratios were computed to identify silica variation between lithologies. The effects of weathering on ASTER image were assessed by highlighting clay mineral distribution (Table 3.1 and 3.2). The ratios were interpreted visually using image classification elements. Colour was the main elements used.

FEATURE	BAND RATIO	REFERENCE
Iron		
Ferric Iron Fe^{3+}	2/1	Rowan; CSIRO
Ferrous Silicates	5/4	CSIRO
Ferrous iron Fe^{2+}	5/3 + 1/2	Rowan
Carbonates/mafic minerals		
Carbonates/Chlorite/Epidote	(7+9)/8	Rowan
Epidote/Chlorite/Amphibole	(6+9)/(7+8)	CSIRO
Amphibole/MgOH/	(6+9)/8	Hewson
Silicates		
Clay	$(5x7)/6^2$	Bierwith
Silica		
SiO2	13/12	Palomera
Basic degree index (garnet, clinopyroxene, epidote and chlorite)	12/13	Bierwith, CSIRO

Table 3-1: Computed ratios.

FEATURE	RED	GREEN	BLUE
Lithology discrimination (ASTER level 1B)	4	6	8
Ratio composite_2	5/3 + 1/2	(6+9)/8	(7+9)/8

Table 3-2: Computed composite

3.7 Data Training and Varidation

Eight transects were studied. Two of these transects thus Coonteruah and Duffer were studied in detail as training while the remaining five; Apex, Euro, Mt Ada, Panorama, Charteris and North Star were used for validation. The Coonterunah and Duffer were chosen because they have good lithological variation and dominated by mafic and felsic rock respectively. Airborne gamma-ray validation used ternary map tonal variation while ASTER used spectroscopy interpretation and image colour variations results.

3.8 Data Integration

In this study data integration means comparing use of different datasets in order to generate more information that could compliment interpretation of lithological mapping. Airborne gamma-ray ternary image and ASTER composite ratio images were computed for the whole area. The two images were interpreted separately using thresholds developed from studying the Coonterunah and Duffer transects that was validated with samples from Apex, North star, Euro, Charteris, Panorama, Mt Ada and Apex transects. Each dataset classification was compared for generation of more information using raster calculator in ArcGIS 10.2. The geological map produced by Geological Survey of Australia was used as a reference. Visual image classification elements were used in comparison.

4 RESULTS AND DISCUSSION

4.1 Introduction

This chapter describes results of airborne gamma-ray, whole-rock geochemical data, ASTER images and laboratory spectroscopy that were found by studying the Warrawona, Kelly and Sulphur Spring groups of volcanic sequences in EPGGT. The Coonterunah and Duffer transects are discussed in detail as they were used as training sample because of their good lithological variation representing mafic and intermediate to felsic rocks respectively while North Star, Mt Ada, Apex, Panorama Chateris and Euro transects were used for validation. Analysis was done for chemical and mineralogical variation between field and airborne datasets.

Studying chemical variation of K, Th and U using box and scatter plots was found suitable for the study because they provide a good visualisation. Box plots provided visualisation of lithology class composition and separation with respect to other classes while scatter plots gave visualisation of correlation of measured values between whole-rock laboratory and airborne gamma-ray geochemical datasets respectively.

Furthermore, use of laboratory reflectance spectra of 350nm 2500nm wavelength to identify detectable minerals and understand effects of weathering using TGS and ENVI was suitable for study as it covers the wave length region that ASTER covers and most of the spectral detectable minerals have their diagnostic feature.

4.2 Lithological Classification

Lithology classification was applied to geochemical sample subset to confirm field descriptions and enable proper classification and comparison with airborne gamma-ray. Comparison of SiO_2 and NaO_2 + K_2O variations shows overlap between peridotite/komatiite, komatiite, komatiitic basalt and basalt, andesite and basalt and andesite and dacite. Although Peridotite/komatiite, komatiite, and komatiitic basalt overlap with basalt it can be discriminated from basalt as they show low values than basalt (Figure 4.1).

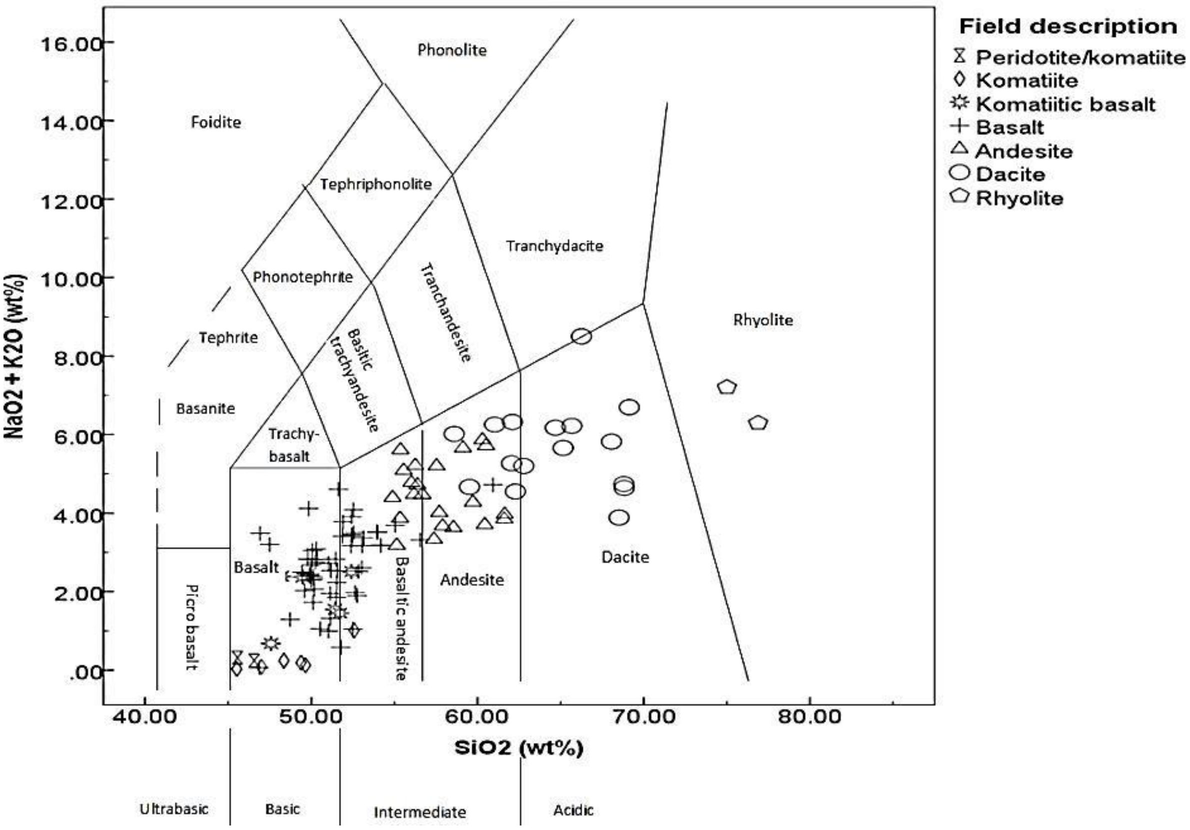

Figure 4-1: Lithology classification using SiO_2 versus Na_2O + K_2O of geochemical samples from transect subsets (rock nomenclature after Le Maitre, 2002).

4.3 Coonterunah Transect

A total of 33 samples were compared for whole-rock geochemistry and mineralogical variation. These were; 4 komatiite, 17 basalt, 11 andesite 1 dacite and. A total of 56 spectra were analysed of which 28 were from fresh and another 28 from weathered surfaces. According to published geological map the main volcanic sequence on transect includes; Table Top, Coucal and Double Bar Formations (Appendix 1).

4.3.1 Chemical Variation.

4.3.1.1 Box Plots

The thorium box plot of laboratory whole-rock geochemical data shows overlaps between basalt, andesite and dacite. Each pair was being influenced by a few outliers in basalt and andesite respectively. There is no overlap between komatiite and the other lithologies. On the other hand airborne gamma-ray box plots shows overlap between all lithology classes (Figure 4-2). The potassium box plot shows overlap between andesite, basalt and dacite. Only komatiite shows a clear separation while airborne gamma-ray show overlap between all classes (Appendix 2). The uranium box plot shows overlaps between komatiite, basalt and andesite apart from dacite while airborne gamma-ray shows overlap between all these lithology classes (Appendix 2).

Overlaps in lithologies of airborne gamma-ray box plot might be influenced by earlier processing steps. Although airborne gamma-ray survey data is normally corrected along flight lines in a systematic way. The final grid is produced after a number of steps that filter the raw data to make it usable. Several algorithms are used to interpolate final values into a grid. This makes point values relative measurements especially those away from the flight line which are not directly opposite the sensor giving them less influence to the sensor due to long travel distance. In addition there are few geochemical samples to highlight enough variation.

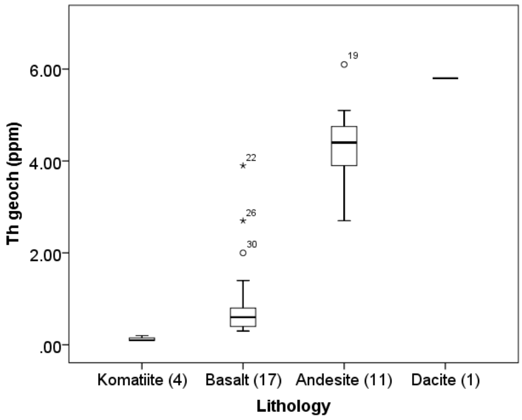

(A) Laboratory geochemical data

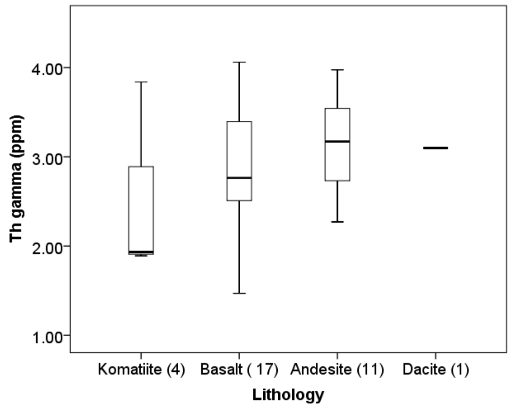

(b) Airborne gamma-ray data

Figure 4-2: Thorium Box plots showing comparison of the thorium content measured with whole-rock laboratory geochemistry and airborne gamma-ray spectrometry for Cooterunah transect

4.3.1.2 Scatter Plots and Deviation Analysis

Scatter plots for whole-rock laboratory geochemical data and airborne gamma-ray data showed poor correlation of 0.33, 0.36 and 0.09 for Th, K, and U respectively. These correlation values are well illustrated with the fitted 1:1 trend line in the scatter plots and deviation analyses. Deviation analysis compares the measured value difference between whole rock geochemistry and airborne gamma-ray spectrometry datasets with respect to 45-degree line (1:1 line) (Equation 1). Basing on the cluster and distance from 1:1 line the deviations are categories into three categories, Better, Over and Under estimated. Better estimates means deviation cluster with the shortest distance to the 1:1 line that can be accepted to be reasonable and comparable to whole-rock geochemistry measured value. Underestimates means deviation with values lower than better estimate and overestimated imply having measured values higher than better estimates. Over and Underestimated categories are further classed into low and high classes. For the sake of discussion Underestimated and Overestimated low and high classes shall be "ULC", "UHC", "OLC" and "OHC" respectively.

$Y = X + 0$ ……………………Equation 1.

Where Y is airborne gamma-ray spectrometry measurement, X is whole-rock geochemistry measurement

Thorium

Scatter plot denotes that laboratory whole-rock geochemical measurements values for Th increases from ultra-mafic to intermediate rock while airborne gamma-ray measurements does not show this trend. This discrepancy is explained by a linear trend in deviation plot which suggest a poor correlation and calibration error in airborne dataset. The deviation categories show that 15.15% of the samples are better estimated, 24.24% are underestimated and composed of 18.18% of ULC and 6.06% of UHC. Overestimated category has 60.61% of which, 51.52% is from OLC and 9.09% from OHC. Intermediate rocks are more underestimated while mafic rocks are overestimated (Table 4.1 and Figure 4-3).

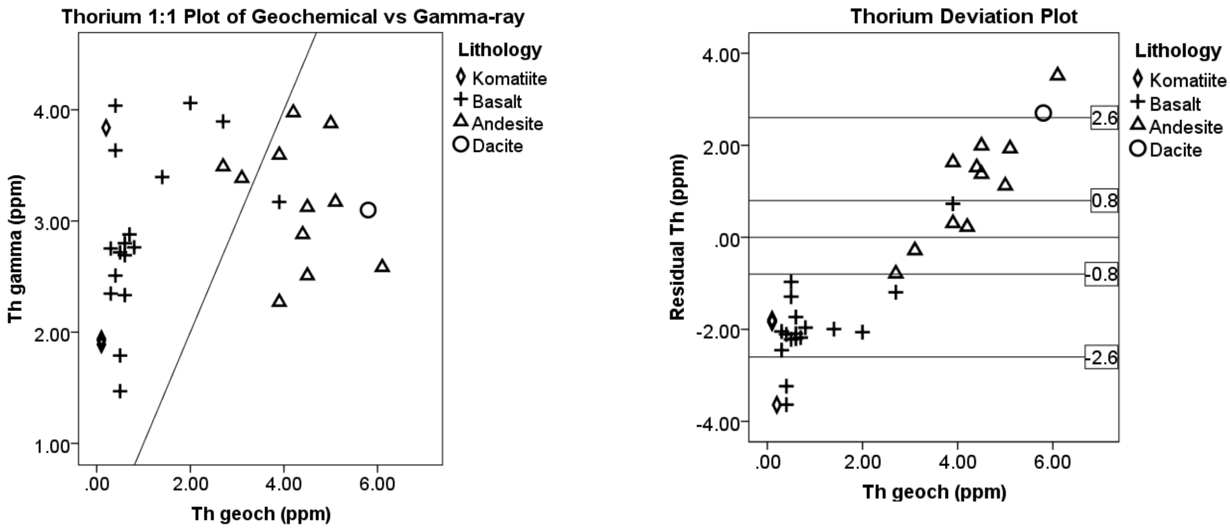

Figure 4-3: 1:1 fit on scatter plot and deviation plot of thorium for Coonterunah formation.

Lithology	Better estimated (ppm)	Underestimated classes (ppm)		Overestimated classes (ppm)		
Geological map code	Better	Low	High	Low	High	Total
	-0.8 - 0.8	0.8 – 2.6	< 2.6	-0.8 - -2.6	>-02.6	
AOt		3 Andesite	1 Andesite	3 Komatiite, 11 Basalt	1 Komatiite, 1 Basalt	**20**
AOcbi	1 Andesite	1 Andesite	1 Dacite	2 Basalt		**5**
AOcf	1 Basalt	2 Andesite				**3**
Auph				1 Basalt	1 Basalt	**2**
AOd	3 Andesite					**3**
Total	**5**	**6**	**2**	**17**	**3**	**33**

Note: geological map code description refer to appendix 1

Table 4-1: Thorium deviation class contribution from each lithology of Coonterunah transect.

In appendix 3, overlay of deviation classes on geology and thorium distribution map shows that most of the better and underestimates class values plots within the intermediate volcanic and lithology transition zones. This might be influenced by sampling foot print or pre-processing steps and calibration. The lithologies are elongated and perpendicular to flight lines providing least coverage. Pre-processing steps of airborne gamma-ray data such as removal of background radiation from the atmosphere and smoothing uses interpolation algorithms to make data usable. The algorithms influences reported values.

Furthermore, OLC values that dominate the AOt basalt might also be influenced by the felsic intrusion in the Table Top Formation as it is expected to have high thorium values in felsic rocks (Dentith, 2014). The OHC values at the bottom of the Coonterunah formation might have been influenced by sampling foot print since it is close to contact with Carlindi granitoid. The linear trend as observed in the deviation plot would be calibration error. Although measurements are not correlating very well between airborne gamma-ray and laboratory whole-rock geochemical datasets, spatially at large scale a similar increasing trend of measured values of Th from mafic (AOt) to intermediate (AOcbi and AOcf) rock could be observed in airborne gamma-ray (Appendix 3). The main difference of the two datasets is that airborne gamma-ray shows little variation compared to whole-rock laboratory geochemistry measurements.

Potassium

Potassium scatter plot in figure 4-4 shows an increasing trend of K content from ultra-mafic to intermediate rocks thus; between komatiite, basalt and andesite/dacite. There is no clear difference between andesite, basalt and dacite as was the case with thorium. On the other hand airborne gamma-ray does not show any trend but deviation plot shows a linear trend which might explain the discrepancy. Deviation categories show that 60.61% of the samples are better estimated, 12.12% underestimated and both ULC and UHC contribute 6.06% each. The remaining 27.27% belongs to overestimated category composing of 18.18% from OLC and 9.09% from OHC (Table 4-2 and Figure 4-4).

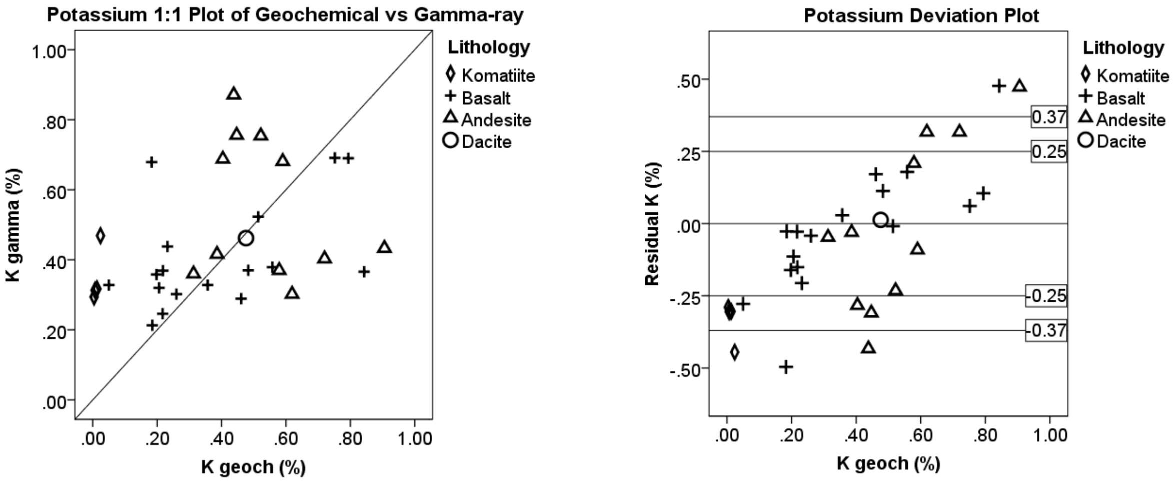

Figure 4-4: 1:1 fit on scatter plot and deviation plot of potassium for Cooneterunah formation

Lithology	Better estimated (%)	Underestimated classes (%)		Overestimated classes (%)		
Geological map code	Better	Low	High	Low	High	Total
	-0.25 – 0.25	0.25 – 0.37	< 0.37	-0.25 - -0.37	>-0.37	
AOt	10 Basalt & 2 Andesite	2 Andesite	1 Basalt	3 Komatiite, 1 Basalt,	1 Komatiite	**20**
AOcbi	1 Dacite 1 Basalt & 1 Andesite			1 Andesite	1 Basalt	**4**
AOcf	1 Andesite & 1 Basalt		1 Andesite			**4**
Auph	2 Basalt					**2**
AOd	1 Andesite			1A	1A	**3**
Total	**20**	**2**	**2**	**6**	**3**	**33**

Note: Geological map code description refer to appendix 1

Table 4-2: Potassium deviation class contribution from each lithology of Cooneterunah transect

Shown in appendix 3, overlay of deviation classes on geological and potassium distribution maps reveal that most of better estimate classes plots in the middle or where lithology surface coverage is relatively larger while overestimate classes plot close to lithological boundaries or where lithology surface coverage area is small. This might be related to sampling foot print. Airborne gamma-ray spectrometer has a large sampling foot print. It samples a point over relatively large areas subject to ground clearance, sample condition and sampling interval and line spacing. The measured value is an average over a relatively large area. On the other hand whole-rock laboratory geochemistry measurement uses a small sampling foot print. Measurements are done on a small area that has been carefully selected to suit research objectives. The low under estimate plotting over the Coucal formation (AOcbi and AOcf) could be associated to calibration error since both lithologies shows better estimated class while over estimates could be related to lithology foot print. Overestimate in Double Bar formation (AOd) could be related to calibration error. Furthermore, weathering would also contribute. Mafic rocks weathers easily exposing more radiation that intermediate rock which do not. Although theses discrepancies were observed an increasing trend of measured value for K from mafic to intermediate rock similar to whole-rock geochemistry measurement could be observed on airborne gamma-ray K distribution map (Appendix 3). The main difference is that airborne gamma-ray has little variation. This is similar to what was observed in thorium.

In addition, the AOt lithology better explains the effects of sampling foot print due to relatively large number of samples (Table 4-2 and Appendix 3). The better, low and high classes plot from the middle of a lithology to the boundary respectively. This implies that moving out of a lithology the foot print coverage reduces as it starts to account for another lithology.

Uranium

Uranium Scatter plot shows that whole-rock laboratory geochemistry measurements associate low measured values to mafic rock and high values to intermediate rock while airborne gamma-ray does not. Whole-rock laboratory geochemistry measurements also have almost the same values for ultramafic and mafic rock. This might be a result of lithology having values below detection limit of the ICP-MS. Deviation categories shows that better estimated category has 24.24% of samples. Under estimated category have a 21.21% of which 9.09 is from ULC and 12,125 from UHC. Overestimated category has 54.54% of which, 30.30% are from OLC and 24.245 from OHC. Intermediate rocks are more underestimated and mafic rocks are overestimated (Table 4.3 and Figure 4-5).

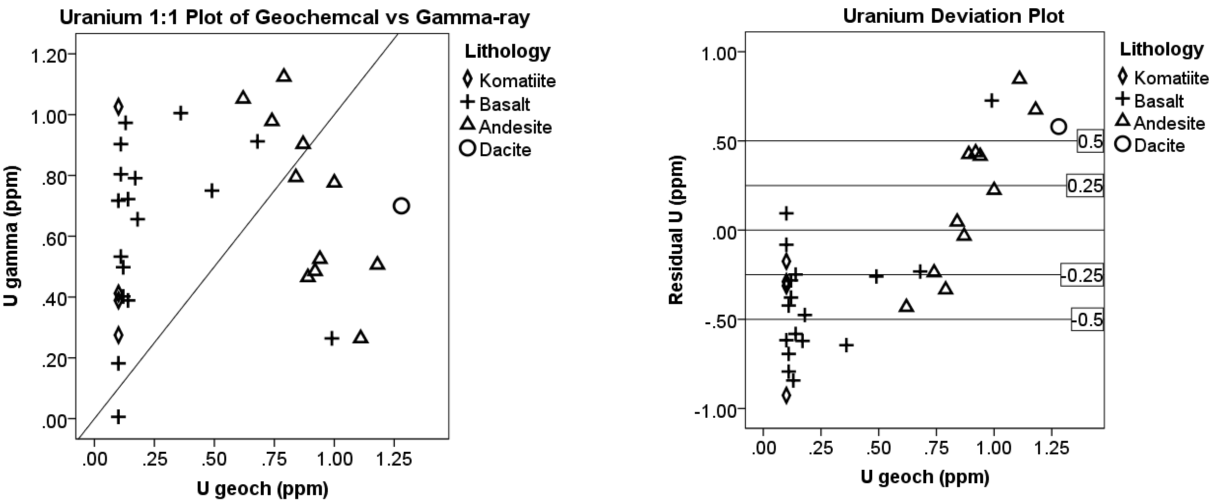

Figure 4-5: 1:1 fit on scatter plot and deviation plot of uranium for Coonterunah formation

Lithology	**Better estimated (ppm)**	**Underestimated classes (ppm)**		**Overestimated classes (ppm)**		
Geological map code	**Better**	**Low**	**High**	**Low**	**High**	**Total**
	-0.25 – 0.25	**0.25 – 0.5**	**< 0.5**	**-0.25 - -0.5**	**>-0.5**	
AOt	1 Basalt 1 Komatiite, 2 Basalt	2 Andesite	1 Andesite	1 Komatiite, 4 Basalt, 1 Andesite	2 Komatiite, 5 Basalt	**20**
AOcbi	2 Andesite 1 Basalt		1 Dacite	1 Basalt		**5**
AOcf		1 Andesite	1 Andesite, 1 Basalt			**3**
Auph				1 Basalt	1 Basalt	**2**
AOd	1 Andesite			2 Andesite		**3**
Total	**8**	**3**	**4**	**10**	**8**	**33**

Note: geological map code description refer to appendix 1

Table 4-3: Uranium deviation class contribution from each lithology of Coonterunah transect.

Overlaying the deviation classes on geology and uranium distribution map shows that the distribution map is noisy (Appendix 3). The high variation of measurement values for mafic rocks could be an effect of radon gas. Radon is produced in a decay series of uranium and is also more present in surrounding air and atmosphere. Its abundant presence affects uranium reading. In addition high overestimated class plotting at the bottom of the Table Top Formation could be influenced by the recent alluvial deposits and the Carlindi intrusion while underestimation could be explained by pre-processing steps.

4.3.1.3 Effects of Relief on Airborne Gamma-ray

A topographic profile of the Coonterunah transects shows a relative flat terrane ranging between 160 – 200 meters in altitude. Measurement comparison of all radioelements with relief does not show any influence. It was expected to have high measurement values of radioelements in low lying areas than in elevated ones (Appendix 4). Normally relief may influences radioelement concentration in low lying areas through is effects on soil erosion and formation.

4.3.2 Spectrally Detectable Mineral and Effects of Weathering

Spectroscopic interpretation of fresh and weathered sample spectra between 350nm to 2500nm shows that mappable minerals in the Coonterunah transect are hornblende, epidote, actinolite, Mg-chlorite, Fe-chlorite and intermediate-chlorite (Mg-OH and Fe-OH). Halloysite (Al-OH), oxides and hydroxides are been introduced due to weathering. The main diagnostic features for Mg-OH, Fe-OH and Al-OH are 2325nm, 2245 and 2200nm respectively (Abweny, 2012). Due to weathering there are absorption shifts. Fresh samples show Mg-OH, Fe-OH and Al-OH absorption features ranges of 2317nm - 2347nm, 2250nm - 2259nm and 2200nm – 2206nm respectively while weathered samples shows 2315nm – 2355, 2246nm – 2257nm and 2205 – 2209nm respectively. The absorption shifts are related to formation of halloysite and iron oxides and hydroxides. The iron oxide and hydroxides forms a cast on the exposed rock surface covering detectable minerals (Figure 3-2).

Halloysite is an alluminosilicate that is formed by hydrolysis. It occurs easily in weathered igneous rocks especially glassy basaltic rocks and is associated with goethite and limonite (Kerry, 1952; Wilson., 1999).

The source of this iron is chemical alteration of chlorite, hornblende and epidote. This was evidenced by a decrease in absorption depth of Mg-OH and Fe-OH in weathered sample compared to fresh samples. Furthermore, increase in iron rise around 550nm to 700nm and 1100nm that is prominent in weathered surfaces also confirms oxidation. Iron might also be responsible in decrease of Mg-OH as the cast it forms might be blocking fresh samples from detection. The case might also be influenced by soil formation (Figure 3-2). The changes in absorption features persist in the ASD spectra of VNIR-SWIR region that were resampled to ASTER (Figure 4-6 and 4-7).

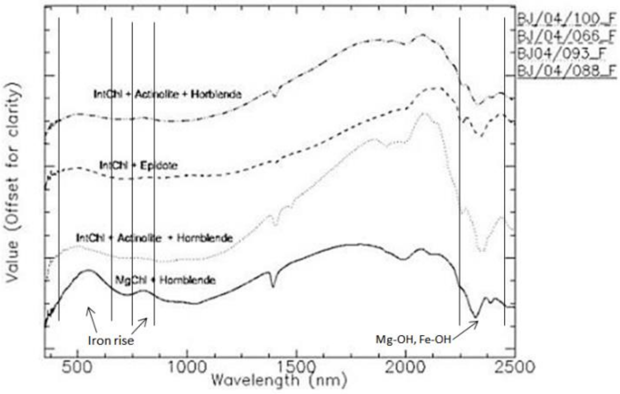

(a) ASD spectra

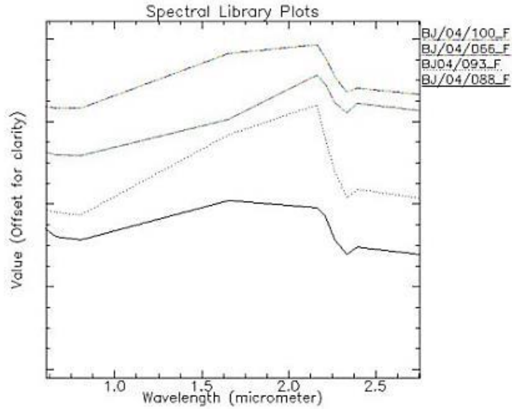

(b) Resampled ASD spectra

Figure 4-6: Stacks of laboratory spectra obtained from fresh sample of Coonterunah transect showing diagnostic features.

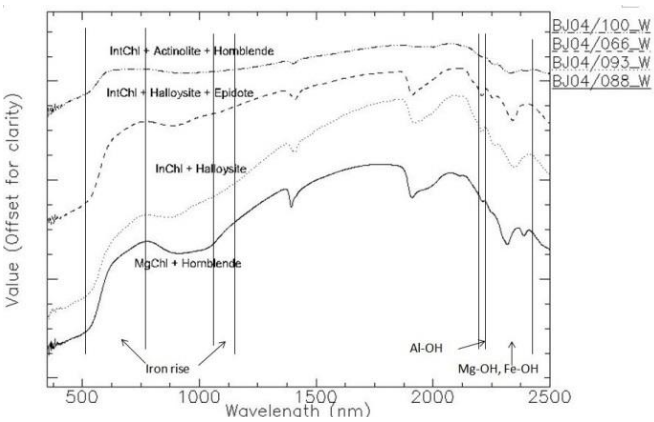

(a) ASD spectra

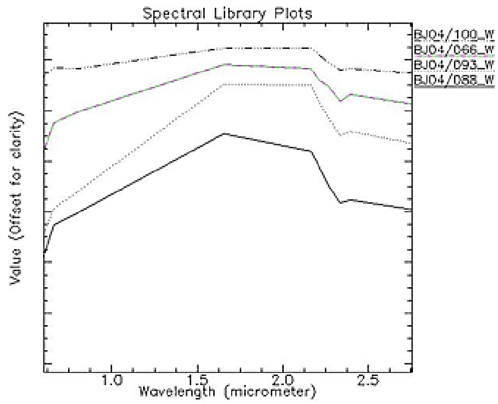

(b) Resampled ASD spectra

Figure 4-7: Stacks of laboratory spectra obtained from weathered sample of Coonterunah transect showing diagnostic features.

4.3.3 ASTER Mineralogical Mapping.

Spectral difference and similarity between geological features can be enhanced by band ratios. It is techniques that add, divide or subtract digital number (DN) values in one spectral band by a corresponding value in another band. The techniques give spectral characteristic regardless of variation in scene characteristics on image features (Lillesand & Kiefer, 1987). In this research the box plot of band ratios pixel values of laboratory spectra that was resampled to ASTER shows that from the commonly used ratio that were computed (Table 3-1). Fe-OH, Mg-OH minerals that ASTER can detect are best highlighted using band ratios 5/3 + 1/2, (6+9)/8 and (7+9)/8 which highlights well ferrous iron (Fe^{2+}), amphibole and Mg-OH and carbonate, chlorite and epidote respectively. Lithology class overlap could still be observed but the ratios have different means and distribution compared to other ratios (Figure 4.8 and Appendix 5).

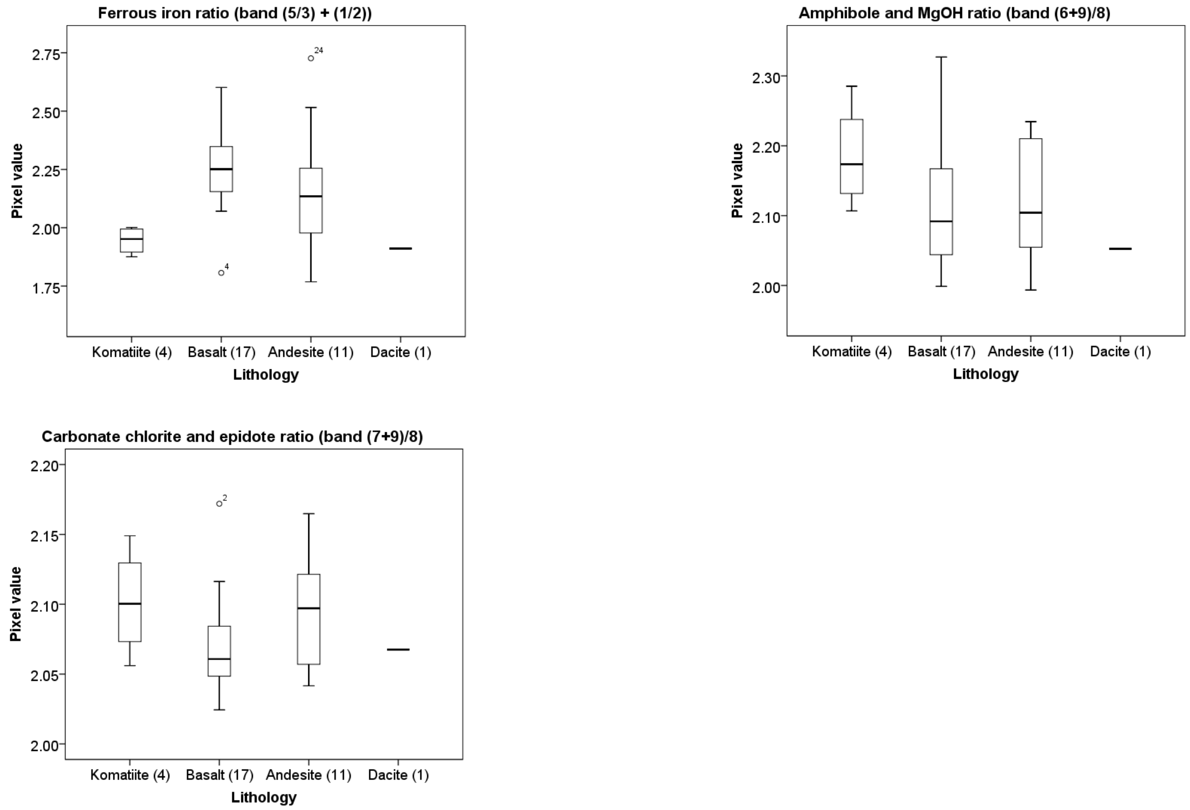

Figure 4-8: Box plot of band ratio pixel value of laboratory spectra resampled to ASTER discriminating lithology.

Assigning Ratio composite_2 to channels as shown in Table 3-2 gives good mineralogical variation. The colour variation matches well with laboratory spectroscopy results which discriminate the transect lithology based on mineral assemblage, thus; Mg-chlorite + hornblende + intermediate-chlorite + actinolite, intermediate-chlorite + actinolite + hornblende and intermediate-chlorite +epidote (Figure 4-9A).

The ratio composite_2 image in figure 4-9A, shows fine to medium grained metabasalt, meta-dolerite and amphibolite (AOt) lithology which forms the bottom of the Coonterunah formation together with the komatiite in white to cream colour. The colour signifies high presence of minerals with ferrous iron, MgOH and amphiboles. This might be related to high magnesium-chlorite and hornblende, actinolite and intermediate chlorite identified using laboratory spectral measurement. Ferrous iron should be attributed from hornblende and actinolite as they both have iron. Furthermore, having same colour in this lithology shows that ASTER could not discriminate ultra-mafic (komatiite) from mafic (basalt). Two senarios would explain this; either komatiite have small outcrop or must have been weathered or the similarity in mineralogical composition. The felsic volcanic metamorphosed (AOcf) and andesite to basalt metamorphosed (AOcbi) forming the Coucal formation could not be discriminated as such. These showed a uniform pale brown colour that is being influenced by intermediate-chlorite, actinolite and hornblende. Massive tholeiitic basalt (AOd) forming Double bar formation at the top of the Coonterunah formation is highlighted in brown, being influenced by intermediate-chlorite and epidote with high iron content. The granitic intrusion (AgLp) is highlighted in red to brown due to high ferrous silicate minerals i.e. biotite, plagioclase and feldspar furthermore, presence of epidote with high iron content. The intrusion might have influenced the presence andesitic composition within the Double Bar Formation.

Halloysite that was identified using laboratory measurements did not have much of the effect as evidenced by ratio $(5x7)/6^2$ images. It is well mapped in alluvial deposits and might have been eroded from the cherty iron beds and other areas (Appendix 6).

4.3.4 Data Integration

ASTER image highlights lithologies based on mineral assemblage (Figure 4-9A). In this transect Mg-chlorite and epidotes are main minerals discriminating lithology. Ultra-mafic and mafic rocks could not be discriminated and similar is the case with intermediate and felsic rock. Mafic lithologies might be influenced by weathering that might have eroded/cover the komatiite more easily than basalt while intermediate rock could be influenced by having little mineralogical variation. On the other hand ternary image could only map well AOt and AWebm lithologies which have large surface coverage and distinct K and Th values (Figure 4-9B). The Table Top formation lithology (AOt) has very low values for both K and Th while the Euro basalt Formation (AWebm) has low Th and medium K values. These variations also enable the two formations to be discriminated by making the AOt show black while the AWebm shows deep red due to K high (Appendix 3). In addition it should be known that on the ternary map darkness is accounted for by intensity. This is represented by grey scale legend while that of ternary consider the ratio of the three channels.

The Double Bar formation (AOd) which is also mafic formation and the Coucal formation which is an intermediate volcanic (AOcbi and AOcf) were not clearly delineated. As discussed in section 4.3.1 poor delineation of these two formations could be a result of instrument calibration error, processing steps and lithology foot print and lithology composition overlap (Appendix 3).

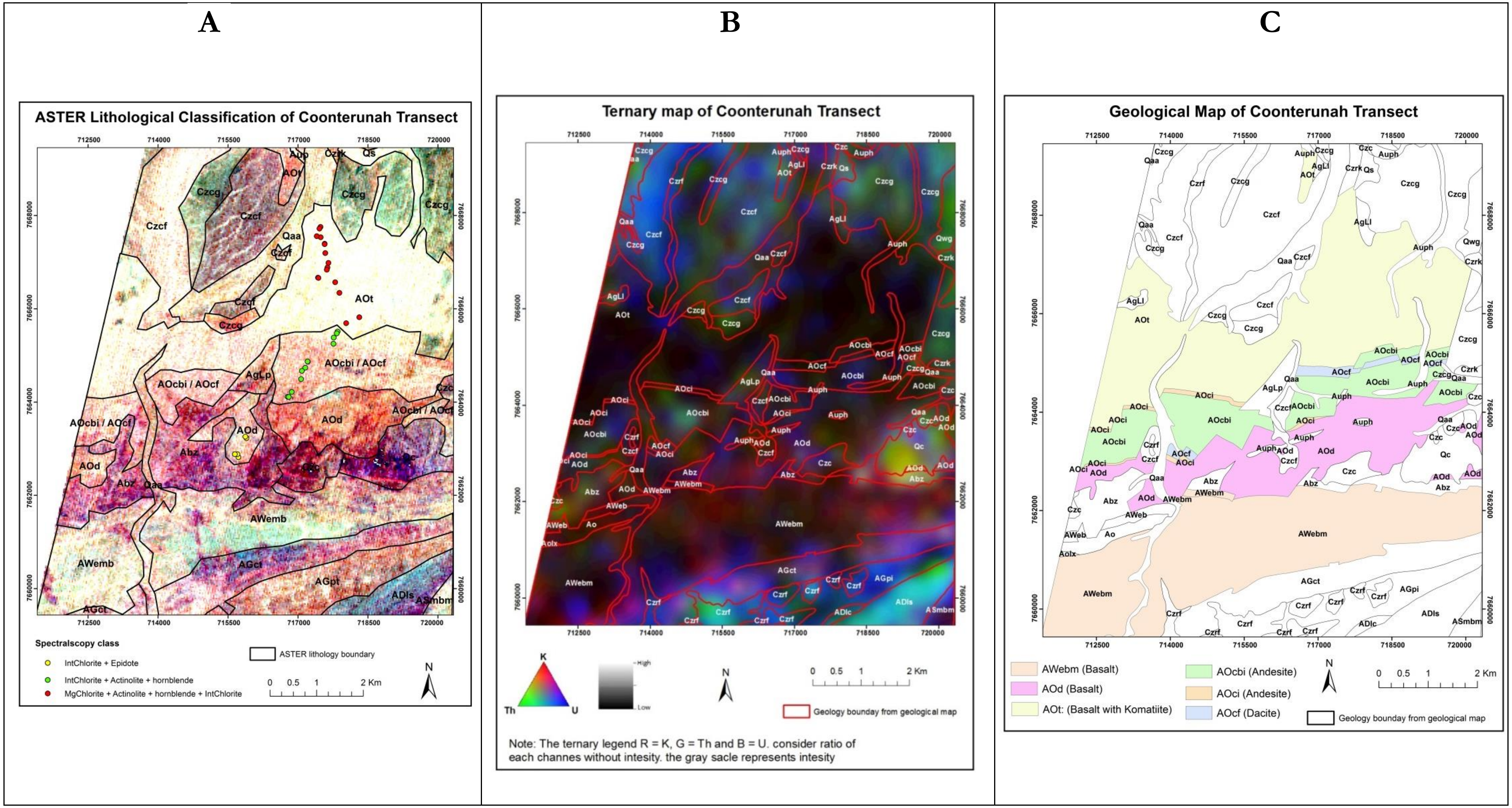

Figure 4-9: Map showing overlay of (A) ASTER composite ratio_2 and laboratory spectroscopy interpretation classes, (B) Gamma- ray ternary image and geology boundary from published geological map and (C) Published geological map highlighting volcanic sequences classes of Coonterunah transect (geological code description refer to appendix 1)

4.4 Duffer Transect

The Duffer transect was composed of 24 samples of which 9, 6, 8 and 1 were basalt, andesite, dacite and rhyolite respectively. A total of 84 spectra were analysed of which 24 were from fresh and another 24 from weathered rock surfaces. The Duffer transect is mainly composed of volcanoclastic, dacitic to rhyolite rocks and tholeiitic basalt and layered metachert according to the published geological map (Appendix 7).

4.4.1 Chemical Variation

4.4.1.1 Box Plots

The thorium box plots for both laboratory whole-rock geochemical data and gamma-ray data showed same single sets of overlaps thus; basalt, andesite and dacite. While whole-rock laboratory geochemical data shows overlap between andesite, dacite and rhyolite, and a clear separation between rhyolite and basalt, airborne gamma-ray shows overlap between basalt andesite and rhyolite and a clear separation between dacite and rhyolite (Figure 4-10). The potassium box plots for laboratory whole-rock geochemical data shows that andesite overlaps all classes. Andesite overlap with basalt is being influenced by a few outlies. There is a clear separation between basalt, dacite and rhyolite. On the other hand airborne gamma-ray box plot shows overlaps between all classes (Appendix 8). The uranium box plot for laboratory whole-rock geochemical data shows overlaps between basalt, andesite and dacite while rhyolite is separable from the other classes. On the other hand, airborne gamma-ray box plot shows overlaps between basalt andesite and dacite. Only andesite and rhyolite are separable (Appendix 8). Overlaps in lithologies for airborne gamma-ray box plot might be influenced by same conditions described in section 4.3.1.1 of the Coonterunah transect.

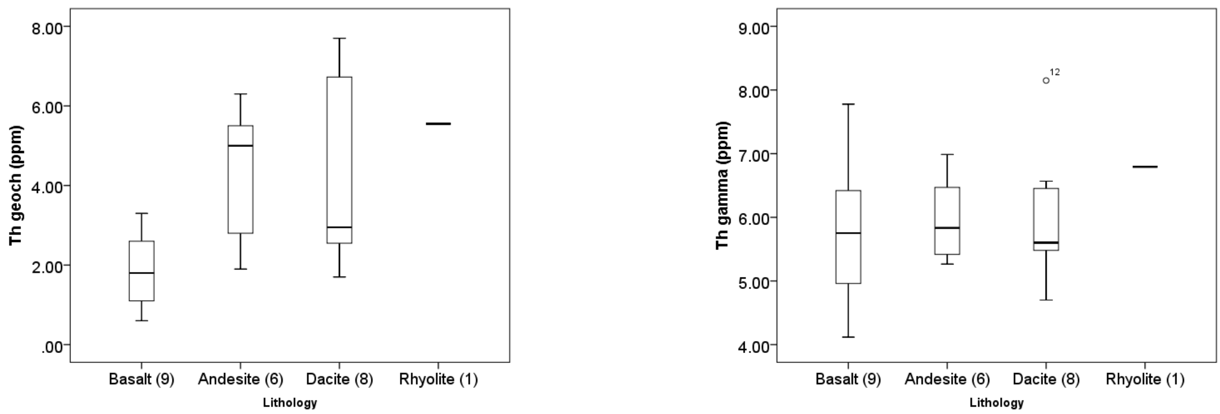

(a) Laboratory geochemical data (b) Airborne gamma-ray data

Figure 4-10: Thorium Box plots showing comparison of the thorium content measured with whole-rock laboratory geochemistry and airborne gamma-ray spectrometry for Duffer transect

4.4.1.2 Scatter Plot and Deviation Analysis.

Scatter plots for whole-rock laboratory geochemical and airborne gamma-ray datasets showed poor correlation strength with Th, K and U showing 0.37, 0.42 and 0.07 and is explained by fitting a 1:1 trend on scatter plot and deviation analysis. The high correlation in Th could be influenced by more presence of accessory minerals such as epidote which host thorium. The deviation are analysed as described in section 4.3.1.2 by categorising them into Better, Under and Overestimated the latter two having ULC, UHC, OLC and OHC Classes.

Thorium

Scatter plot reveal that whole-rock laboratory measurements have an increasing trend in measurement value from mafic to felsic rocks while airborne gamma-ray does not. This is explained by the deviation analysis plot that shows a linear trend confirming poor correlation and high error. Deviation categories show that better estimated category has 25% of the samples. Underestimated category has 4.2% from ULC only while overestimated has 70.8% of which 58.3% is OLC and 12.5% from OHC. (Table 4-4 and Figure 4-11).

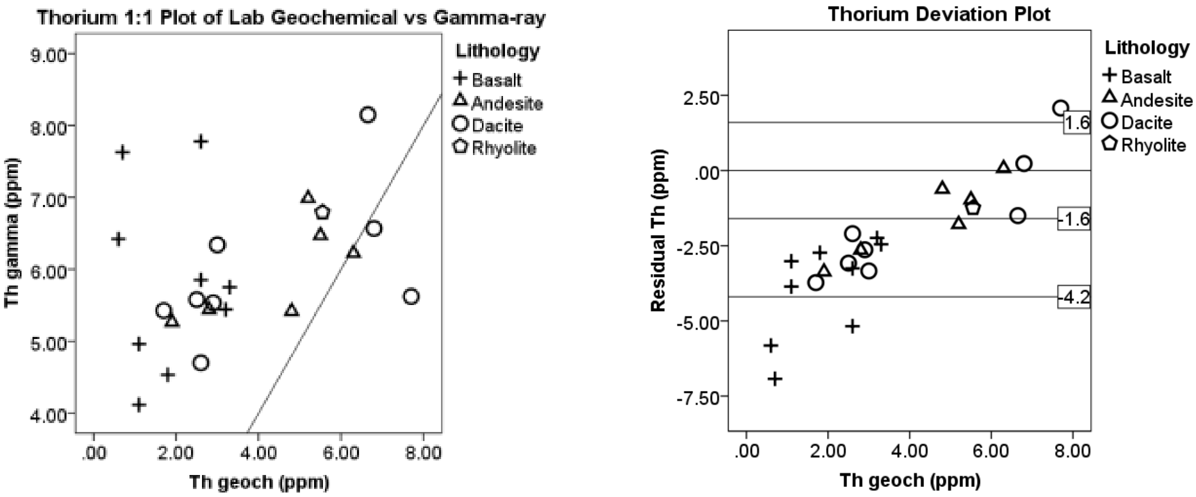

Figure 4-11: 1:1 fit on scatter plot and deviation plot of thorium for Duffer formation.

Lithology	Better estimated (ppm)	Underestimated classes (ppm)		Overestimated classes (ppm)		
Geological map code	**Better**	**Low**	**High**	**Low**	**High**	**Total**
	-1.6 – 1.6	**1.6 – 4.2**	**<4.2**	**-1.6 - -4.2**	**>-4.2**	
AWmbt				2Basalt, 1 Andesite,		**3**
AWmb				3 Basalt	1 Basalt	**4**
AWdfx	2 Dacite, 2Andesite	1 Dacite		5 Dacite, 2Andesite, 1Basalt	1 Basalt	**14**
AWdb	1 Andesite					**1**
AWdfdp	1 Rhyolite					**1**
AWmbk					1 Basalt	**1**
Total	**6**	**1**		**14**	**3**	**24**

Note: Geological map code description refer to appendix 7

Table 4-4: Thorium deviation class contribution from each lithology of Duffer transect.

Overlay of deviation classes on geology and thorium distribution maps in appendix 9 showed that better estimates plots in intermediate and felsic lithology while overestimate plots mostly in mafic rock. Better estimation in intermediate and felsic rocks might be related to lithology surface area coverage and processing steps. Most of the sampled intermediate and felsic rock have a relatively large surface area coverage compared to mafic rock. Similarly, both under and overestimates could also be related to surface coverage area as they plot either close to lithology boundary or within relative small lithology compared intermediate and felsic lithology and furthermore, calibration error. At a large scale spatially, thorium shows a general comparable results to laboratory geochemical results as it is able to discriminate intermediate/felsic from mafic rock (Appendix 9).

Potassium

Scatter plot for potassium shows similar results to thorium, having showed an increase in measurement values from mafic to felsic rocks for whole-rock laboratory geochemical measurement and a linear trend on deviation plot. Deviation better estimated category is composed of 37.5%, under and overestimated categories are composed of 12.5%, and 50% respectively. Intermediate and felsic rocks are better estimated than mafic rock (Table 4-5 and Figure 4-12).

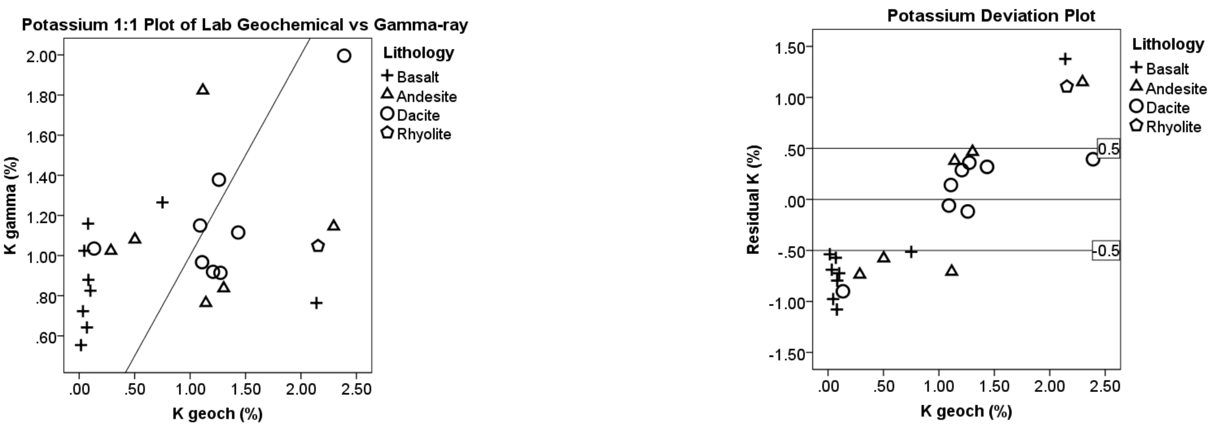

Figure 4-12: 1:1 fit on scatter plot and deviation plot of potassium for Duffer formation

Lithology	**Better estimated (%)**	**Underestimated classes (%)**	**Overestimated classes (%)**	
Geological map code	**Better**	**High**	**High**	**Total**
	-0.5 – 0.5	**<0.5**	**>-0.5**	
AWmbt	1 Andesite	1 Basalt	1 Basalt	**3**
AWmb			4 Basalt	**4**
AWdfx	7 Dacite, 1Andesite	1 Andesite	2 Andesite, 1 Dacite, 2Basalt	**14**
AWdb			1 Andesite	**1**
AWdfdp		1 Rhyolite		**1**
AWmbk			1 Basalt	**1**
Total	**9**	**3**	**12**	**24**

Note: Geological map code description refer to appendix 7

Table 4-5: Potassium deviation class contribution from each lithology of Duffer transect.

In appendix 9, an overlay of deviation classes on geology and potassium distribution map shows that better estimated categories plots in felsic rocks while under and overestimate plot mostly in mafic rocks. Both estimates could be influenced by lithology surface area coverage as describe with thorium that most of the sampled intermediate and felsic lithologies have large surface area coverage compared to mafic lithology. Pre-processing steps and calibration might also be contribution. Furthermore at a large scale spatially, potassium could discriminate intermediate/felsic rock from mafic rock as also observed with thorium.

Uranium

Scatter plot show a systematic trend of measurement values from mafic to felsic rocks for whole-rock laboratory data while airborne gamma-ray does not show any trend rather all measurement values are associated with high values. The high values could be related to its high mobile nature and presence of radon gas in air. The measurement values trend could be explained by deviation analysis.

Deviation analysis better estimated category has 29.2% of the samples. Underestimated category has 16.7%, and each class contributing 8.3%. Overestimated has 54.2% of which 45.8% is from OLC and 8.3% from OHC (Table 4-6 and Figure 4-13).

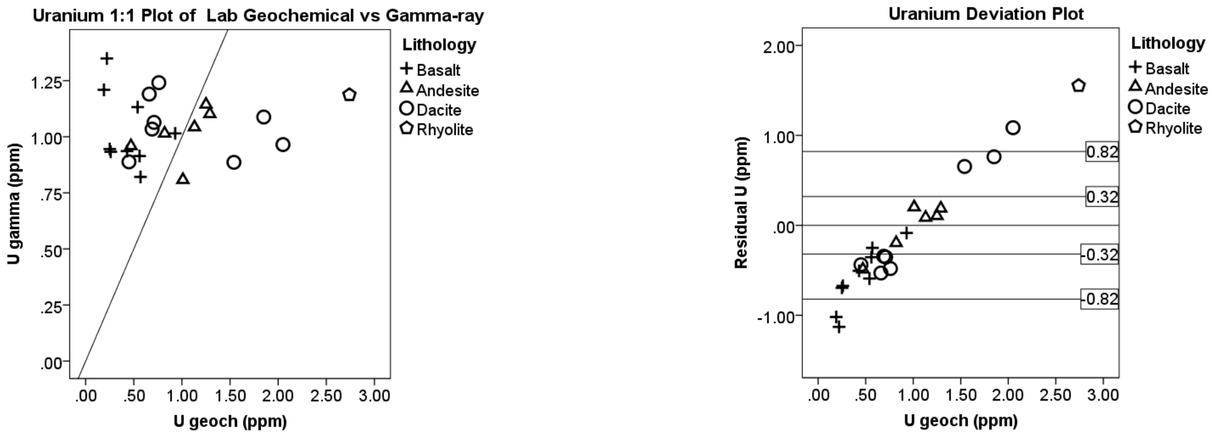

Figure 4-13: 1:1 fit on scatter plot and deviation plot of uranium for Duffer formation

Lithology	Better estimated (ppm)	Underestimated classes (ppm)		Overestimated classes (ppm)		
Geological map code	**Better**	**Low**	**High**	**Low**	**High**	**Total**
	-0.32 – 0.32	**0.32 – 0.82**	**<0.82**	**-0.32 - -0.82**	**>-0.82**	
AWmbt	1Basalt, 1Andesite			1 Basalt		**3**
AWmb				3 Basalt	1 Basalt	**4**
AWdfx	3Andesite, 1Basalt	2 Dacite	1D	5Dacite, 1Basalt, 1Andesite		**14**
AWdb	1 Andesite					**1**
AWdfdp			1Rhyolite			**1**
AWmbk					1 Basalt	**1**
Total	**7**	**2**	**2**	**11**	**2**	**24**

Note: Geological map code descriptions refer to appendix 7.

Table 4-6: Uranium deviation class contribution from each lithology of Duffer transect

As shown in appendix 9, overlay of deviation classes on geology and uranium distribution map showed better estimate plot in felsic lithology while overestimate plots mostly in mafic rock. Better estimation in intermediate and felsic rocks might be related to lithology surface area coverage and processing steps as observed in thorium that intermediate and felsic lithologies have large surface area coverage compared to mafic lithologies. Similarly, both under and overestimates might also be explained by surface area coverage as they plot either close to lithology boundary or within relative small lithology compared to intermediate and felsic lithology and calibration error.

4.4.1.3 Effect of Relief on Airborne Gamma-ray.

Similar to the Coonterunah Formation, the Duffer Formation area is flat. Its altitude ranges between 146 – 160m. Radioelement measurement does not show any relief influence as described for Coonterunah transect in both section A-B and C-D of the transect (Appendix 10).

4.4.2 Spectrally Detectable Minerals and Effects of Weathering.

Similar to what is described in section 4.3.2. Spectroscopic interpretation of the Duffer Formation identifies epidote, intermediate-chlorite and Fe-chlorite, Illite and halloysite to be detectable. Absorption positions for Mg-OH, Fe-OH and Al-OH for fresh samples show ranges of 2339nm - 2352nm, 2249nm - 2258nm and 2207nm – 2219nm while weathered samples shows 2331nm – 2352, 2248nm – 2261nm and 2204 – 2215 respectively.

Weathering has introduced halloysite, illite oxides and hydroxide. The oxides and hydroxides forms iron cast on weathered surfaces. The iron cast (goethite and hematite) is result of chemical alteration in chlorite and epidote. This is evidenced by a decrease in absorption depth for Mg-OH and Fe-OH in weathered sample compared to fresh samples and iron rise around 530nm to 700nm and 800 to 1100nm that is prominent in weathered surfaces (Figure 4-14 and 4-15).

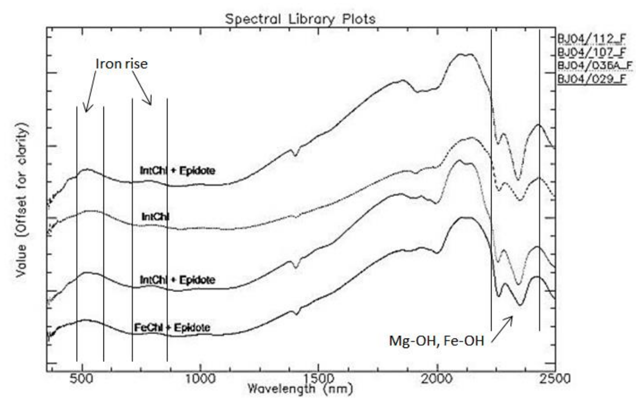

(a) ASD spectra

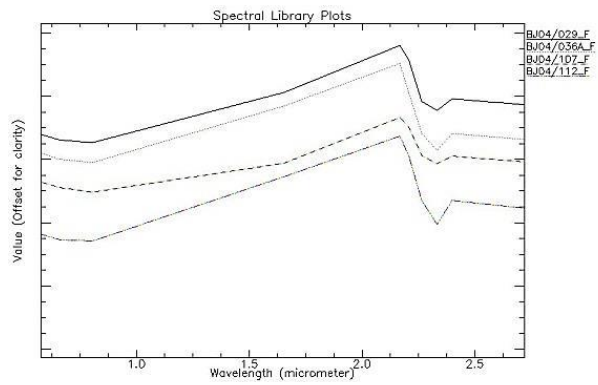

(b) Resampled ASD spectra

Figure 4-14: Stacks of laboratory spectra obtained from fresh sample of Duffer transect showing absorption points.

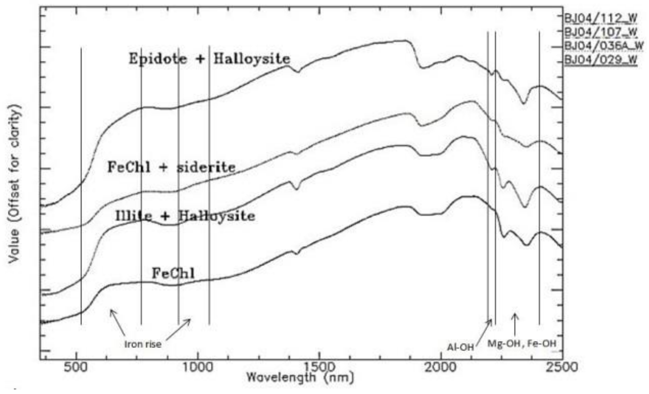

(a) ASD spectra

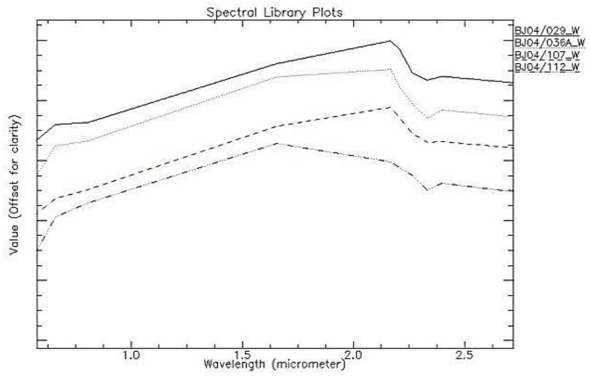

(b) Resampled ASD spectra

Figure 4-15: Stacks of laboratory spectra obtained from weathered sample of Duffer transect showing absorption points.

4.4.3 ASTER Mineralogical Mapping.

Results of spectroscopic band ratio pixel value analysis for laboratory spectra resampled to ASTER identify best lithology discriminating band and composite ratios to be the same as those for Coonterunah transect that highlighting ferrous iron (Fe^{2+}), amphibole and Mg-OH and carbonate, chlorite and epidote (Table 3-1 and 3-2, Figure 4-16 and Appendix 11).

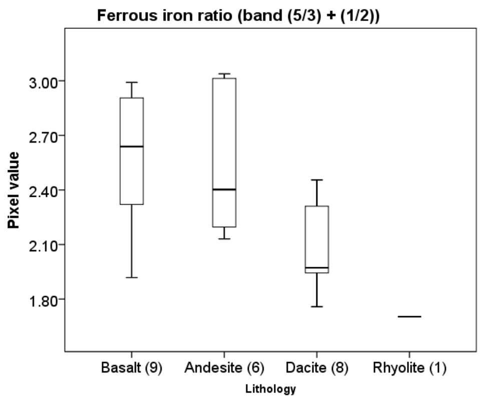

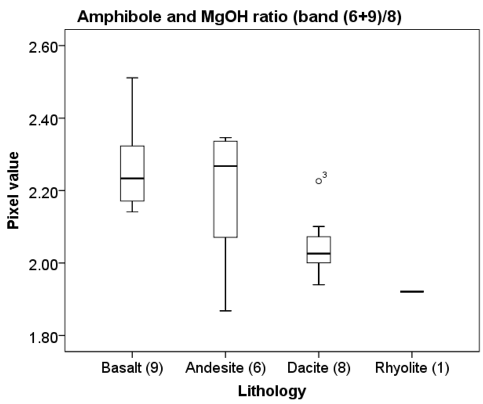

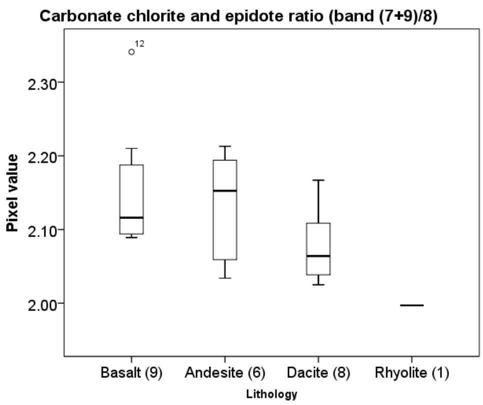

Figure 4-16: Box plot of band ratio pixel value of laboratory spectra resampled to ASTER discriminating lithology.

Mineralogical mapping on ASTER image does not show a clear variation due dominance of intermediate chlorite and epidote in all lithologies and weathering. Mt Ada basalt (AWmb) is being highlighted in pale yellow and pale red while Duffer Formations intermediate and felsic rocks are being highlighted in mixture of cream, pale red and pale green. This makes it difficult to discriminate dacite, andesite and rhyolite. Recent deposits are being highlighted in light cyan and dark red. Spectral assemblage could not be defined since all lithologies are dominated by intermediate-chlorite + epidote (Figure 4-17). Clay minerals identified on field measurements are relatively abundant in recent deposits and the Duffer Formation (Appendix 6).

4.3.4 Data Integration

ASTER image could not highlight mineral variation in the Duffer transect well due to high weathering that has enabled mafic lithology that occur as sill within intermediate lithologies not to be discriminated. Furthermore mineralogical overlap also influences the results. On the southern part of the map ASTER could discriminate Mt Ada basalt (AWmb) into AWmb and AWmba and intermediate rock due to large lithology surface area coverage and less weathering (Figure 4-17).

Similar to what was observed on Coonterunah transect, airborne gamma-ray maps well lithologies with large surface area coverage and distinct radiometric values (Figure 4-18A). Mt Ada basalt (AWmb) in black and alluvial sand and gravel in river and creek channel beds (Qaa) in red are being influenced by low values for potassium, thorium and uranium and medium potassium values respectively. Intermediate and felsic rocks of the Duffer formation are distinct from mafic rock due to medium, Th, K and U values which are uniform hence cannot be discriminated into single lithological classes thus dacite, andesite and rhyolite.

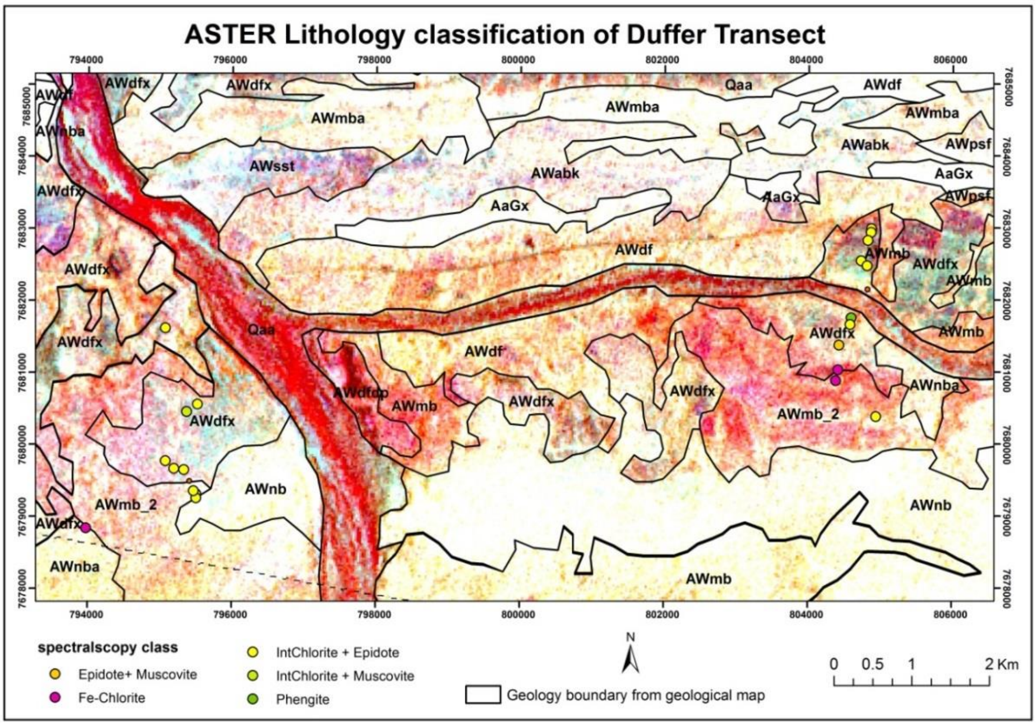

Figure 4-17: Map showing overlay of ASTER lithology classification form composite ratio_2 and laboratory spectroscopy interpretation on Duffer transect (Geological code description refers to appendix 8).

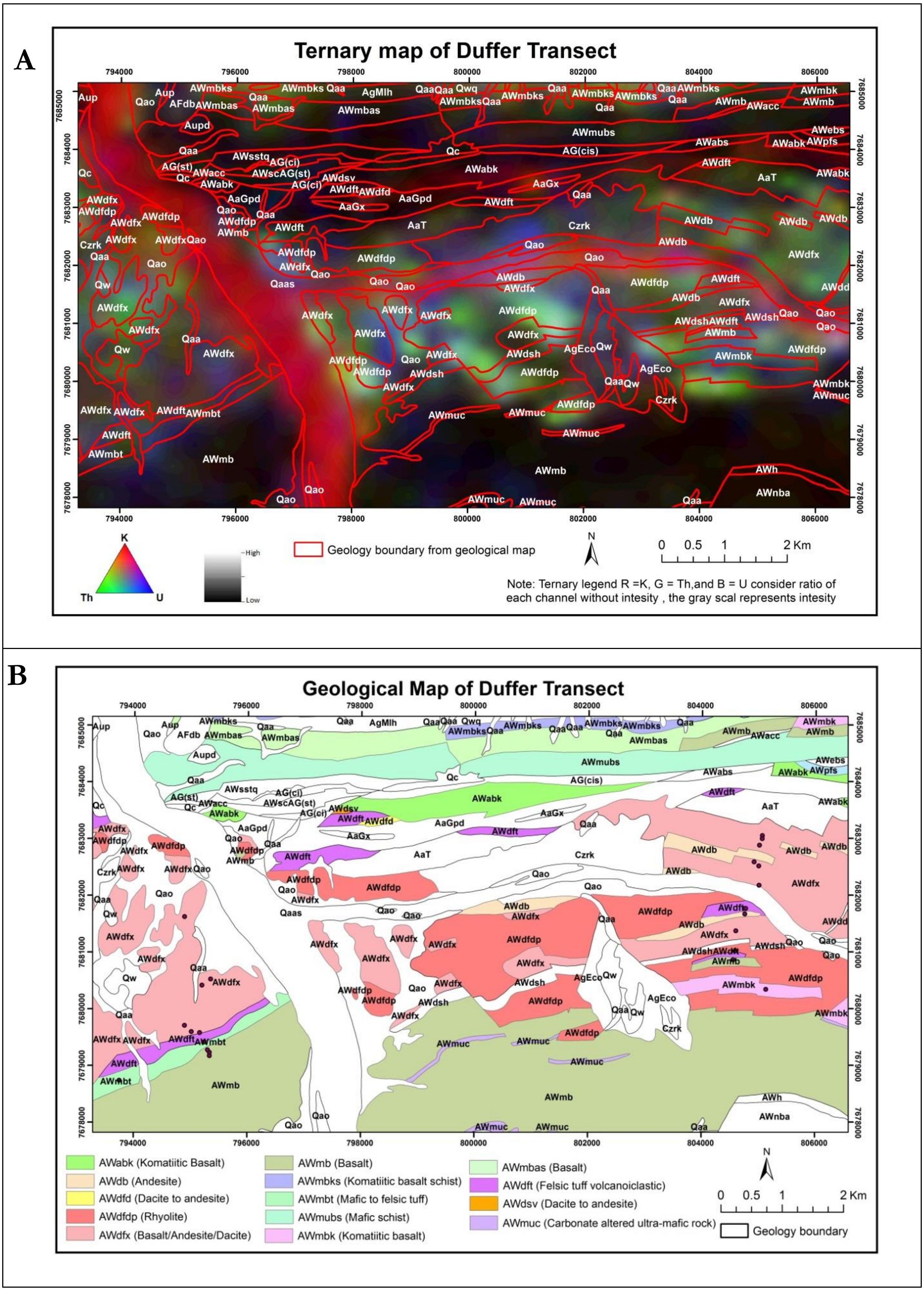

Figure 4-18: (A) Overlay of geological map on gamma-ray ternary image (B) Published geological map highlighting volcanic sequences of Duffer transect. (Geological code description refers to appendix 8).

4.5 Apex Transects

The Apex transect was used for validation the so far obtained results of ASTER mineralogical mapping and airborne gamma-ray chemical mapping. As described section 2.3.1.4, the Apex Formation is composed of komatiite and basalt. In the Warralong belt the basalt (AWabk) is commonly pillowed with local pyroxene spinifex texture. On ASTER image the lithology shows white pale green colour (Figure 4-19A). Spectral interpretation shows presence of intermediate chlorite, epidote, hornblende, Mg-chlorite and halloysite. The pale green might be related to high presence of MgOH mineral relative to ferrous iron and amphibole and epidotes. Though the image colour is different to that of Coonterunah basalt (AOt), mineral assemblage is similar. The difference in image colour might be due to MgOH abundance (Figure 4-9A).

In the Marble Bar belt the Apex basalt AWe and AWa on ASTER image shows pale yellow and light brown colour. The yellow relates to presence of relatively same abundance of Mg-chlorite and iron while the brown is due to high iron contents due to weathering. To the north-west the dark purple (AWeu) highlight hydrothermally altered quartzo feldspathic rhyolite that is metamorphosed to talc-chlorite schist (Figure 4-19D). Spectral interpretation of field data suggest present of Mg-chlorite, hornblende and epidote which is similar to Coonterunah AOt and its boundary with the Coucal Formation which is composed of intercalation of chert.

In both Warralong and Marble Bar greenstone belts airborne gamma-ray ternary map shows basalt in black signifying deficiency of K, Th and U (Figure 4-19 B and E). The results are similar to AOt basalt (Figure 4-9B). In figure 4-19E hydrothermally altered rocks shows a red spot on the northwest of the map. This indicates high presence of K .Mount Edgar granite on the south is shown in yellowish red indicating more K enrichment compared to Th and U. the Sky blue on the East of Mount Edgar granite indicate Uranium enrichment of Duffer Formation.

4.6 Mount Ada Transect

The Mount Ada transect was used for validation. In the Warralong belt, Mt Ada basalt (AWmbk) as described in section 2.3.1.3 is Komatiitic and commonly pillowed with local pyroxene spinifex texture. It shows a dark brown with cyan patches (Figure 4-19A). The dark brown is related to high presence of ferrous minerals while cyan is for relative present abundance of MgOH and amphiboles. The red colour is attributed to high iron content due to weathering. Spectral results of samples for the Mt Ada show presence on intermediate chlorite and epidote. Both image colour and mineral assemblages are same to those of AOd basalt of the Coonterunah transects. Although Apex and Mt Ada basalts are in the same greenstone belt ASTER shows their differences while airborne gamma-ray does not. The difference could be related to weathering that if influencing iron content in Mount Ada basalt.

4.7 Panorama Transect

As described in section 2.3.1.4 the Panorama Formation in the McPhee belt is a weakly metamorphosed felsic tuff with minor agglomerate that is locally silicified composed of andesitic basalt giving the lithology character of both mafic and intermediate rock. On ASTER image the lithology shows pale green, purple and cyan colours (Figure 4-20A). The pale green colour is similar to the Duffer Transect intermediate rocks AWdfx and felsic AWdfdp and could be related to Mg-chlorite together with the cyan while purple is associated alteration and presence of carbonates. Spectral interpretation identifies presence of intermediate chlorite, epidote and Fe-chlorite. These mineral were also identified in the Duffer formation which is dominated by intermediate lithology. Furthermore there is presence of halloysite signifying more weathering.

Airborne gamma-ray ternary image for the transect shows a north-south trends feature of yellowish-white, green and yellowish orange colours from west to east (Figure 4-20B). Yellowish-white indicates enrichment of K, Th and U, green indicates enrichment uranium and yellowish orange indicates of K and U. This suggests a chemical variation within the lithology. These minerals are possibly reached from sericite, carbonate, epidote and chlorite which occurs as secondary minerals

4.8 North Star Transect

The North Star basalt in the Marble Bar belt is generally massive and includes syn-volcanic dolerite intrusions which are locally schistose and metamorphosed. On ASTER image the lithology shows a cyan colour (AWAn-bb) which is similar to other basalts (Figure 4-21A). In areas where the basalt is metamorphosed to talc-carbonate and chlorite-serpentine schist (AWAn-mutk), the rock shows white brown pale green and light brown. Spectroscopic interpretation shows presence of intermediate chlorite, epidote, hornblende and halloysite. The hornblende is found in komatiitic basalt. Similar to other basalts, ternary image for the transect show black for low values of K, Th and U (Figure 4-21B).

4.9 Euro Transect

As described in Section 2.3.2, The Euro basalt appears in Strelley Panorama and Kelly belts. In East Strelley It is mainly composed of pillowed basalt of interbedded tholeiitic units of high Mg-basalt (AWebm). In the Kelly and McPhee the formation is composed of metamorphosed komatiitic basalt, metadolerite and pillowed tholeiitic basalt (A-KEe-bbo) and A-KEe-bk which is more komatiitic. On ASTER image AWebm show more green (Figure 4-22D), while A-KEe-bbo and A-KEe-bk show white, yellowish, and cyan. (Figure 4-22A) Spectral interpretation also show more occurrence of intermediate chlorite and epidote in AWebm while A-KEe-bbo and A-KEe-bk show more presence of hornblende, Mg-chlorite and actinolite compared to intermediate chlorite and epidote. The colour for dominant mineralogy for A-KEe-bbo and A-KEe-bk are similar to AOt basalt of the Coonterunah transects which also have Komatiite.

Ternary image for the two locations also show a subtle chemical difference. The AWebm in the East Strelley shows deep red colour (Figure 4-22E), while the in the McPhee and Kelly shows black (Figure 4-22 B). The black in the Kelly is similar to that of AOt which is also composed of komatiite (Figure 4-9B).

4.10 Charteris Transect

In the north East Kelly belt the Charteris is composed of metamorphosed tholeiitic basalt (AWbck). ASTER composite image shows the area in white to pale yellow. The colours are similar to the Coonterunah top part of the AOt and apex basalt (Awa) in the marble belt. Spectral results show presence of intermediate chlorite and epidote (Figure 4-23A). Furthermore, ternary image shows in black (4-23B)

Transects results of ASTER, and airborne gamma-ray were summarised and developed colour thresholds for classification (Table 4-7 and 4-8). The thresholds were applied in mapping the whole EPGGT volcanic sequences.

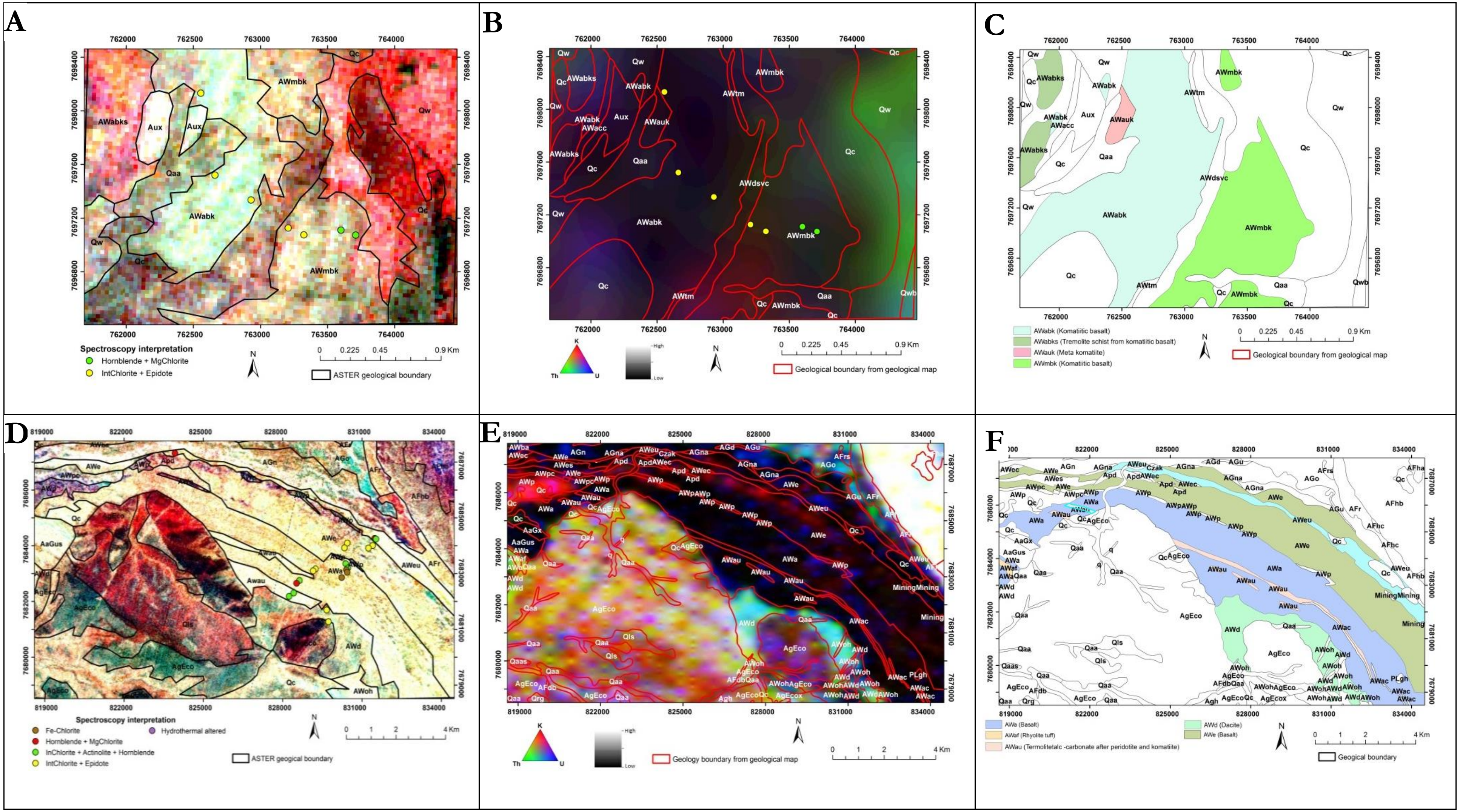

Figure 4-19: Apex and Mt Ada transect validation maps for (A and D) ASTER and (B and E) Overlay of gamma-ray geology map and (C and D) Geological maps in (A, B and C) Warralong belt and (D, E and F) Marble Bar belt. (Geological code description refers to appendix 12).

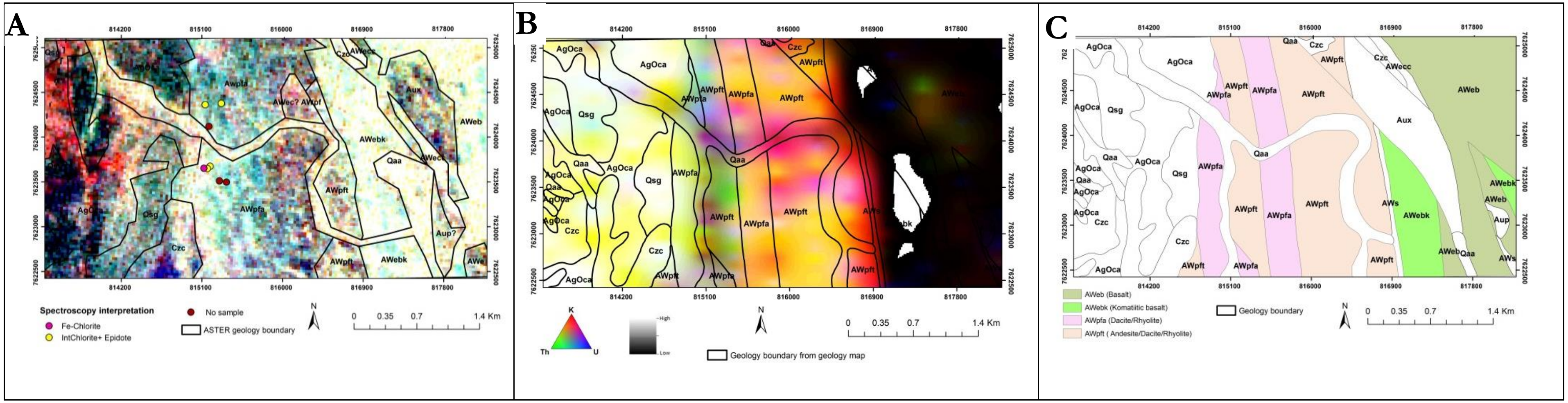

Figure 4-20: Panorama transect validation maps of (A) Overly of ASTER lithology classification and spectroscopy interpretation (B) Overlay of gamma-ray ternary map and geology and (C) Geology map highlighting volcanic sequences in McPhee belt. (Geological code description refers to appendix 12).

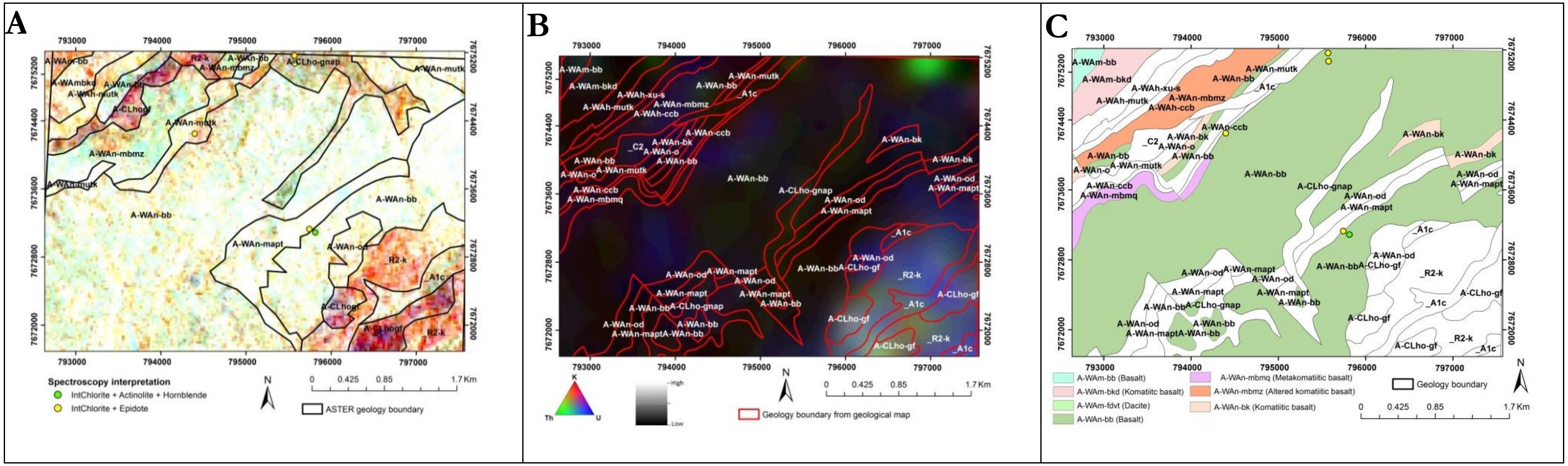

Figure 4-21: North Star Formation validation maps of (A) Overly of ASTER lithology classification and spectroscopy interpretation (B) Overlay of gamma-ray ternary map and geology and (C) Geology map highlighting volcanic sequences in Marble Bar belt. (Geological code description refers to appendix 12).

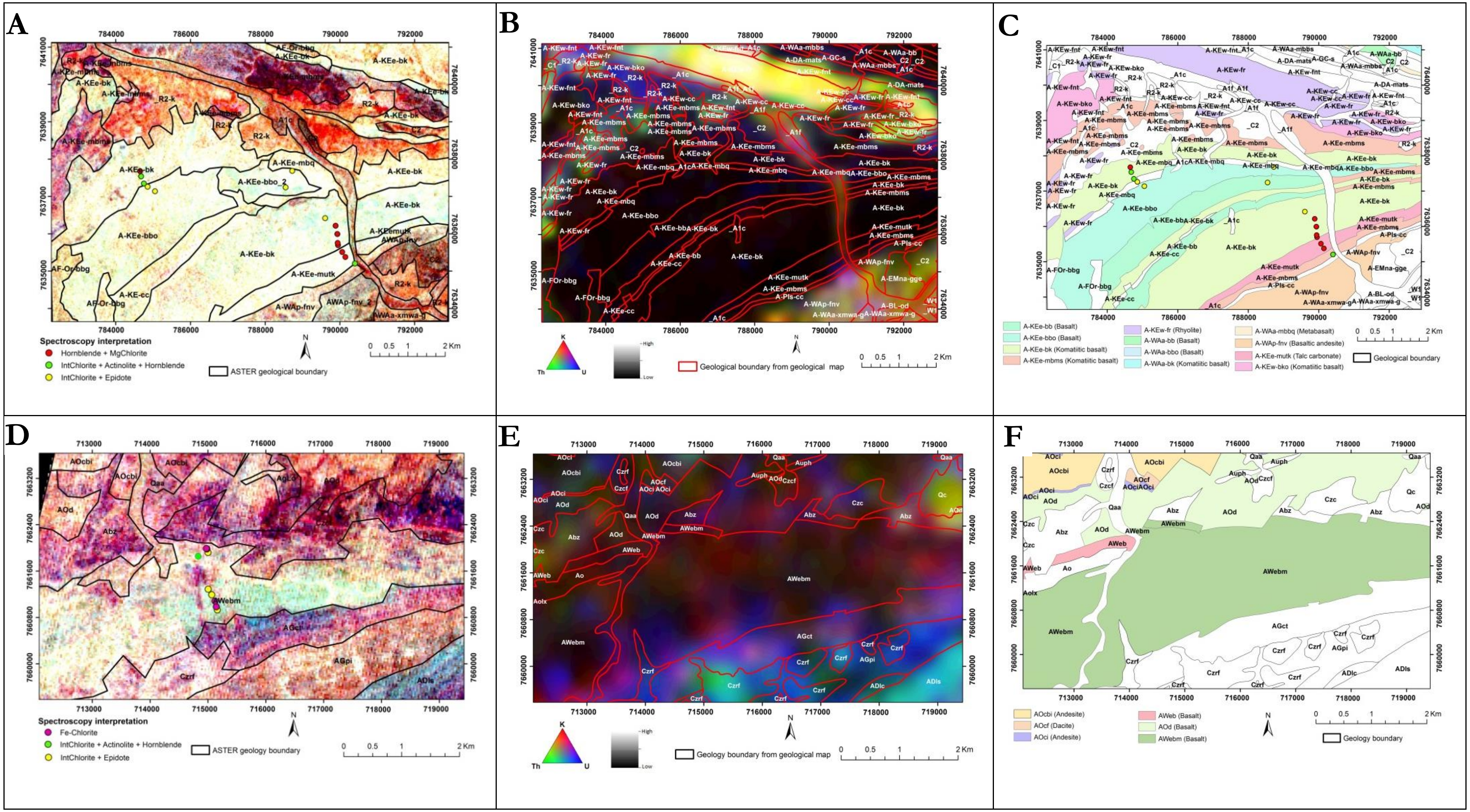

Figure 4-22: Euro transect validation maps of (A and D) ASTER lithology classification (B and E) Overly of gamma-ray ternary and geological map (C and F) Geological map highlighting volcanic sequence in (A, B and C) McPhee belts and (D, E and F) East Strelley. (Geological code description refers to appendix 12).

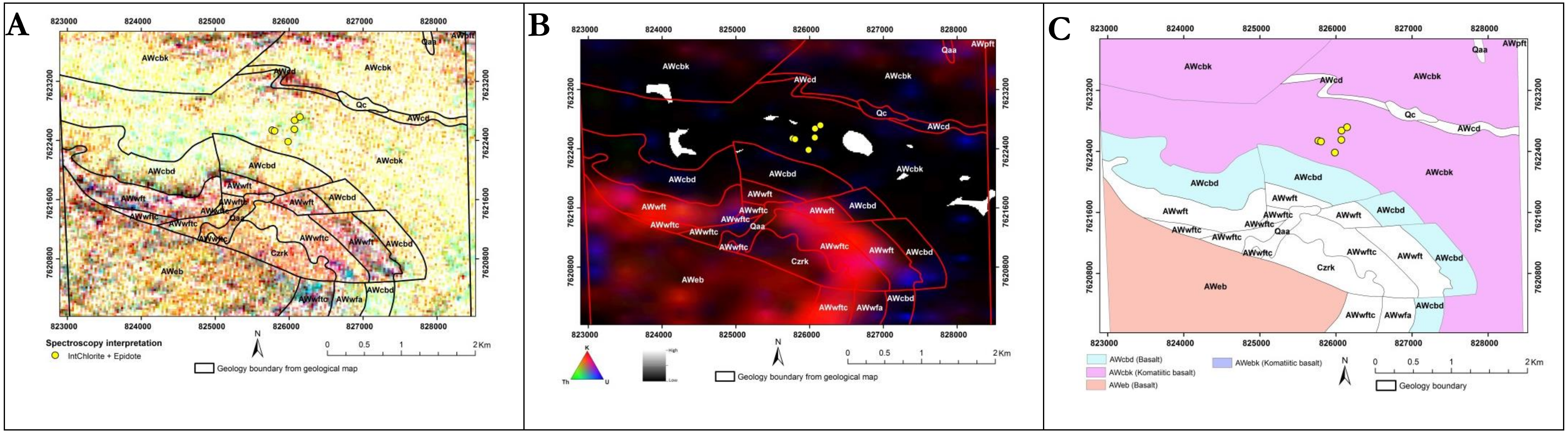

Figure 4-23: Charteris validation maps of (A) Overly of ASTER and geology map and (B) Overly of gamma-ray ternary map and geology map and (C) Geological map highlighting volcanic sequence in McPhee and Strelley belts. (Geological code description refers to appendix 12).

4.11 Image Classification and Integration

The most common way of presenting meaningful results to multispectral remote sensing data is through thematic maps (Foody and Mathur, 2004). It provides good representation of continuity and variability of image data giving pattern that can help to understand characteristic of features on ground.

This research used interactive supervised classification (maximum likehood) in ARC GIS software. Class training samples were from colour threshold that were developed from studying ASTER and airborne gamma-ray spectrometry datasets for Coonterunah, Duffer, Apex, Euro, North star, Panorama, Charteris and Mt Ada transects.(Tables 4-7 and 4-8). The results showed that ASTER could map volcanic sequence in three lithology classes thus; ultra-mafic and mafic, intermediate/felsic and intermediate/felsic altered (Figure 4-24B). On the other hand airborne gamma ray can map four classes thus; ultra-mafic, mafic, intermediate/felsic and intermediate/felsic altered (Figure 4-25B). Integration of ASTER and airborne gamma- ray showed that the EPGGT could be mapped into four classes thus; ultra-mafic, mafic, intermediate/felsic and intermediate/felsic altered (Figure 4-26B). Airborne gamma-ray was able to overcome effects of weathering that affects ASTER by improving lithology boundary. In addition airborne gamma-ray was able to discriminate ultra-mafic from mafic rock.

Accuracy assessment was applied by computing a confusion matrix crossing sampling point and classified lithology classes. Assessment considered number of sample pixel per class because sample numbers were not even per class. They were 99 basalt, 6 komatitie, 8 komatiitic basalt, 25 andesite, 23 dacite, 11 rhyolite, 1 peridotite dyke and 2 peridotite/komatiite and 6 unknown. Aster image shows an overall accuracy of 57.55%. Basalt and ultra-mafic lithology were mapped out well. There was confusion of basalt class with intermediate/felsic and intermediate/felsic altered. This is because the lithologies are coinciding Table 4-9. Similarly airborne gamma-ray shows overall accuracy of 56.00% with basalt confusing with intermediate/felsic and intermediate felsic altered rocks because they concede. Table 4-10. Integration of the two dataset would better map the volcanic sequence terrane as ultra-mafic, mafic, intermediate/felsic, and intermediate/felsic altered (Figure 4-26B).

	Transect								Classification	
Lithology	Coonterunah	Duffer	Apex	North Star	Mt Ada	Euro	Panorama	Charteris	Colour	Lithology
Peridotite/komatiite						white			White/pare yellow/light brown	Ultra-mafic and mafic
Komatiitic Basalt	White			White		white				
Basalt	White and light brown	White/pale brown/pale green/ pale yellow	White/ pale yellow,	Pale green/ light brown	Pale yellow / pale red	Pale green		White/ pale yellow		
Andesite	Cream and pale red	Cream and Pale red/pale green							Cream pale red /pale green/ purple/cyan	Intermediate or felsic
Dacite	Cream and Pale red	Cream and Pale red					Pale green/purple			
Rhyolite		Red (weathered)	Purple				Pale green/purple /cyan			Intermediate or felsic altered (with more purple)

Table 4-7: ASTER lithological colour scheme from composite ratio images.

	Transect								Classification	
Lithology	Coonterunah	Duffer	Apex	North Star	Mt Ada	Euro	Panorama	Charteris	Colour	Lithology
Peridotite/komatiite						Black			Black	Ultra-mafic
Komatiitic Basalt	Black					Black				
Basalt	Black/ Deep-red black	Black	Black	Black blue patches	Black	Deep red-black		Black with blue patches	Deep red, Black	mafic
Andesite	Deep red-black	Green, Blue, Red							mixture of green red purple and black	Intermediate or felsic
Dacite	Black/ Blue	Green, Blue, Red					Green, Purple,			
Rhyolite		Green, Blue, Red	Red- pink				Purple, Red ,Green			Intermediate or felsic altered (more red and purple)

Table 4-8: Airborne gamma-ray colour scheme from ternary image.

Class name	Ultra-mafic and mafic	Intermediate/felsic	Intermediate /felsic altered	Total	Overall accuracy	Error of omission	Producer accuracy
Peridotite dyke	225.00	0.00	0.00	225.00		0.00	100.00
Peridotite komatiite	450.00	0.00	0.00	450.00		0.00	100.00
Komatiitic basalt	900.00	450.00	0.00	1350.00		33.33	66.67
Komatiite	0.00	225.00	225.00	450.00		100.00	0.00
Basalt	8550.00	5175.00	4275.00	18000.00	57.55	52.50	47.50
Andesite	675.00	1575.00	900.00	3150.00		78.57	21.43
Dacite	1575.00	1125.00	2025.00	4725.00		66.67	33.33
Rhyolite	900.00	225.00	675.00	1800.00		50.00	50.00
No name	1125.00	0.00	0.00	1125.00		0.00	100.00
Total	14400.00	8775.00	8100.00	31275.00			
Error of commission	40.62	41.03	47.22	42.45			
User accuracy	59.38	58.97	52.78	57.55			

Table 4-9 : ASTER image accuracy summary.

Class name	Ultra-mafic	Mafic	Intermediate/ felsic altered	Intermediate /felsic	Total	Overall accuracy	Error of omission	Producer accuracy
Peridotite/komatiite	450.00	0.00	0.00	0.00	450.00		0.00	100.00
Komatiite	0.00	225.00	0.00	225.00	450.00		50.00	50.00
Komatiitic basalt	1125.00	675.00	0.00	0.00	1800.00		0.00	100.00
Basalt	5625.00	4500.00	3600.00	2025.00	15750.00	56.00	35.71	64.29
Andesite	225.00	675.00	450.00	675.00	2025.00		55.56	44.44
Dacite	225.00	900.00	2025.00	1125.00	4275.00		73.68	26.32
Rhyolite	0.00	1350.00	450.00	450.00	2250.00		40.00	60.00
no name	0.00	0.00	450.00	675.00	1125.00		100.00	0.00
Total	7650.00	8325.00	6975.00	5175.00	28125.00			
Error of commission	26.47	45.95	48.39	60.87				
User accuracy	73.53	54.05	51.61	39.13				

Table 4-10: Airborne gamma-ray accuracy summary.

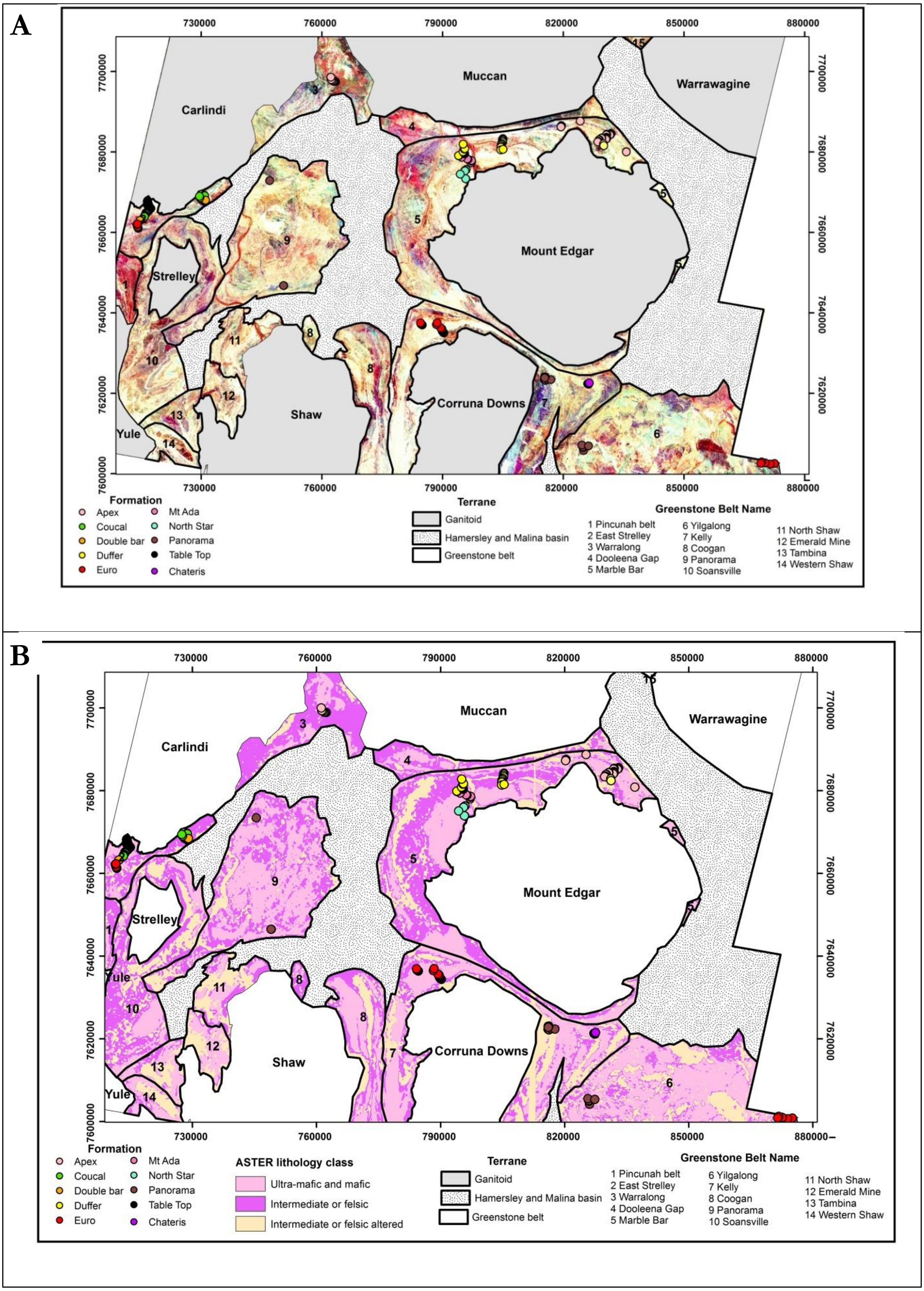

Figure 4-24: (A) ASTER unclassified composite image highlighting volcanic sequence (B) Classified lithology from ASTER thresholds.

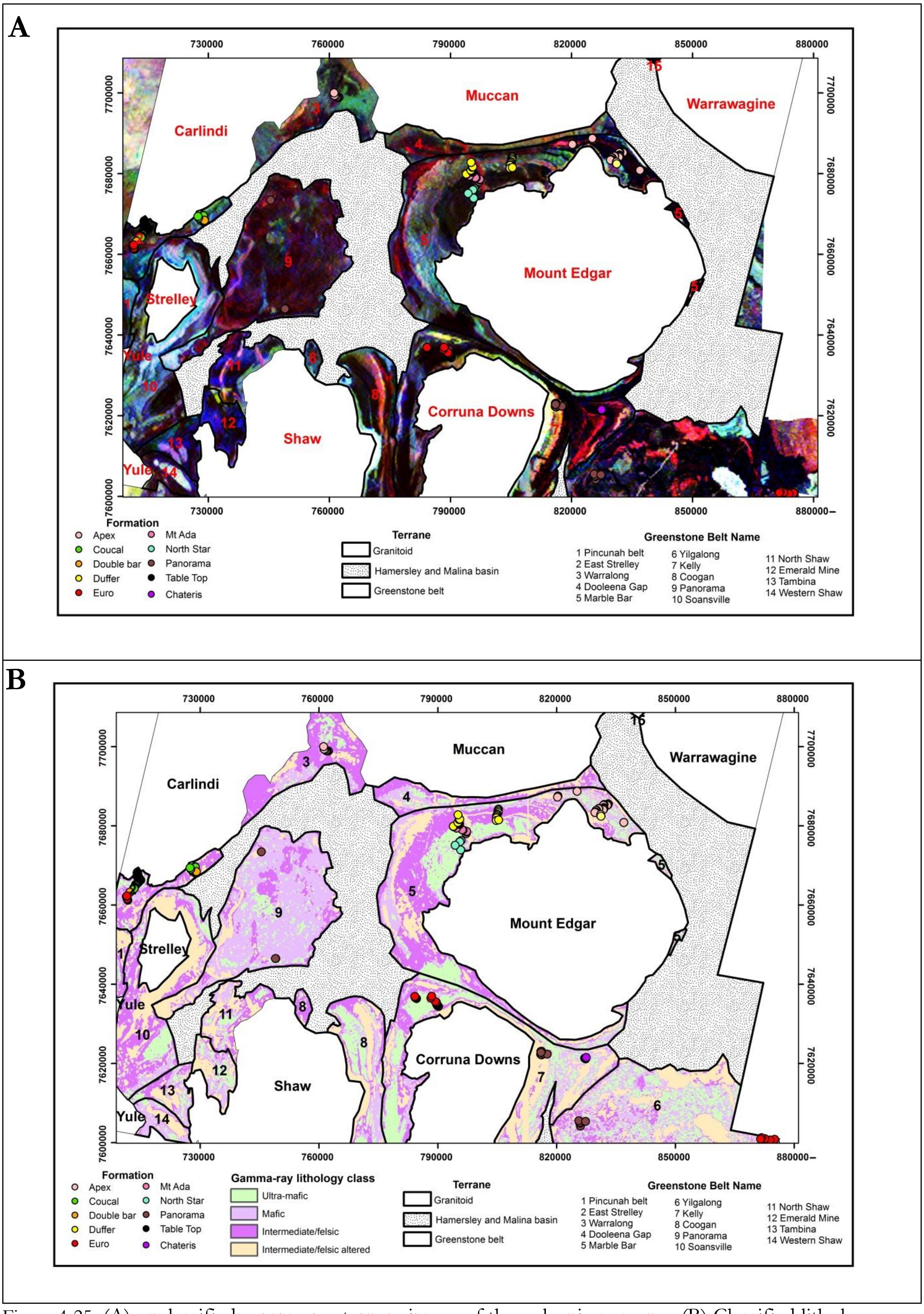

Figure 4-25: (A) unclassified gamma-ray ternary image of the volcanic sequence (B) Classified lithology from gamma-ray thresholds.

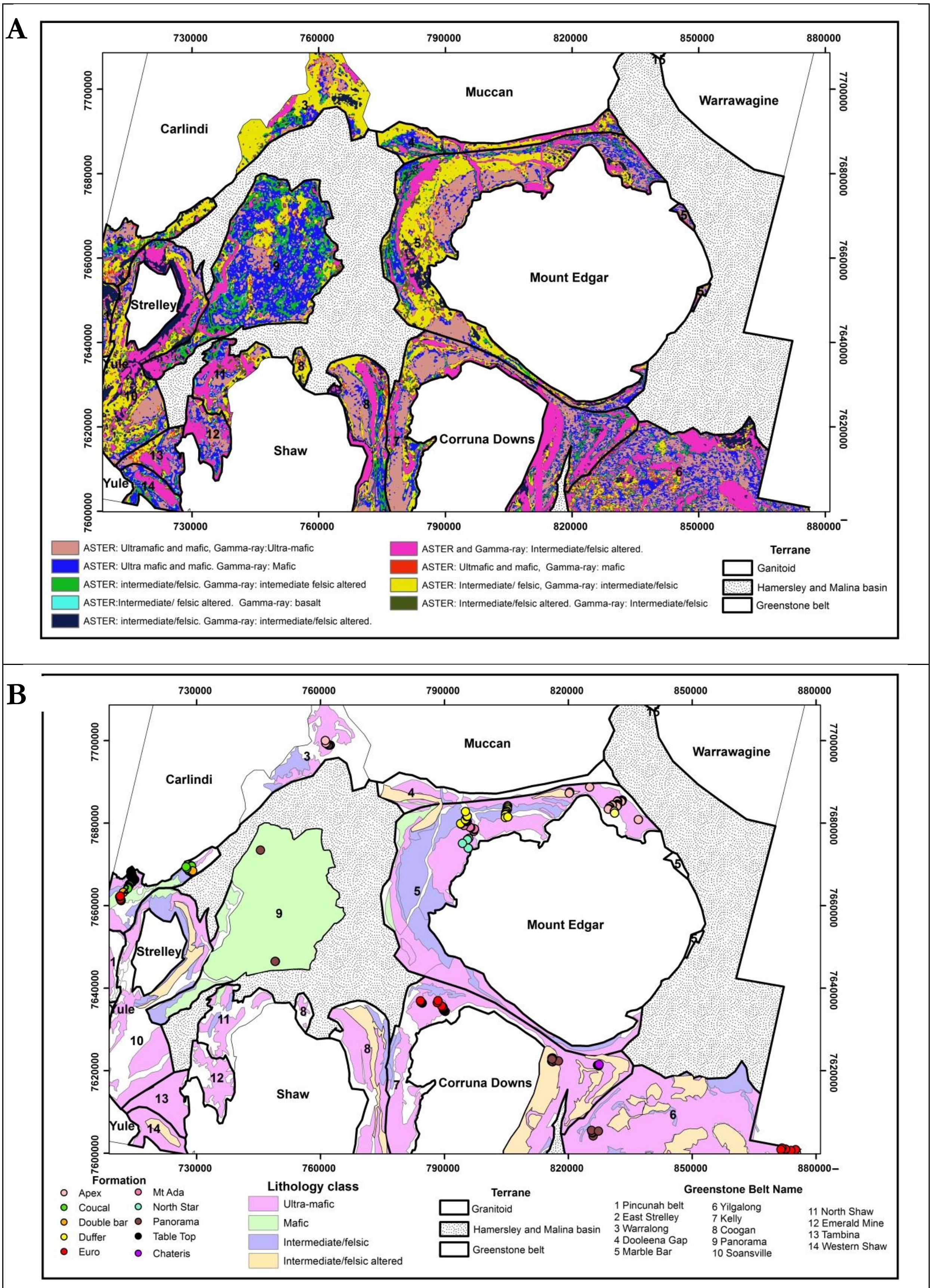

Figure 4-26: ASTER and Airborne gamma-ray classified integrated map(A) integrated map showing variations (B) Generalised map of the EPGGT after integration.

4 CONCLUSIONS AND RECOMMENDATION

This research assessed the extent to which airborne gamma-ray and ASTER image datasets could be integrated to map chemical and mineralogical variation in the volcanic sequence of EPGGT.

Airborne gamma-ray results show an average correlation with whole-rock laboratory geochemistry data. In both datasets potassium and thorium shows a similar increasing trend of measured values from ultra-mafic to intermediate/felsic rocks (Appendix 2 and 3). The trend in airborne gamma-ray is clear on distribution maps than on box plot due to little variation between lithology composition, survey parameter and pre-processing steps. The general linear trend observed in deviation plot could be used to correct airborne data. In addition potassium and thorium in both datasets shows lithology overlap between ultra-mafic and mafic rock and intermediate and felsic rock. Uranium in both cases does not show any trend due to its high mobile nature and possibly radon gas that also affects much its measurement.

The distinct variation in measured chemical value for thorium and potassium enables airborne gamma-ray to discriminated lithology. Low measurement values are related ultra-mafic and mafic classes (peridotite, komatiite, komatiite basalt and Basalt) and medium values to intermediate and felsic classes (andesite, dacite and rhyolite). Presence of Komatiite in ultramafic lithology depletes K, this enables discrimination between ultra-mafic and mafic lithology. On the other hand due to metamorphism/hydrothermal alteration K could discriminate intermediate/felsic lithology into altered and none altered. Therefore using airborne gamma-ray the EPGGT could be classed into Ultra-mafic (komatiite,), mafic (Basalt), intermediate/felsic (dacite/andesite/rhyolite) and intermediate/felsic altered (Dacite/andesite/rhyolite) (Table 4-8 and Figure 4-22). Accuracy assessment suggests and average mapping of 56% due to coinciding of lithology and little chemical variation.

The results of ASTER analysis shows that ratios (5/3) + (1/2), (6+9)/8 and (7+9)/8 which highlight ferrous iron, amphibole, MgOH, and carbonate chlorite and epidote respectively are useful in mapping mineralogical variation when assign to red, green and blue channels respectively. Minerals that can be detected are Mg-chlorite, hornblende, epidote, actinolite, and intermediate chlorite, halloysite, illite, iron oxides and hydroxides. Of these ASTER detectable minerals hornblende is the only mineral significant for lithological characterisation. It is found in ultramafic rocks only. At a regional scale ASTER could classify the whole greenstone terrane into ultra-mafic and mafic, intermediate/felsic and intermediate/felsic altered (Table 4-7 and Figure 4-24).Accuracy assessment suggest 57%.

Integration of ASTER and airborne gamma-ray results compliments each other well. ASTER image potential for mapping mineral variation and boundaries that is being affected by surface soils and iron cast covering rock surfaces due weathering could be overcome by airborne gamma-ray which was able to penetrate the surface soils and iron cast delineating better lithology boundary (Figure 4-26B). Furthermore airborne gamma-ray could was able to discriminating ultramafic and mafic which improved integrated results. Therefore lithologies which are being mapped well are Ultramafic, mafic intermediate/felsic altered.

5.1 Recommendation

Based on the results of this research the following recommendations are made:

- There is need to have more geochemical sample to highlight the subtle variation between lithologies. Parallel transect would also help to analyse the variation.
- The Australian Geological Survey defines the airborne gamma-ray survey data used in this research as semi detailed. There is need to compare it with a detailed survey results to determine if felsic and intermediate lithology could be discriminated
- Hyper spectral imagery would help to determine if there are any other minerals significant for lithological characterisation.
- There is need to investigate if the linear trend on deviation plots could be used to correct for airborne gamma-ray.
- There is need to investigate alternative means of comparing ASTER imagery spectra directly with laboratory spectra ratio to see if results would be improved.

LIST OF REFERENCES

Abrams, M: Hook, S. (2001). *ASTER Users Handbook version 2*. Retrieved from Earth Remote Sensing Data Analysis Center (2000) http://www.ersdac.or.jp/

Abweny, M. S. M. (2012). *Near infrared spectroscopy of low grade metamorphic volcanic rocks of the east Pilbara granite greenstone terrane Australia*. Retrieved from http://www.itc.nl/library/papers_2012/msc/aes/abweny.pdf

Anderson, K. F. E. (2003). *Radioelement Indicators for Hydrothermal Alteration in the Panorama VHMS District , Western Australia*. Retrieved from http://www.itc.nl/library/papers_2003/msc/ereg/anderson.pdf

Barley, M. E. (1998). Archean volcanic-hosted massive sulphides. *Australian Geology and Geophysics*, *17*(4), 69 – 73.

Bayanjargal, O. (2004). *Regional Alteration Mapping for Volcanic-hosted Massive Sulphide Exploration in the Pilbara , Australia*. Retrieved from http://www.itc.nl/library/papers_2004/msc/ereg/oyungerel_bayanjargal.pDF

Bickle, M. J., Bettenay, L. F., Chapman, H. J., Groves, D. I., McNaughton, N. J., Campbell, I. H., & de Laeter, J. R. (1989). The age and origin of younger granitic plutons of the Shaw Batholith in the Archaean Pilbara Block, Western Australia. *Contributions to Mineralogy and Petrology*, *101*(3), 361–376. doi:10.1007/BF00375320

Clark, R. N. (1999). Chapter 1: Spectroscopy of Rocks and Minerals, and Principles of Spectroscopy, in Manual of Remote Sensing. *Remote Sensing for the Earth Sciences*, *3*, 3 – 58.

Dentith, M. and M. S. T. (2014). Potassium, uranium and thorium in igneous rocks. In *Geophysics for the Mineral Exploration Geoscientist* (first., pp. 210 – 217). Cambridge University Press.

Dickson, B. L., Fraser, S. J., & Kinsey-Henderson, A. (1996). Interpreting aerial gamma-ray surveys utilising geomorphological and weathering models. *Journal of Geochemical Exploration*, *57*(1-3), 75–88. doi:10.1016/S0375-6742(96)00017-9

Eberle, D. G., & Paasche, H. (2012). Integrated data analysis for mineral exploration: A case study of clustering satellite imagery, airborne gamma-ray, and regional geochemical data suites. *Geophysics*, *77*(4), B167. doi:10.1190/geo2011-0063.1

Ehlers, M., Greenlee, D., Smith, T., & Star, J. (1991). Integration of Remote Sensing and GIs : Data and Data Access. *Photogrammetric Engineering and Remote Sensing*, (6), 669–675.

Foody, G. M., & Mathur, A. (2004). Toward intelligent training of supervised image classifications: directing training data acquisition for SVM classification. *Remote Sensing of Environment*, *93*(1-2), 107–117. doi:10.1016/j.rse.2004.06.017

Ghatak, A., Basu, A. R., & Wakabayashi, J. (2012). Elemental mobility in subduction metamorphism: insight from metamorphic rocks of the Franciscan Complex and the Feather River ultramafic belt, California. *International Geology Review*, *54*(6), 654–685. doi:10.1080/00206814.2011.567087

Hastie, A. R., Kerr, A. C., Pearce, J. A., & Mitchell, S. F. (2007). Classification of Altered Volcanic Island Arc Rocks using Immobile Trace Elements: Development of the Th Co Discrimination Diagram. *Journal of Petrology*, *48*(12), 2341–2357. doi:10.1093/petrology/egm062

Hickman A.H, V. K. (2006). *Early Earth evolution: evidence from the 3 . 5 – 1 . 8 Ga Geological history of the Pilbara region of Western* (pp. 283–297).

International Atomic Energy Agency. (2003). *Guidelines for Radioelement mapping using gamma ray spectrometery data*. Retrieved from http://www-pub.iaea.org/MTCD/publications/PDF/te_1363_web.pdf

Kanlinowsk I, A. and Oliver, S. (2004). *ASTER Mineral Index Processing Manual. Remote Sensing Application Geoscience Australia.* Retrieved from http://www.ga.gov.au/image_cache/GA7833.pdf

Kerry, P. F. (1952). Formation and Occurence of Clay minerlas. *Clays and Clay Minerals*, 19 – 32. doi:10.1346/CCMN.1952.0010104

Le Maitre, R. W. (2002). *Igneous Rocks*. (D. a. Le Maitre R.W, Streckeisen A., Zanettin B., Le Bas M.J., Bonin B., Bateman P., Bellieni G. & W. A. . Efremova, S., Keller, J., Lameyre J., Sabine P.A., Schmid R., Sørensen H., Eds.) (Second.). Cambridge University Press.

Lillesand, T. ., & Kiefer, R. . (1987). *Remote sensing and image interpretation* (p. 721). New york: Wiley and Sons.

Milsom, J. and Eriksen, A. (2007). *Field Geophysics* (4th ed., p. 244). John Wiley and Sons.

Nesbitt, R.W., Sun, S.S., and Puruvis, A. C. (1977). Komatiities geochemistry and gneissis. *Canadian Mineralogist*, *17*, 165 – 186.

Pablo, R., & Palomera, A. D. (2004). *Application of Remote Sensing and Geographic Information Systems for Mineral Predictive Mapping , Deseado Massif , Southern Argentina by*. Retrieved from http://www.itc.nl/library/papers_2004/msc/ereg/andrada_de_palomera.pdf

Richardson, L. M. (2004). *Index of Airborne Geophysical Surveys Compiled (Eighth edition).*

Smithes, R. H., Champion, D. C., Kranendonk, M. J. Van, & Hickman, A. H. (2007). *Geochemistry of volcanic rocks of the northern Pilbara Craton,Western Australia: Western Australia Geological Survey* (p. Report 104, p47).

Thuss, B. (2005). *Spectroscopic study of Early Archean volcanic rocks in the Pilbara Craton (Western Australia).* Universisy of Delft.

Van der Meer, F. D., van der Werff, H. M. A., van Ruitenbeek, F. J. A., Hecker, C. A., Bakker, W. H., Noomen, M. F., van der Meijde, M., Carranza, E.J.M., Smeth, J.B. &Woldai, T. (2012). Multi- and hyperspectral geologic remote sensing: A review. *International Journal of Applied Earth Observation and Geoinformation*, *14*(1), 112–128. doi:10.1016/j.jag.2011.08.002.

Van Kranendonk. (2004). The Geology of Carlindie 1:100 000 sheet: Western Australia Geological Survey. *1:100 000 Geological Series Explanatory Notes*, 45p.

Van Kranendonk, M. J. (2000). Geology of the North Shaw 1: 100 000 sheet: Western Australia Geological Survey. *1:100 000 Geological Series Explanatory Notes*, 86p.

Van Kranendonk, M. J. (2003). Geologiy of the Tamourah 1: 100 000 sheet: Western Australia Geological Survey. *1:100 000 Geological Series Explanatory Notes*, 57p.

Van Kranendonk, M. J. (2010). The Geology of Coongan 1:100 000 sheet: Western Australia Geological Survey. *1:100 000 Geological Series Explanatory Notes*, 67p.

Van Kranendonk, M. J., Hickman, A. H., Smithies, H. R., R, N. D., & Geoff Pike. (2002). Geology and Tectonic Evolution of the Archean North Pilbara Terrain , Pilbara Craton , Western Australia. *Economic Geology*, *97*(4), 695–732. doi:10.2113/gsecongeo.97.4.695

Van Kranendonk, M. J., Hugh Smithies, R., Hickman, A. H., & Champion, D. C. (2007). Review: secular tectonic evolution of Archean continental crust: interplay between horizontal and vertical processes in the formation of the Pilbara Craton, Australia. *Terra Nova*, *19*(1), 1–38. doi:10.1111/j.1365-3121.2006.00723.x

Van Kranendonk, M. J., Hickman, A. H., Smithies, R. H., Williams, I. R., Bagas, L., Farrell, T. R. (2006). Revised lithostratigraphy of Archean supracrustal and intrusive rocks in the northern Pilbara Craton, Western Australia, 57.

Van Ruitenbeek, F. J. a., Cudahy, T., Hale, M., & van der Meer, F. D. (2005). Tracing fluid pathways in fossil hydrothermal systems with near-infrared spectroscopy. *Geology*, *33*(7), 597. doi:10.1130/G21375.1

Van Ruitenbeek, F. J. A., Cudahy, T. J., van der Meer, F. D., & Hale, M. (2012). Characterization of the hydrothermal systems associated with Archean VMS-mineralization at Panorama, Western Australia, using hyperspectral, geochemical and geothermometric data. *Ore Geology Reviews*, *45*, 33–46. doi:10.1016/j.oregeorev.2011.07.001

Van Ruitenbeek, F. J. A., Debba, P., van der Meer, F. D., Cudahy, T., van der Meijde, M., & Hale, M. (2006). Mapping white micas and their absorption wavelengths using hyperspectral band ratios. *Remote Sensing of Environment*, *102*(3-4), 211–222. doi:10.1016/j.rse.2006.02.012

Wilson. (1999). The Origin and Formation of Clay Minerals in the Soil; Past Present and Future Perspective. *Clay Minerals*, *34*(1), 7 – 25.

Zhang, X., Pazner, M., & Duke, N. (2007). Lithologic and mineral information extraction for gold exploration using ASTER data in the south Chocolate Mountains (California). *ISPRS Journal of Photogrammetry and Remote Sensing*, *62*(4), 271–282. doi:10.1016/j.isprsjprs.2007.04.004

APPENDICES

Appendix 1: Geological map and lithology code description table of Coonterunah transects

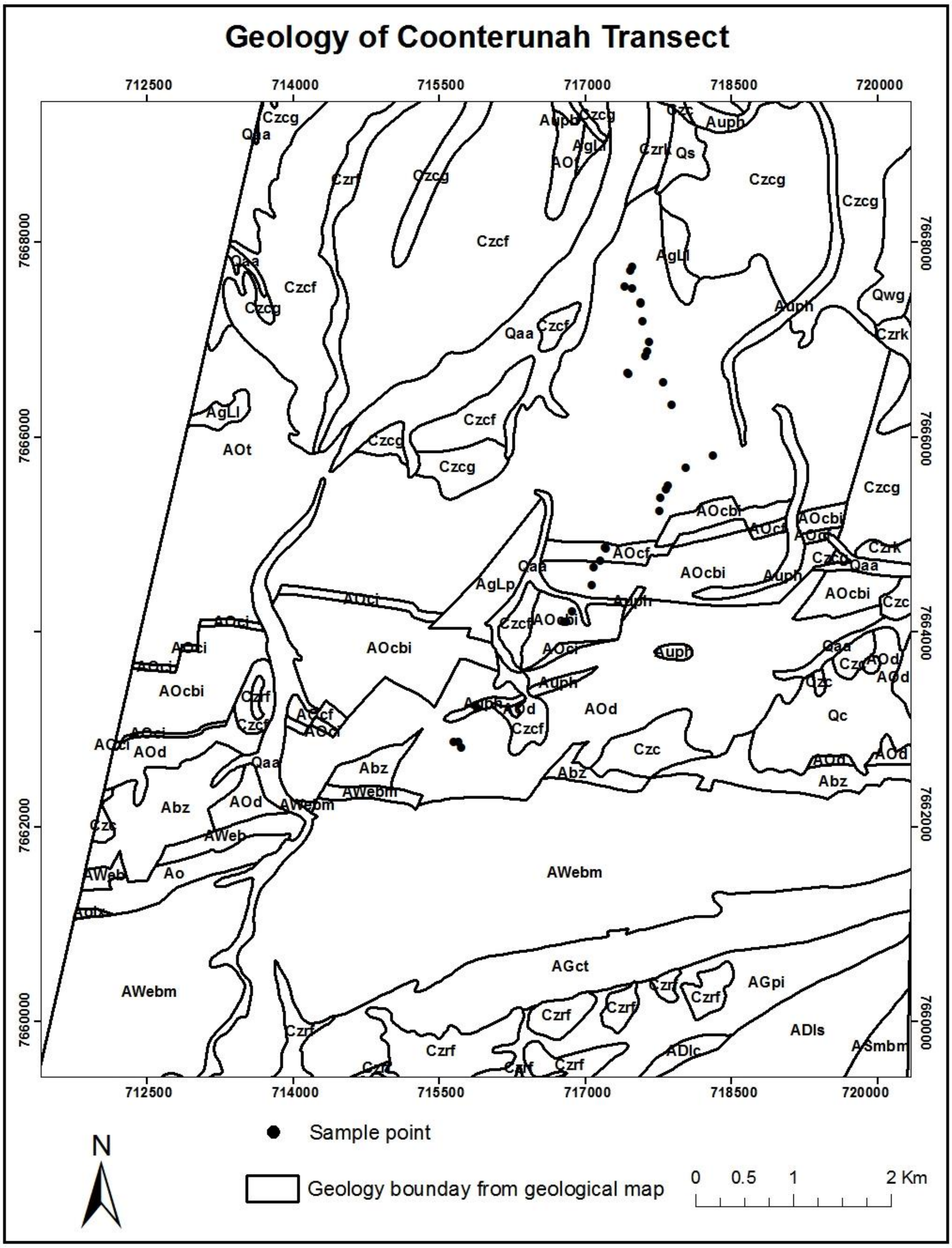

Subgroup	Formation	Symbol	Description
	Un assigned	Aup	Metamorphosed serpentinized peridotite and serpentine-chlorite schist
		Abz	Silicified and sericitized basaltic rock; local felsic volcanic rock
		Qs	Eolian sand - orange to light red sand in undulating sheets
		Qwg	Sheet wash sand and quartz pebbles overlying and derived from granitoid rocks
		Qc	Eolian sand - orange to light red sand in undulating sheets
		Qaa	Sand and gravel in rivers and creeks
		Czcg	Clay, silt, sand, and gravel derived from granitoid rock; variably consolidated and dissected
		Czc	Colluvium - dissected consolidated clay, silt, and sand deposits; derived from adjacent rock outcrop
		Czcf	Ferruginous silt, sand, and gravel; variably consolidated and dissected
		Czrf	Ferruginous duricrust; includes massive, pisolitic, and nodular laterite, and consolidated ferruginous alluvium
Golds worthy	Lala rook Sst/ Paradise	ADls	Coarse to pebbly sandstone and pebble conglomerate; minor siltstone and grey shale; weakly metamorphosed
		ADlc	Pebble to boulder conglomerate and interbedded pebbly to coarse sandstone; weakly metamorphosed
Soansville	Paddy Market	AGpi	Thinly bedded black, white, red, and grey, cherty banded iron-formation; minor ferruginous shale; weakly metamorphosed
	Corboy	AGct	Sandstone, with pebble conglomerate interbeds; local siltstone and shale; weakly metamorphosed
	Six Mile creek	ASmbm	High-Mg basalt; metamorphosed
	Euro Basalt	AWeb	Tholeiitic and high-Mg basalt, and dolerite sills; metamorphosed
		AWebk	Komatiitic basalt, as lavas and subvolcanic intrusions; metamorphosed
		AWebm	High-Mg basalt, commonly pillowed; metamorphosed
	Strelley pool chert	AWs	Laminated grey and white chert; includes silicified siliciclastic and chemical sedimentary rocks; stromatolitic; local carbonate rock; metamorphosed
Coonterunah	Double Bar	AOd	Massive tholeiitic basalt; locally pillowed and schistose; metamorphosed
	Coucal	AOcbi	Andesite to basalt; metamorphosed
		AOcf	Felsic volcanic rocks; local felsic agglomerate; metamorphosed
		AOci	Cherty banded iron-formation; black and white, and rarely red layered; metamorphosed
Carlindi intrusion	Granitoid complex	AgLI	Biotite-hornblende leucogranite
		AgLmh	Hornblende-phyric monzogranite
		AgLp	Quartz-feldspar porphyry; high-level equivalent of AgLI
Coonterunah	Table Top	AOt	Fine- to medium-grained metabasalt, metadolerite, and amphibolite

Appendix 2: Cooneterunah transect box plots showing comparison of potassium thorium and uranium contents measured with whole-rock laboratory geochemistry and airborne gamma-ray spectrometry.

<table>
<tr><th>Laboratory whole-rock geochemical data Box plot</th><th>Airborne gamma-ray data Box plots</th></tr>
<tr><td>Potassium</td><td>Potassium</td></tr>
<tr><td>
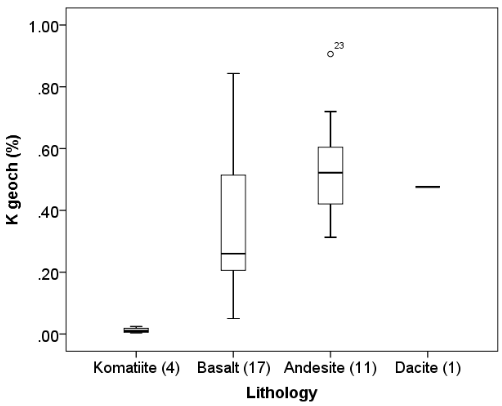

</td><td>
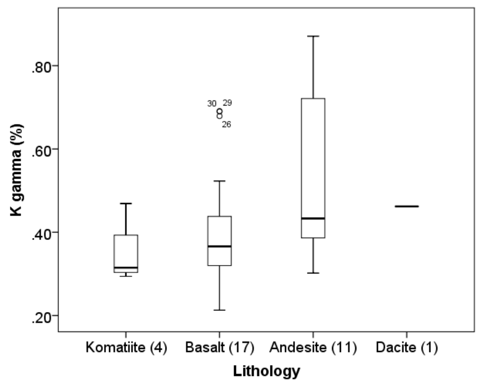

</td></tr>
<tr><td>Thorium</td><td>Thorium</td></tr>
<tr><td>
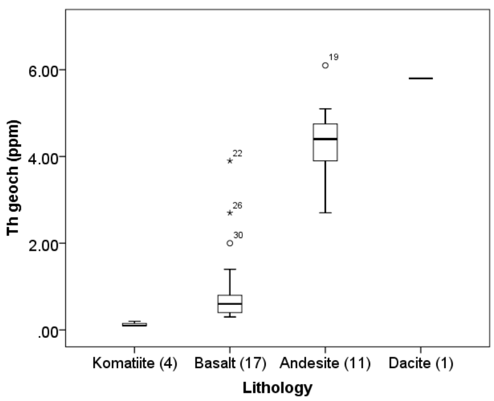

</td><td>
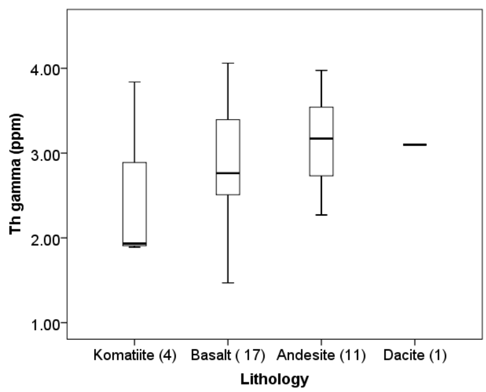

</td></tr>
<tr><td>Uranium</td><td>Uranium</td></tr>
<tr><td>
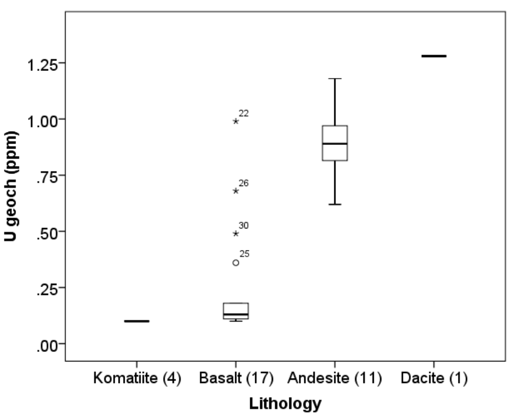

</td><td>
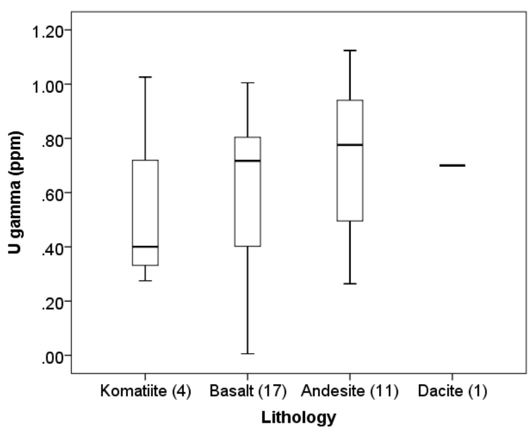

</td></tr>
</table>

Appendix 3: Thorium, Potassium and Uranium distribution map for Coonterunah transect with estimation classes.

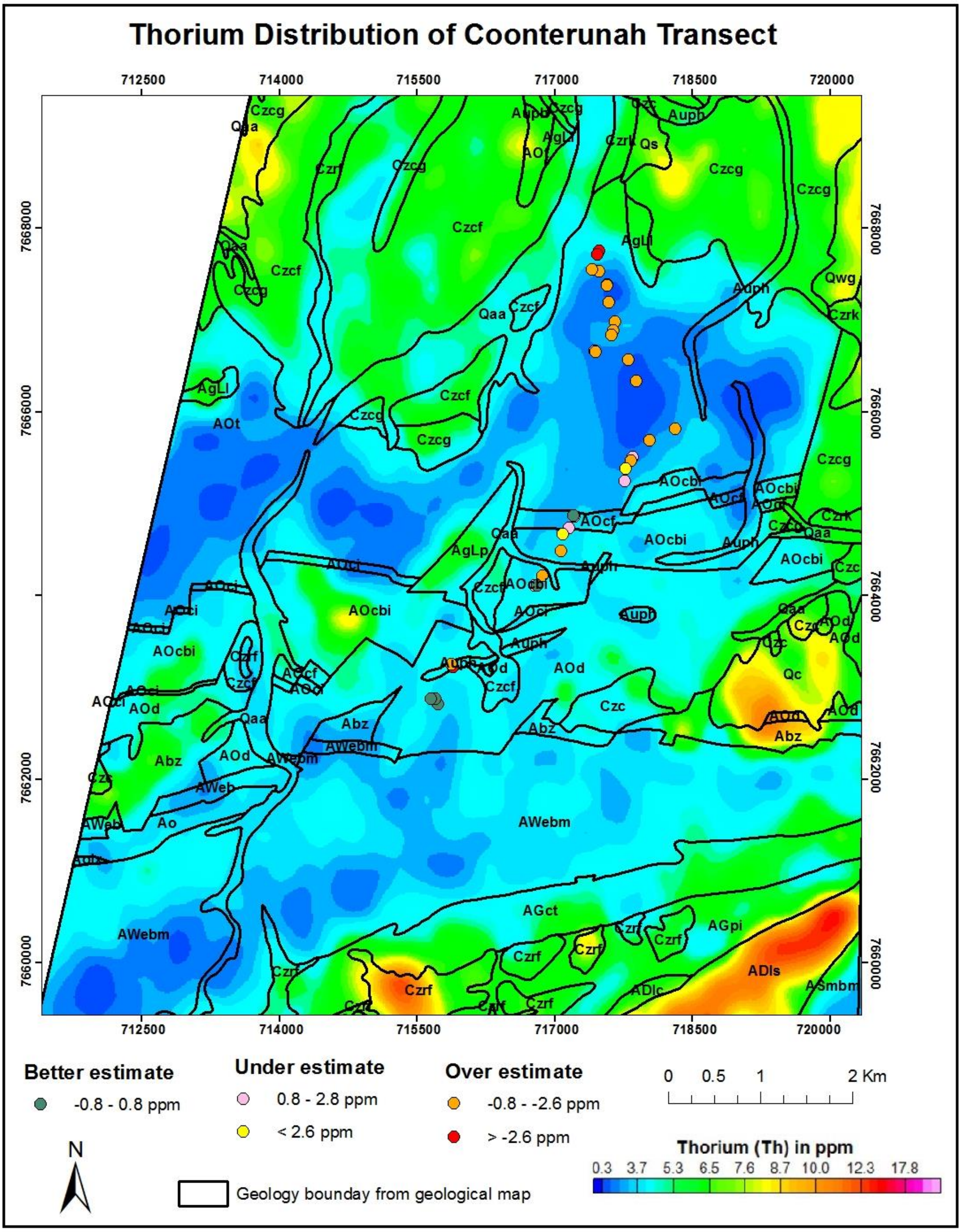

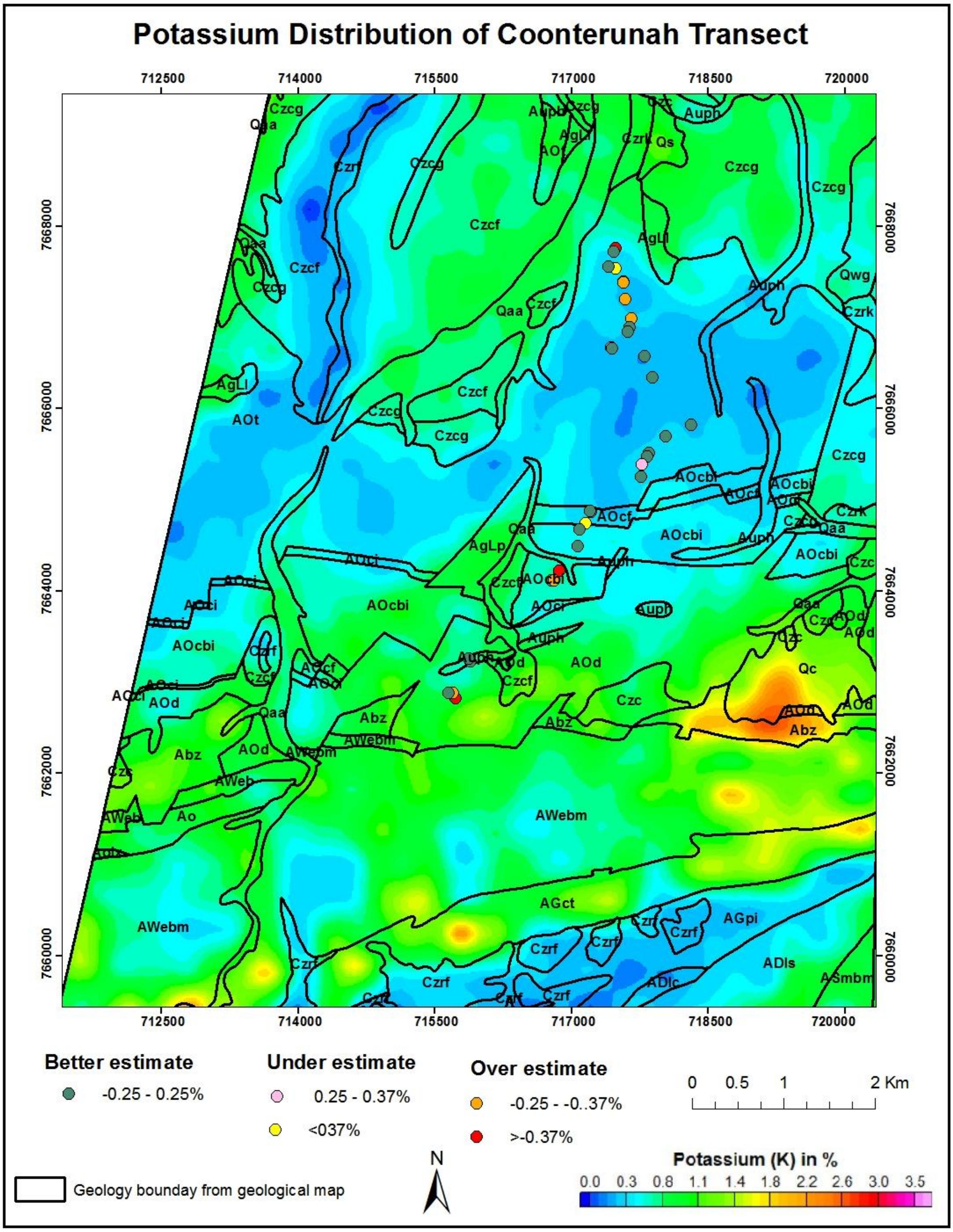
Potassium Distribution of Coonterunah Transect
712500
714000
715500
717000
718500
720000
7668000
7666000
7664000
7662000
7660000
Better estimate
-0.25 - 0.25%
Under estimate
0.25 - 0.37%
<037%
Over estimate
-0.25 - -0..37%
>-0.37%
0 0.5 1 2 Km
N
Potassium (K) in %
0.0 0.3 0.8 1.1 1.4 1.8 2.2 2.6 3.0 3.5
Geology bounday from geological map

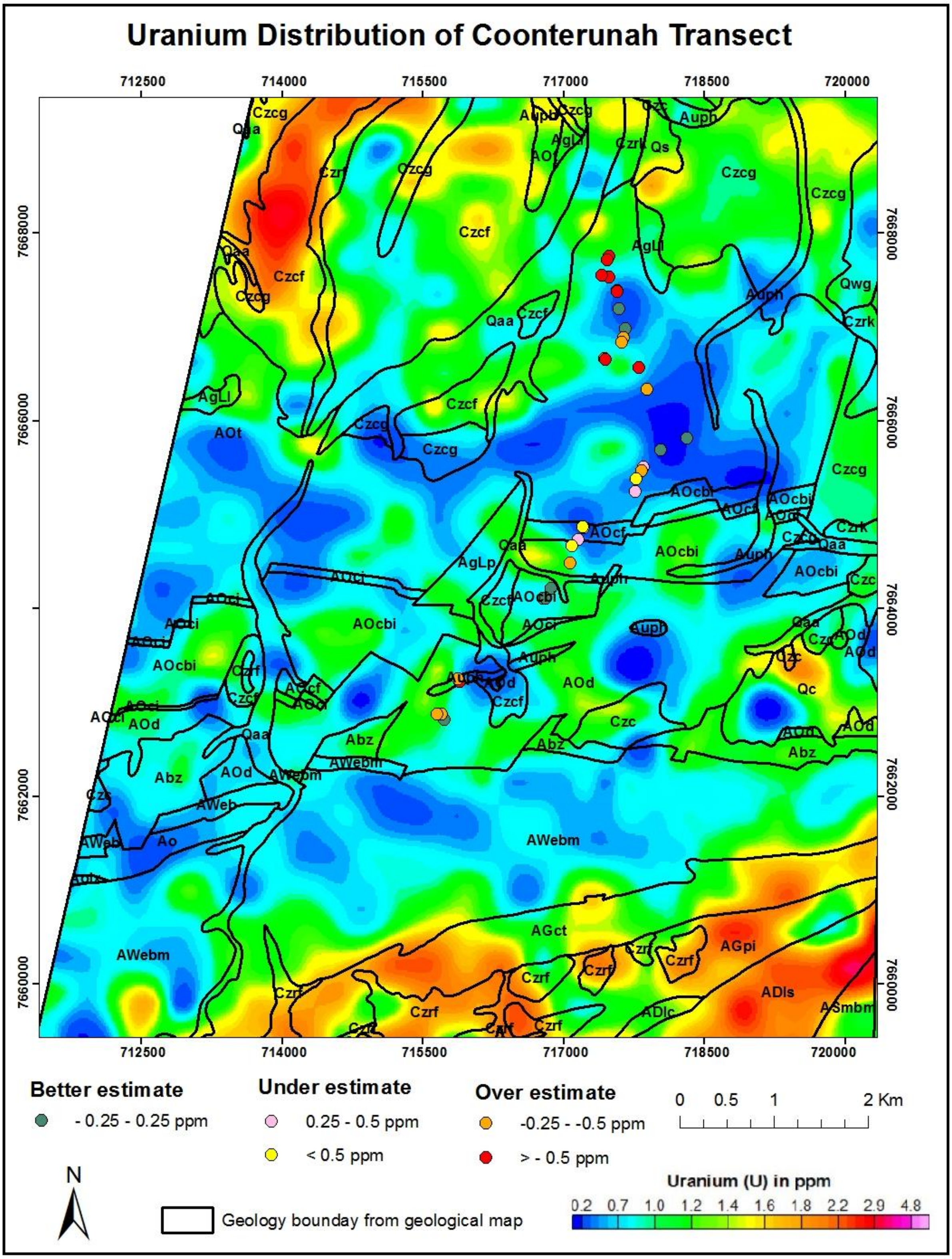
Uranium Distribution of Coonterunah Transect
712500
714000
715500
717000
718500
720000
7668000
7666000
7664000
7662000
7660000
Better estimate
- 0.25 - 0.25 ppm
Under estimate
0.25 - 0.5 ppm
< 0.5 ppm
Over estimate
-0.25 - -0.5 ppm
> - 0.5 ppm
0 0.5 1 2 Km
N
Geology bounday from geological map
Uranium (U) in ppm
0.2 0.7 1.0 1.2 1.4 1.6 1.8 2.2 2.9 4.8

Appendix 4: Coonterunah profiles comparing for potassium thorium and uranium with relief.

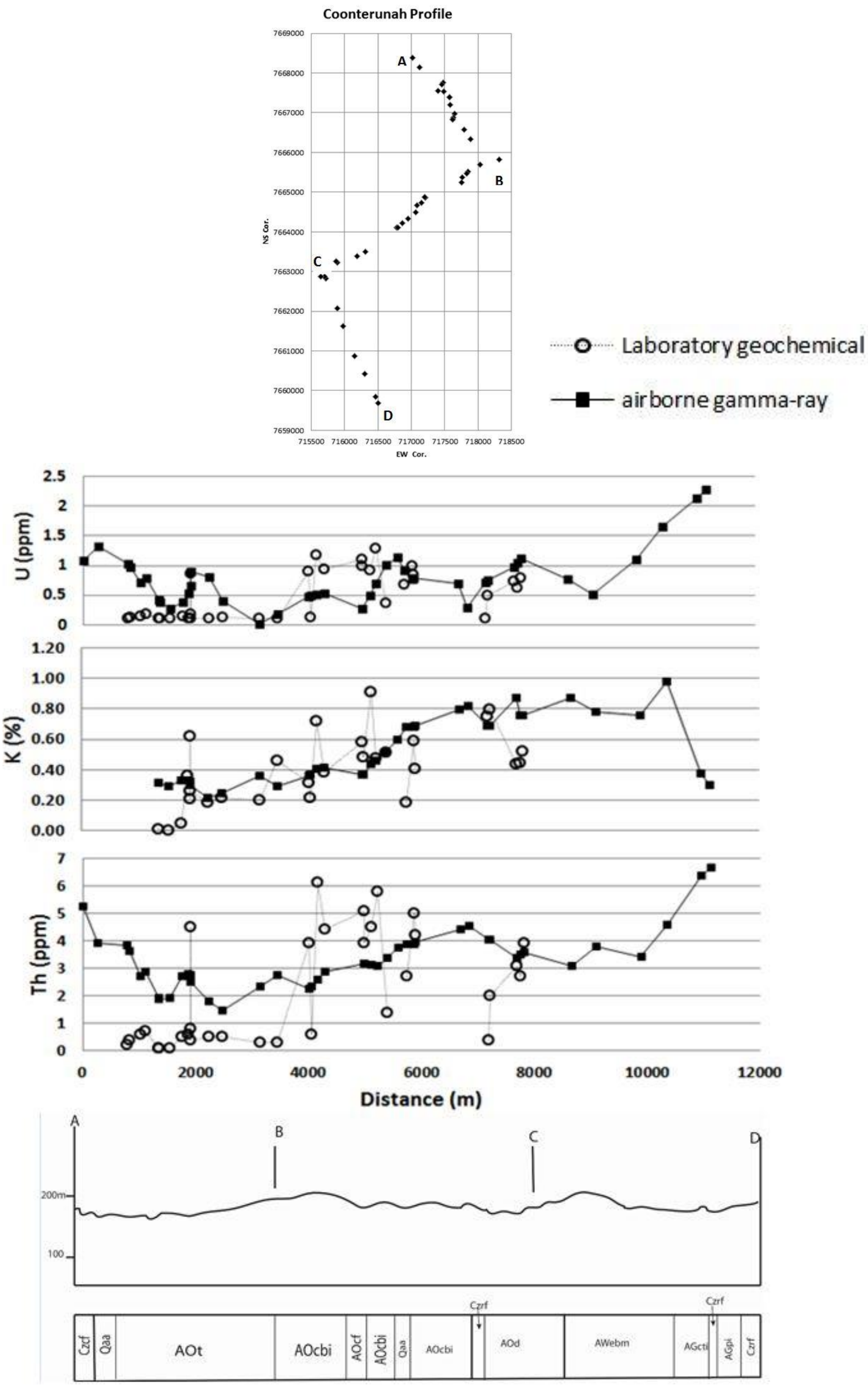

Appendix 5: Coonterunah transect box plot showing comparison of band ratio pixel value of resampled spectra used to select best lithology discriminating ratio.

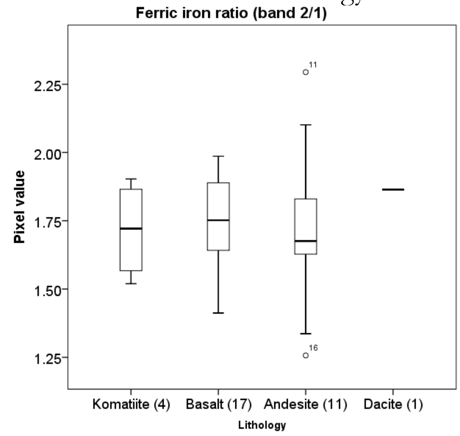

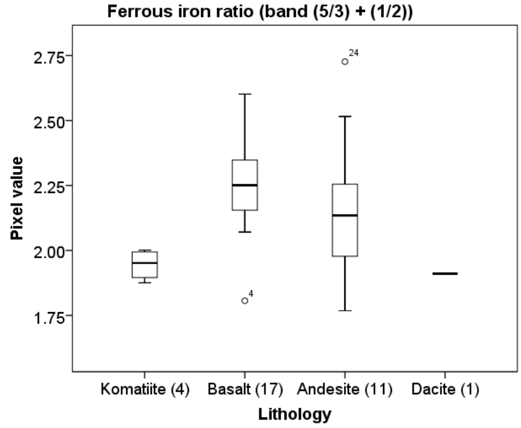

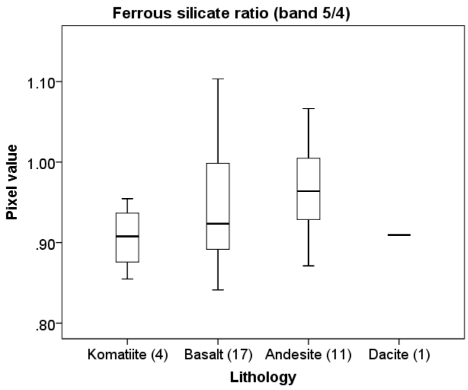

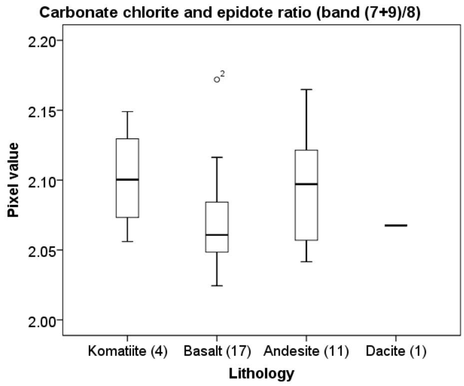

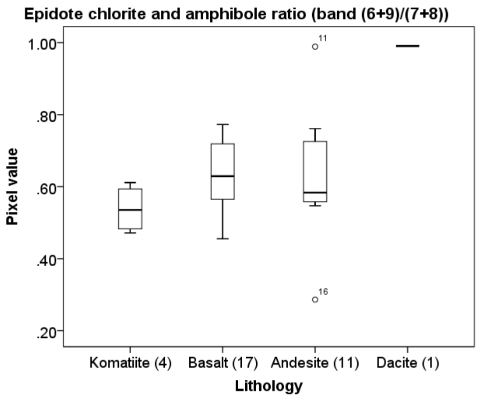

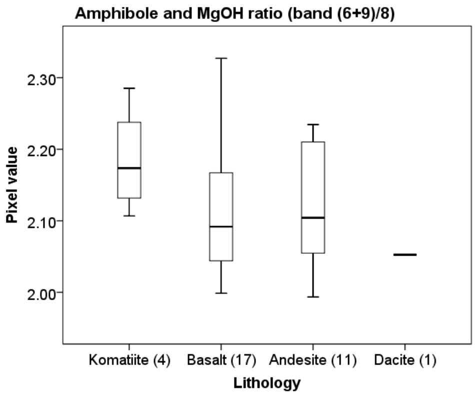

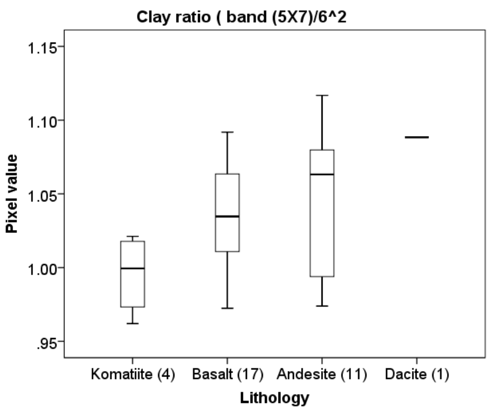

Appendix 6: Clay mineral distribution map of Coonterunah and Duffer transects.

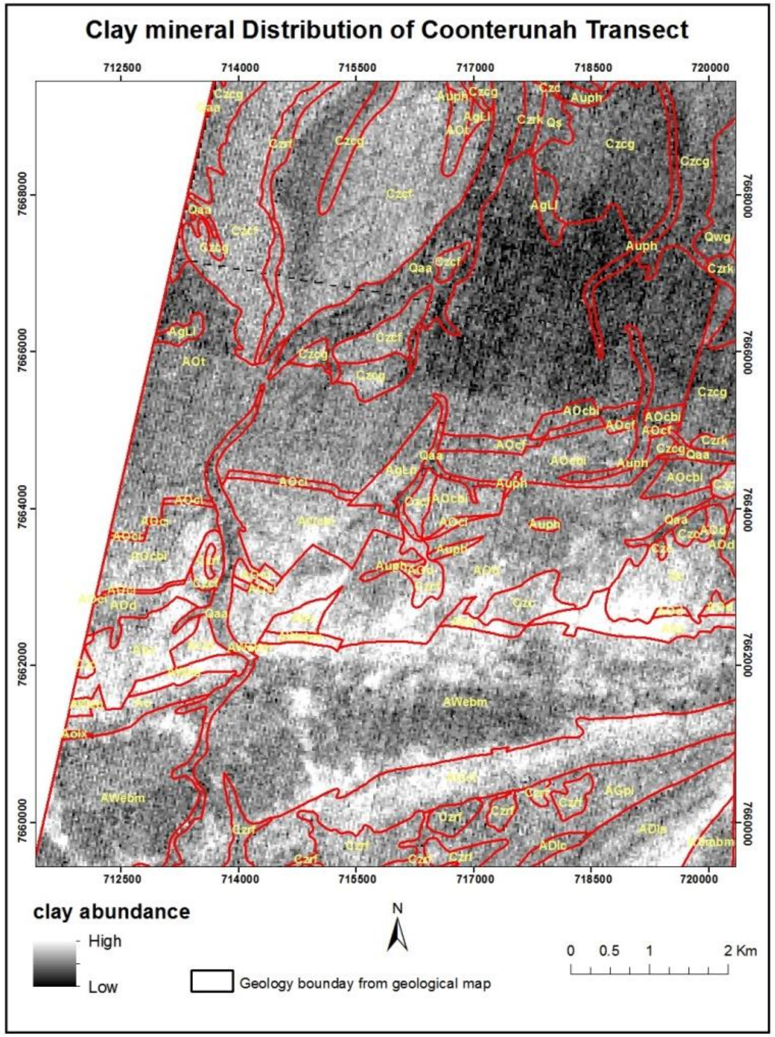

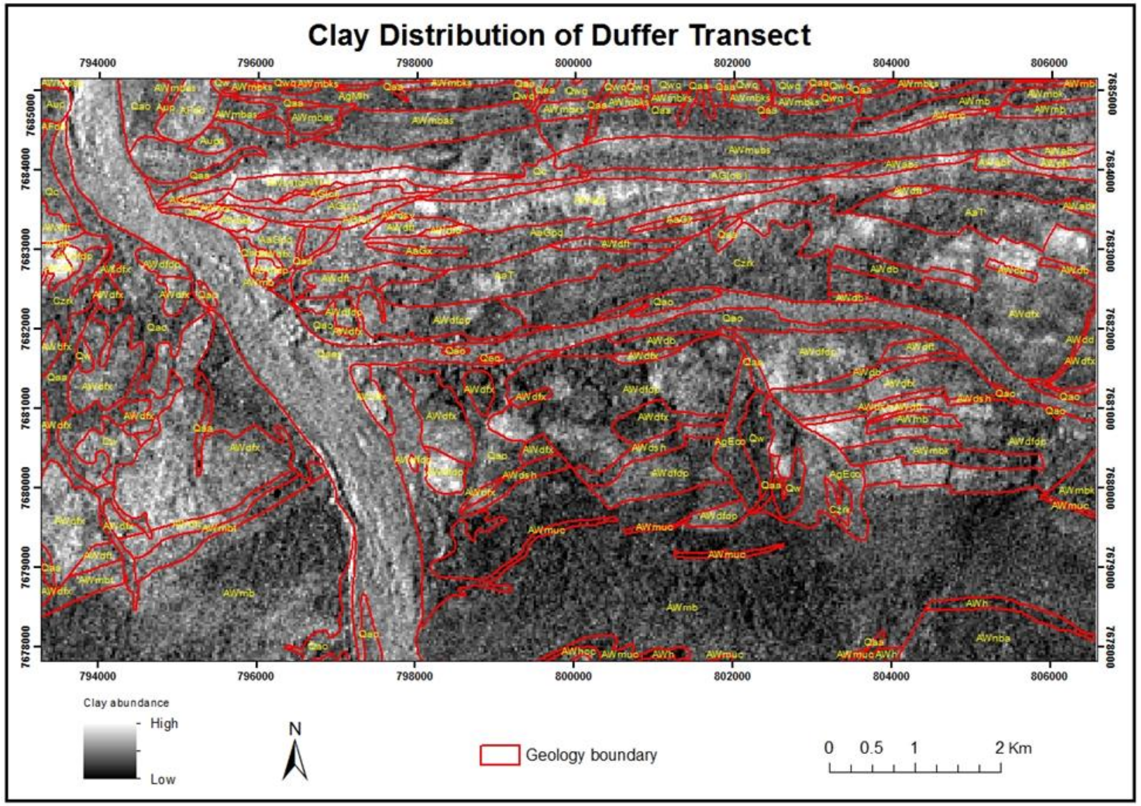

Appendix 7: Geological map and lithology code description table of Duffer transect

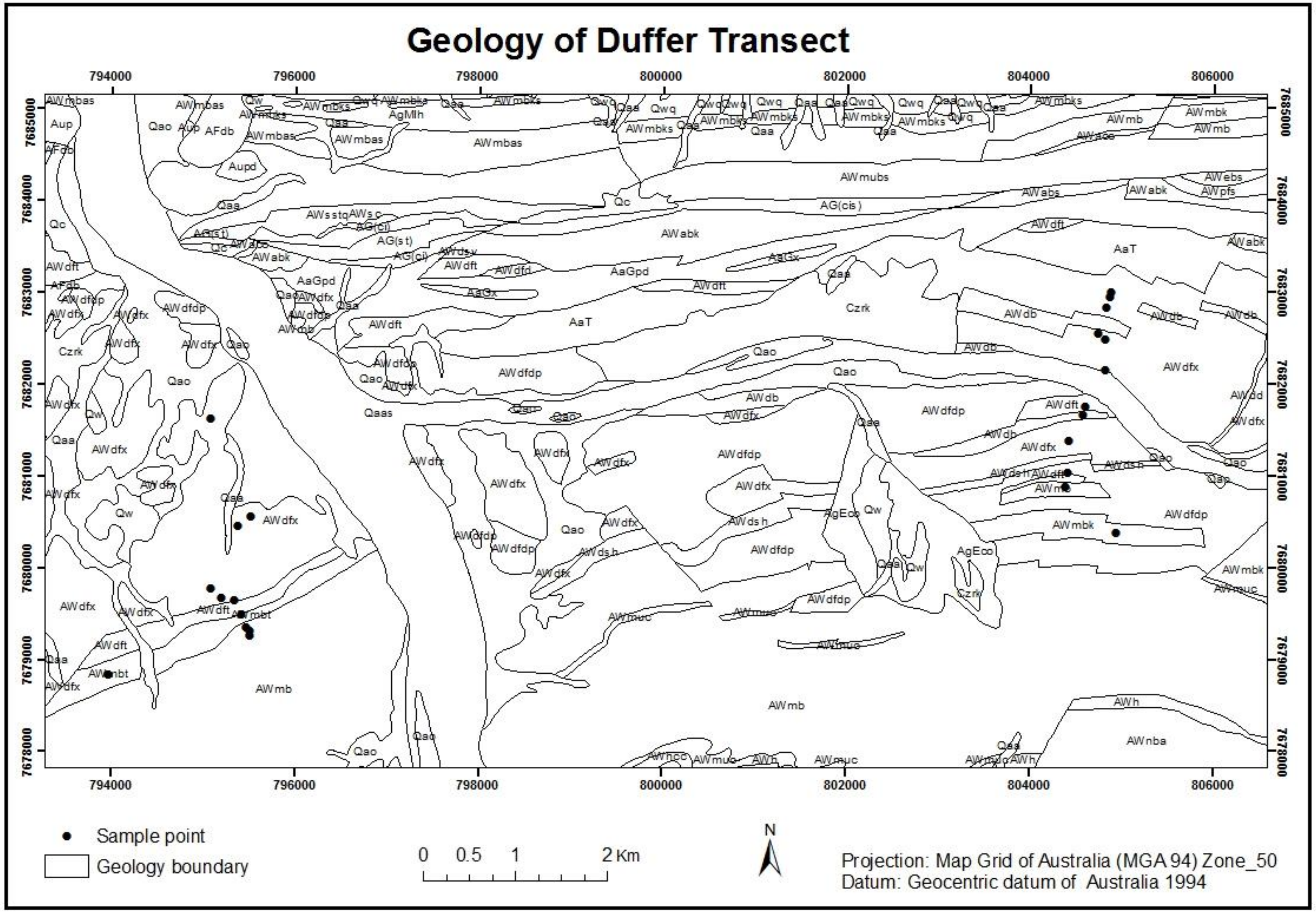

Subgroup	Formation	Symbol	Description
Soansville subgroup	Un assigned	Aup	Serpentinized metaperidotite and serpentine-chlorite schist
		Aupd	Serpentinized metadunite and serpentine schist
		Czrk	Calcrete; massive, nodular, and cavernous limestone; deviationorigin
		Qaa	Alluvial sand, silt, and gravel in broad creeks
		Qaas	Alluvial sand and gravel in river and creek channel beds
		Qao	Over bank deposits; alluvial sand, silt, and gravel on floodplains adjacent to main drainage channels and interchannel islands
		Qc	Colluvium - sand, silt, and gravel in outwash fans; scree and talus
		Qw	Low-gradient sheetwash deposits - silt, sand, and pebbles on distal outwash fans
	Bellary	AFdb	Dolerite and medium- to coarse-grained gabbro dykes
	Cleaverville	AG(ci)	Banded iron-formation interbedded with ferruginous chert and ferruginous shale
		AG(cis)	Sheared cherty banded iron-formation; white chert and limonitic layers
	Farrel quartize	AG(st)	Pebbly sandstone, blue-grey lithic arenite, and quartz arenite; turbiditic;
	Gap intrusion	AaGpd	Serpentinized metadunite and serpentine schist
		AaT	metagabbro and metapyroxenite
	Copping ganodiorite	AgEco	Massive to foliated, cream to pinkish, biotite granodiorite to tonalite; weakly foliated
	Euro basalt	AWebs	Strongly sheared chlorite schist
	Strelley pool	AWsc	Laminated grey and white chert; includes silicified chemical sedimentary rocks
		AWsstq	Thick-bedded, quartz-rich sandstone; minor chert; weakly metamorphosed
Salgash subgroup	Panorama	AWpfs	Quartz-sericite schist, derived from felsic volcanic rocks
		AWpft	Felsic tuff and volcaniclastic sandstone, including ash beds; well bedded; weakly metamorphosed
	Apex	AWabk	Komatiitic basalt; commonly pillowed; local pyroxene spinifex texture
Coongan sub group	Duffer	AWdb	Basalt; pillowed
		AWdd	Metadolerite and amphibolite, in dykes
		AWdfd	Dacite to andesite; local felsic schist
		AWdfdp	Feldspar porphyritic andesite to dacite; mainly subvolcanic intrusions
		AWdft	Felsic tuff and volcaniclastic rock; local greywacke, conglomerate, and jasper chert; thinly to moderately bedded; locally silicified
		AWdfx	Lithic volcaniclastic breccia and conglomerate; dacitic to andesitic.
		AWdsv	Dacite to andesite; local felsic schist
	Mt Ada basalt	AWmb	Basalt, undivided; includes local syn-volcanic dolerite intrusions
		AWnb	Basalt; generally massive; includes syn-volcanic dolerite intrusions; metamorphosed
		AWmbas	Amphibolite, strongly foliated to schistose; partly retrogressed to greenschist facies
		AWmbk	Komatiitic basalt; commonly pillowed; local pyroxene spinifex texture
		AWmbt	Mafic to felsic tuff; medium to fine grained; weakly metamorphosed
		AWmbks	Tremolite-chlorite-serpentine and chlorite-carbonate schist derived from komatiitic basalt
		AWmuc	Black-weathering carbonate-altered ultramafic rock; massive to schistose; metamorphosed
		AWmubs	Dismembered serpentinized metaperidotite in carbonate-chlorite-talc schist and mafic schist

Appendix 8: Duffer transect box plots showing comparison of potassium thorium and uranium contents measured with whole-rock laboratory geochemistry and airborne gamma-ray spectrometry.

<table>
<tr><th>Laboratory whole-rock geochemical data Box plot</th><th>Airborne gamma-ray data Box plots</th></tr>
<tr><th>Potassium</th><th>Potassium</th></tr>
<tr><td>
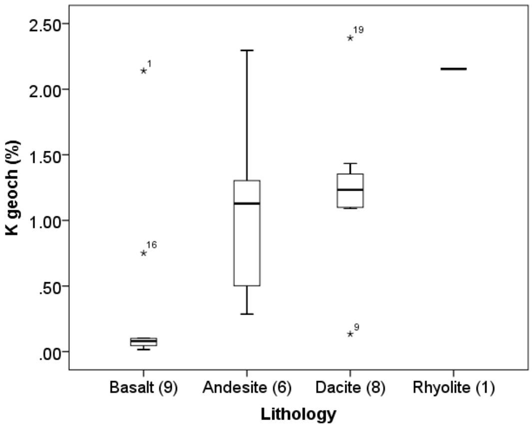

</td><td>
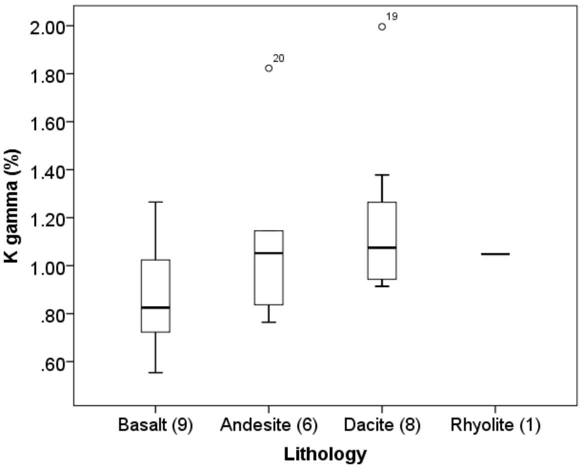

</td></tr>
<tr><th>Thorium</th><th>Thorium</th></tr>
<tr><td>
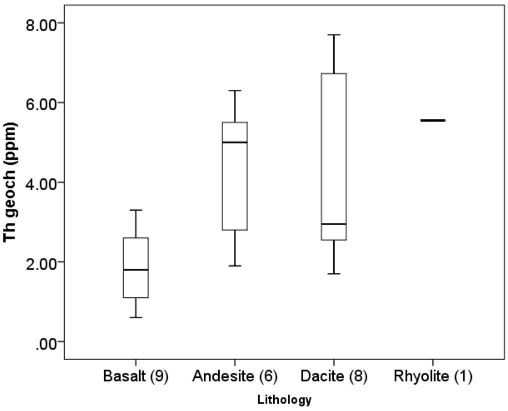

</td><td>
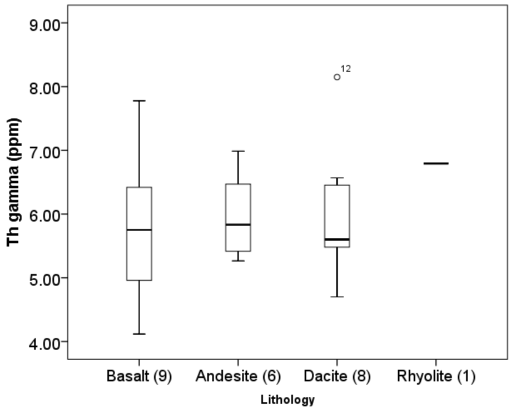

</td></tr>
<tr><th>Uranium</th><th>Uranium</th></tr>
<tr><td>
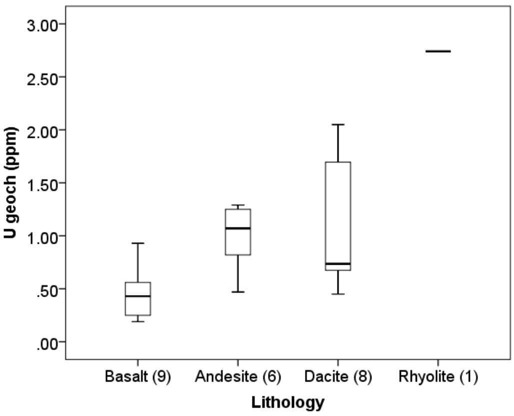

</td><td>
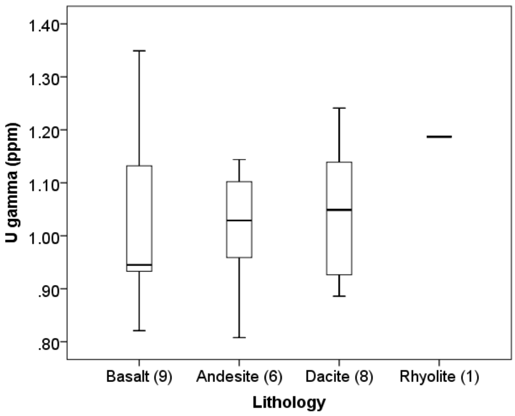

</td></tr>
</table>

Appendix 9; Thorium, potassium and uranium distribution map for Duffer transect with estimation classes.

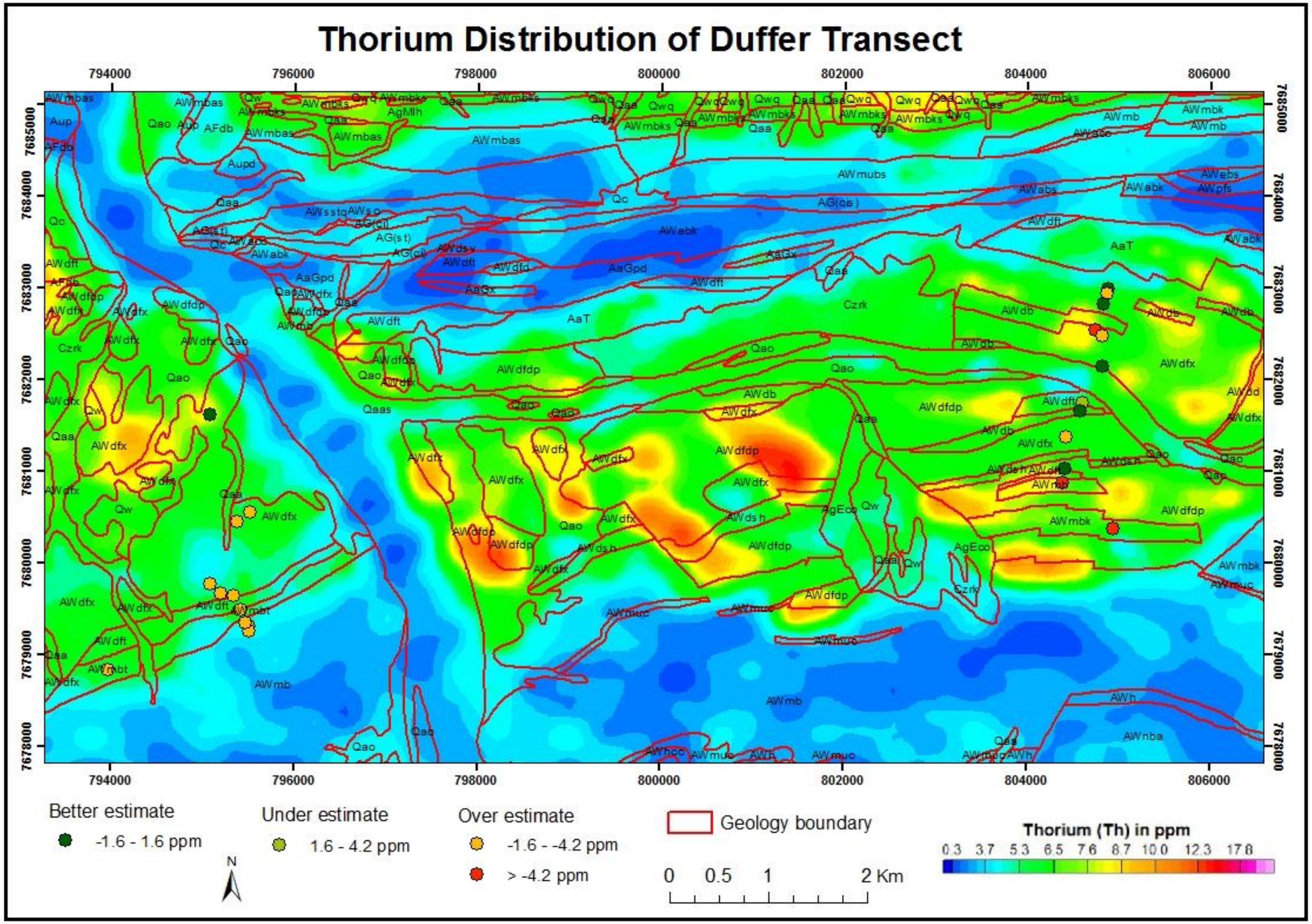
Thorium Distribution of Duffer Transect
794000
796000
798000
800000
802000
804000
806000
7678000
7679000
7680000
7681000
7682000
7683000
7684000
7685000
Better estimate
-1.6 - 1.6 ppm
Under estimate
1.6 - 4.2 ppm
Over estimate
-1.6 - -4.2 ppm
> -4.2 ppm
Geology boundary
0 0.5 1 2 Km
N
Thorium (Th) in ppm
0.3 3.7 5.3 6.5 7.6 8.7 10.0 12.3 17.8

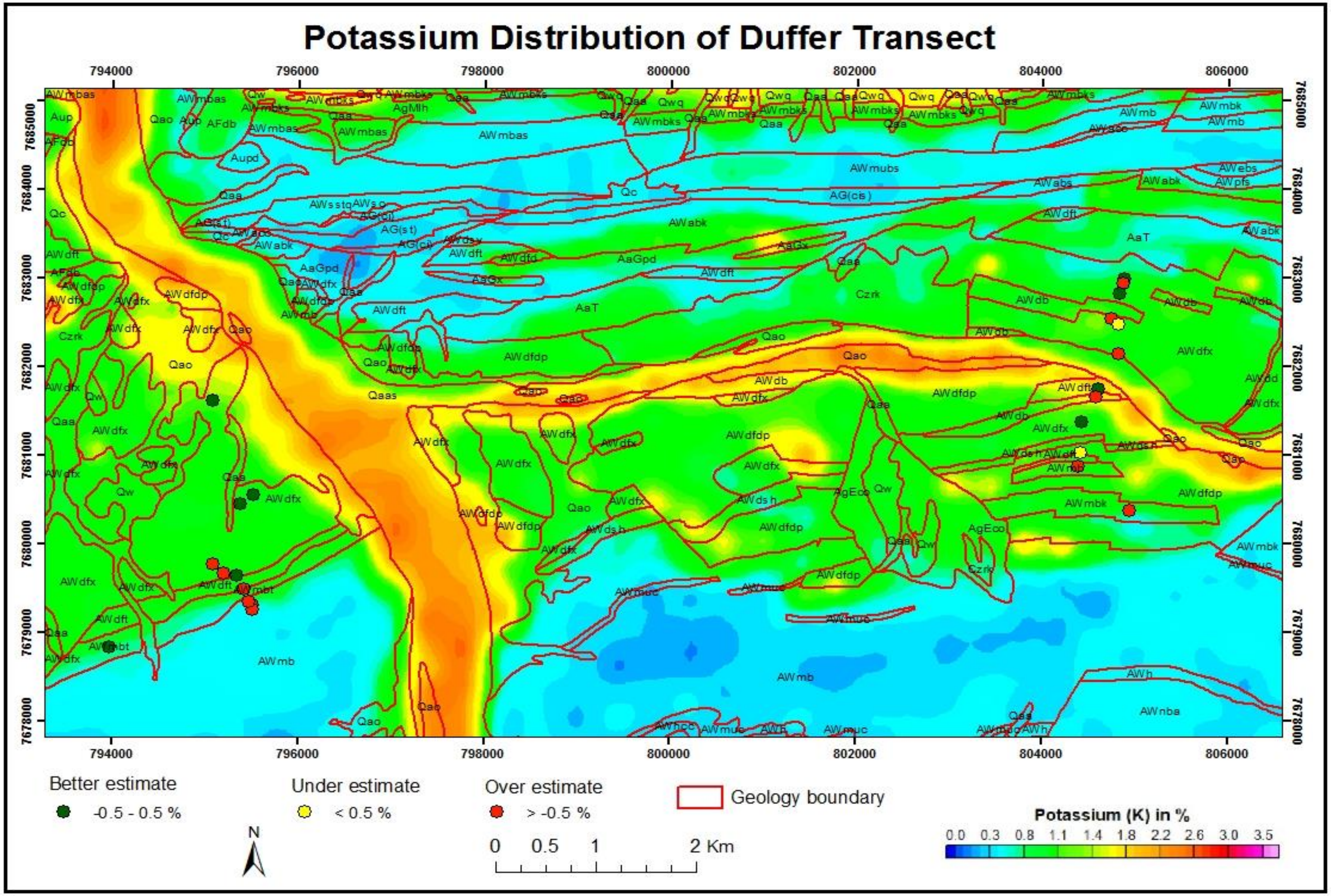
Potassium Distribution of Duffer Transect
794000
796000
798000
800000
802000
804000
806000
7685000
7684000
7683000
7682000
7681000
7680000
7679000
7678000
Better estimate
-0.5 - 0.5 %
Under estimate
< 0.5 %
Over estimate
> -0.5 %
Geology boundary
N
0 0.5 1 2 Km
Potassium (K) in %
0.0 0.3 0.8 1.1 1.4 1.8 2.2 2.6 3.0 3.5

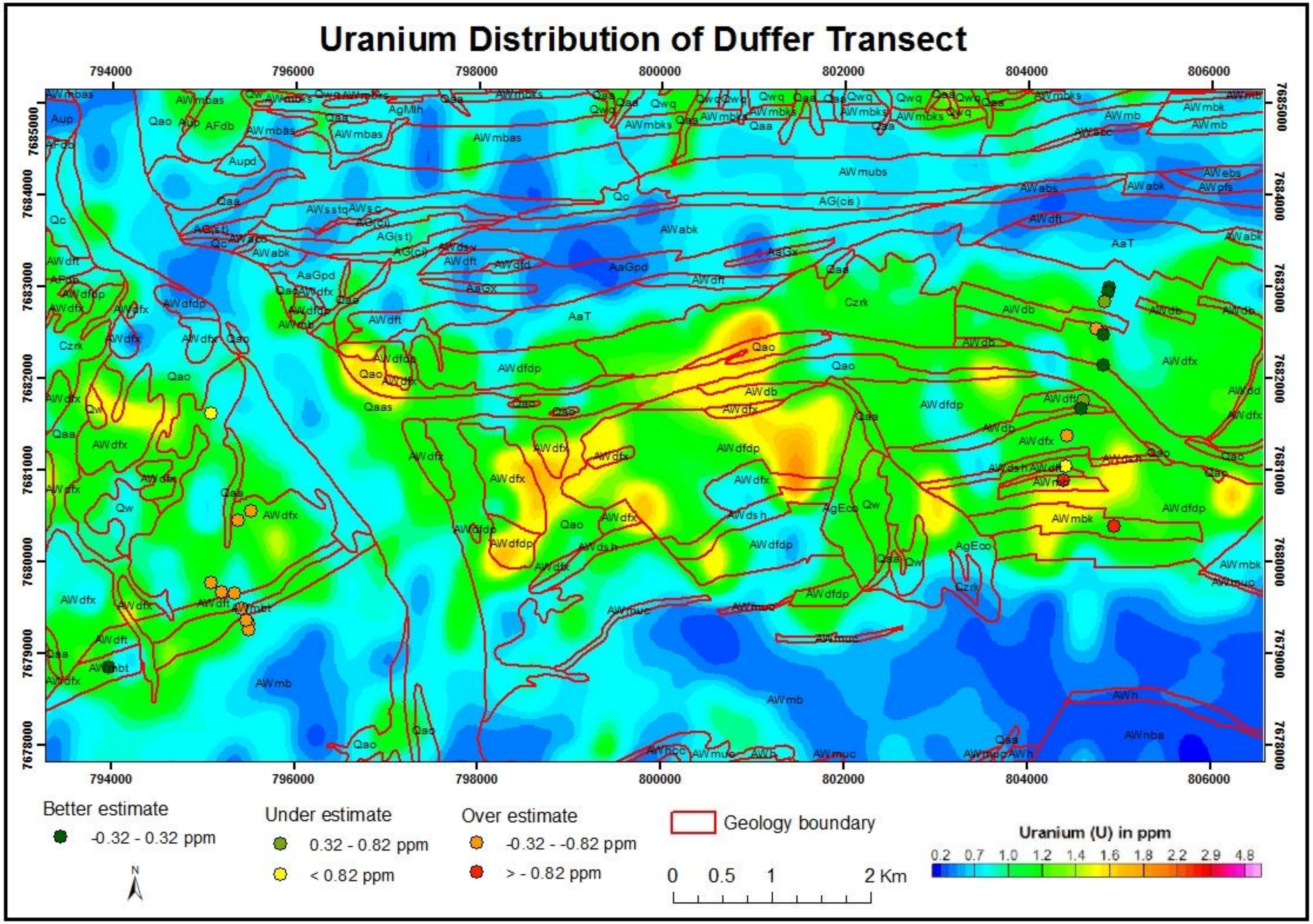
Uranium Distribution of Duffer Transect
Better estimate
-0.32 - 0.32 ppm
Under estimate
0.32 - 0.82 ppm
< 0.82 ppm
Over estimate
-0.32 - -0.82 ppm
> - 0.82 ppm
Geology boundary
0 0.5 1 2 Km
Uranium (U) in ppm
0.2 0.7 1.0 1.2 1.4 1.6 1.8 2.2 2.9 4.8
N

Appendix 10: Duffer profiles comparing for potassium thorium and uranium with relief.

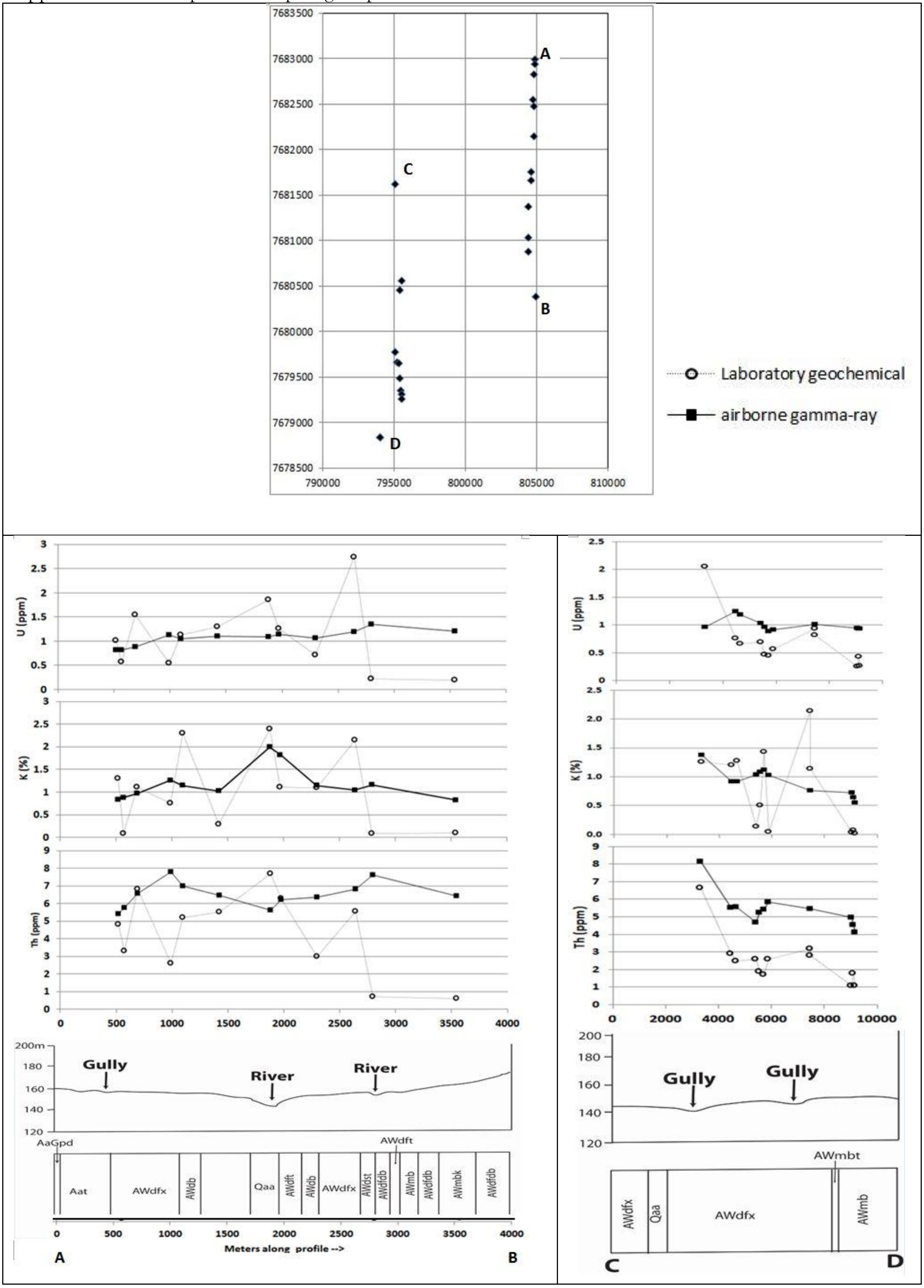

Appendix 11: Duffer transect box plot showing comparison of band ratio pixel value of resampled spectra used to select best lithology discriminating ratio.

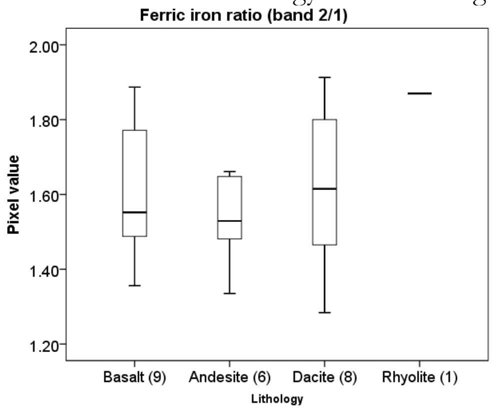

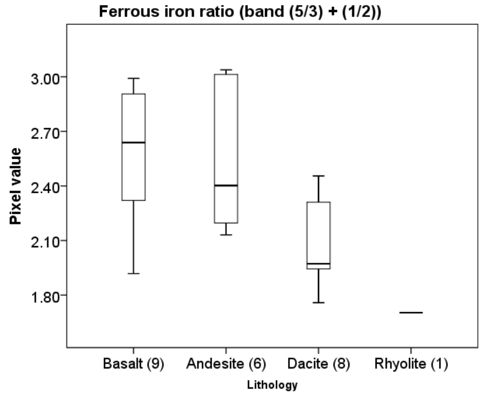

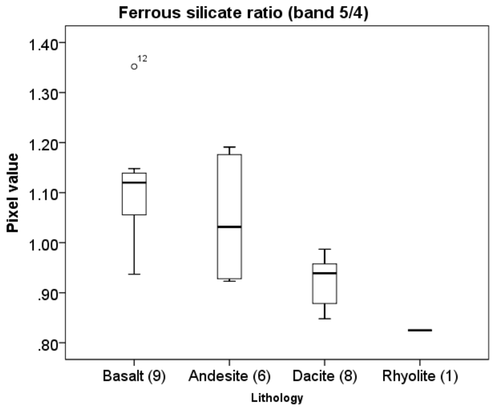

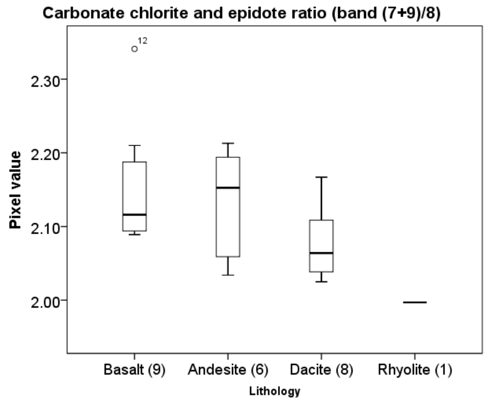

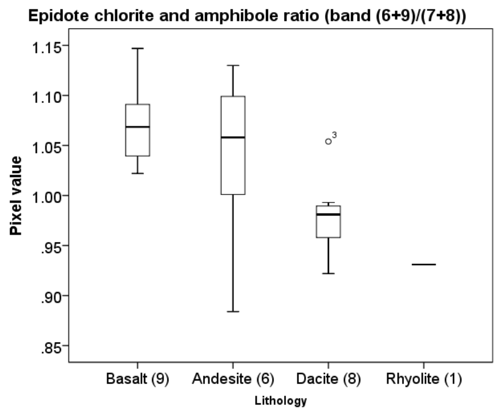

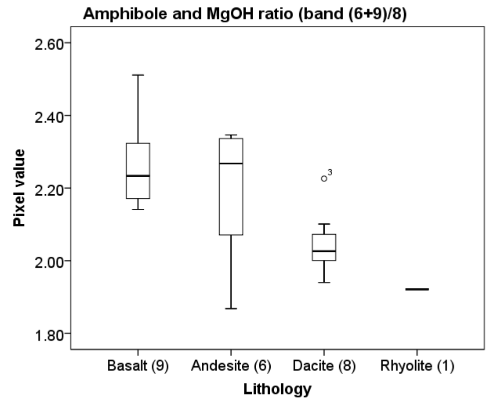

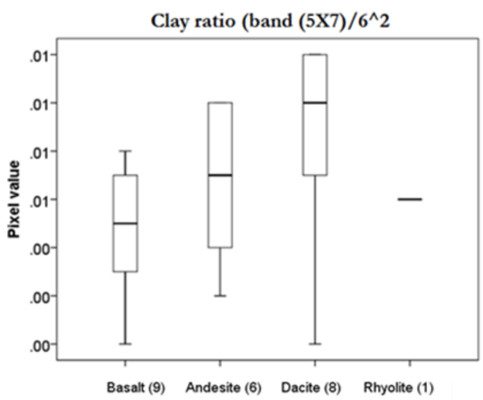

Appendix 12: Lithology description for Panorama, North Star, Apex, Mt Ada, Euro and Charteris transects.

Panorama transect	
Symbol	**Description**
Czc	Colluvium - clay, silt, and sand derived from adjacent rock outcrop; dissected and consolidated
Qaa	Alluvial clay, silt, sand, and gravel in main drainage channels
Qsg	Mixed eolian and eluvial sand - red-brown quartz sand in sheets; overlying and derived from granitoid rock
AWs	White, grey, and blue-black banded chert; local wavy laminated chert; minor felsic ash and massive blue-grey chert;locally stromatolitic; weakly metamorphosed
Aux	Metapyroxenite; includes metamorphosed diorite and dolerite
Aup	Metamorphosed serpentinized peridotite and serpentine-chlorite schist; local asbestos veins
AWecc	White, grey, and blue-black banded chert; local massive blue-grey chert; locally stromatolitic; metamorphosed
AWebk	Komatiitic basalt and minor tholeiitic basalt, massive and pillowed; metamorphosed
AWeb	Basalt, mostly pillowed; minor massive dolerite, gabbro, and komatiitic basalt; metamorphosed
AgOca	Biotite monzogranite, fine to coarse grained, sparsely feldspar porphyritic; common mafic xenoliths
AWpfa	Felsic agglomerate and minor tuff; locally silicified; weakly metamorphosed
AWpft	Felsic tuff and minor agglomerate; locally silicified, weakly metamorphosed

North Star transect	
Symbol	**Description**
A-WAm-fdvt	Dacitic volcaniclastic rock; tuffaceous, with accretionary lapilli; metamorphosed
_C2	Partly consolidated colluvial sand, silt, and gravel in proximal outwash fans; scree and talus; dissected by present-day drainage
_A1c	Sand, silt, and gravel in active drainage channels; includes clay, silt, and sand in poorly defined drainage courses on floodplains
_A1b	Sand, silt, and gravel in the beds of major active drainage channels
_R2-k	Deviationcalcrete; massive, nodular, and cavernous limestone; variably silicified; dissected by present-day drainage
A-WAh-xu-s	Ultramafic volcanic rocks, siliciclastic sedimentary rocks; basalt, and chert; local felsic volcanic rocks; metamorphosed
A-WAn-bb	Basalt; generally massive; includes syn-volcanic dolerite intrusions; locally schistose; metamorphosed
A-WAm-bb	Basalt; generally massive, but locally pillowed; local dolerite sills; metamorphosed
A-WAn-mbmz	Altered komatiitic basalt; widespread silicification and quartz veinlets
A-WAn-mutk	Talc-carbonate and chlorite-serpentine-carbonate schist; metamorphosed ultramafic volcanic rocks
A-WAn-bk	Komatiitic basalt, massive and pillowed lavas; local pyroxene spinifex texture; metamorphosed
A-WAm-bkd	Pillowed and variolitic komatiitic basalt; metamorphosed
A-WAh-ccb	Grey and white layered chert; local limonitic chert and felsic volcanic rocks; metamorphosed
A-WAh-mutk	Talc-carbonate and chlorite-serpentine-carbonate schist; metamorphosed ultramafic volcanic rocks
A-CLho-gnap	Porphyritic microgranite and microgranodiorite; mainly in subvolcanic intrusions; euhedral feldspar and quartz phenocrysts, typically in a dark grey, fine-grained to glassy matrix; metamorphosed
A-WAn-o	Dolerite and gabbro; metamorphosed
A-WAn-od	Dolerite; metamorphosed
A-WAn-mapt	Serpentinized peridotite; local pseudomorphed olivine-cumulate textures
A-WAn-mbmq	Silicified meta komatiitic basalt

A-CLho-gf	Alkali-feldspar granite; medium to coarse grained; includes local diorite and granodiorite; massive to weakly foliated; weakly metamorphosed

Mt Ada and Apex transects	
Symbol	**Description**
Qwb	Sheetwash clay and silt with gilgai (crabhole) surface; generally vegetated
Qaa	Alluvial sand, silt, and gravel in broad creeks
Qc	Colluvium - sand, silt, and gravel in outwash fans; scree and talus; proximal mass wasting deposits
Qw	Low-gradient sheetwash deposits - silt, sand, and pebbles on distal outwash fans; no defined drainage
Aux	Metapyroxenite; massive, coarse grained
AWabks	Tremolite-chlorite-serpentine schist derived from komatiitic basalt
AWauk	Metakomatiite
AWacc	Grey, white, and blue-black layered chert; weakly metamorphosed
AWabk	Komatiitic basalt; commonly pillowed; local pyroxene spinifex texture; weakly metamorphosed
AWdsvc	Volcanogenic sandstone with cherty siltstone tops; carbonate cemented; turbiditic; weakly metamorphosed
AWmbk	Komatiitic basalt; commonly pillowed; local pyroxene spinifex texture; weakly metamorphosed
AWmbk	Komatiitic basalt; commonly pillowed; local pyroxene spinifex texture; weakly metamorphosed
AWtm	Marble Bar Chert Member: grey, white and red layered chert; weakly metamorphosed
AWtm	Marble Bar Chert Member: grey, white and red layered chert; weakly metamorphosed

Euro transect	
Symbol	**Description**
_A1c	Sand, silt, and gravel in active drainage channels; includes clay, silt, and sand in poorly defined drainage courses on floodplains
_A1f	Floodpain deposits; sand, clay, and gravel adjacent to main drainage channels
_C1	Colluvial sand, silt, and gravel in outwash fans; scree and talus; proximal mass-wasting deposits; unconsolidated
_R2-k	Deviationcalcrete; massive, nodular, and cavernous limestone; variably silicified; dissected by present-day drainage
_W1	Silt, sand, and pebbles in distal sheetwash fans; no defined drainage
A-BL-od	Dolerite dyke; local gabbro; weakly metamorphosed
A-DA-mats	Serpentinite, schistose
A-EMna-gge	Biotite-hornblende granodiorite to tonalite; equigranular; contains inclusions of Tambina Supersuite tonalite; metamorphosed
A-FOr-bbg	Massive porphyritic vesicular and amygdaloidal basalt; some pillow basalt
A-GC-s	Sandstone, siltstone, conglomerate, shale, chert, and banded iron-formation; metamorphosed
A-KEe-bb	Massive basalt; metamorphosed
A-KEe-bbo	Pillowed basalt; includes local massive basalt, dolerite, and komatiitic basalt; metamorphosed
A-KEe-bk	Komatiitic basalt, massive and pillowed lavas and subvolcanic intrusions; local pyroxene spinifex texture; metamorphosed
A-KEe-cc	Chert; metamorphosed
A-KEe-mbms	Mafic schist derived from komatiitic basalt
A-KEe-mbq	Silicified metamafic volcanic rock

A-KEe-mutk	Talc-carbonate rock derived from metamorphosed peridote; includes volcanic protoliths.
A-KEw-bko	Pillowed komatiitic basalt; metamorphosed
A-KEw-cc	Chert; metamorphosed
A-KEw-fnt	Felsic volcanic sandstone; tuffaceous; local quartz sandstone; metamorphosed
A-KEw-fr	Porphyritic rhyolite and rhyodacite; local felsic volcaniclastic rocks; metamorphosed
A-PIs-cc	White, grey, and blue-black layered chert; mainly silicified carbonate rocks; local sandstone and felsic volcaniclastic rocks; locally stromatolitic; metamorphosed
A-WAa-bb	Basalt; tholeiitic and massive; commonly pillowed and locally schistose; metamorphosed
A-WAa-bbo	Pillowed and massive basalt; includes minor dolerite; metamorphosed
A-WAa-bk	Komatiitic basalt, massive and pillowed lavas and subvolcanic intrusions; local pyroxene spinifex texture; metamorphosed
A-WAa-cc	Chert; metamorphosed
A-WAa-mbbq	Silicified metabasalt
A-WAa-mbbs	Strongly sheared chloritic schist after metabasalt
A-WAa-mutk	Talc-carbonate rock derived from metaperidote; includes volcanic protoliths
A-WAa-mwa	Medium-grained amphibolite and amphibolitic schist; derived from basalt and dolerite
A-WAa-xmwa-g	Interlayered amphibolite and granitic rocks; commonly schitose; includes granite and pegmatite veins
A-WAp-fnv	Felsic volcaniclastic rock; includes debris-flow deposits, autobreccia, agglomerate, and tuffaceous rocks; minor chert; local basaltic andesite; metamorphosed
A-WAp-mus	Ultramafic schist

Apex transect	
Symbol	**Description**
Qaas	Unconsolidated sand, silt, and gravel in discrete channel beds
Qwg	Sheetwash sand and quartz pebbles overlying and derived from granitoid rocks
Qls	Mixed lacustrine and eolian deposits; clay, silt, and sand
Qaa	Alluvium - undivided clay, silt, sand, and gravel in rivers and creeks
Czak	Calcrete - massive, nodular, and cavernous limestone, variably silicified; dissected valley calcrete
Qao	Over bank deposits - alluvial sand, silt, and clay on floodplains adjacent to main drainage channels
Qrg	Quartzofeldspathic eluvial sand, with quartz and rock fragments; overlying and derived from granitoid rock
Czag	Consolidated alluvial gravel, sand, and silt; local carbonate cement; dissected
Qc	Colluvium - sand, silt, and gravel on outwash fans; scree, talus; proximal mass-wasting deposits
q	Quartz vein, various ages
PLgh	Horrnblende monzogranite and granodiorite; in small plutons
AFdb	Black Range Dolerite suite: dolerite and medium- to coarse-grained gabbro dykes; weakly metamorphosed
AgMx	Foliated to gneissic granitoid rock with mafic and ultramafic xenoliths
AFk	Massive, vesicular and amygdaloidal basalt and andesite
AFka	Basaltic agglomerate
AGo	Pillowed and massive basalt, hyaloclastic breccia, and silicified basaltic andesite; metamorphosed
AGn	Banded iron-formation, jaspilite, banded and ferruginous chert, and black carbonaceous shale; metamorphosed
AGna	Basal pebble to cobble conglomerate, sandstone, siltstone, and shale; metamorphosed

AWba	Fine- to medium-grained amphibolite, and mafic hornfels; after basalt
AFr	Massive, porphyritic, vesicular and amygdaloidal basalt; some pillow basalt
AFrs	Basal, polymictic pebble conglomerate and sandstone
AGd	Fine- to coarse-grained metadolerite sills
Apd	Quartz-feldspar porphyry; dacite and rhyodacite; metamorphosed
AGu	Weathered brown, grey-green shale, siltstone, lithic wacke, sandstone, and pebble conglomerate; local polymicitic, matrix-supported conglomerate; metamorphosed
AaGus	Serpentinite; after peridotite
AaGx	Metapyroxenite
AFhb	Massive and flow-banded porphyry, porphyry breccia, bedded tuffaceous rocks, and quartz-feldspar and feldspar porphyry
AFha	Medium- to very coarse-grained feldspathic sandstone, pebbly sandstone, and conglomerate; minor fine-grained sandstone and siltstone
AFhc	Polymictic, matrix-supported cobble to boulder conglomerate, sandstone, siltstone, and wacke
Agh	Hornblende monzogranite and granodiorite
AFhu	Tuffaceous sandstone, siltstone and shale, accretionary lapilli and felsic tuff, and some feldspathic sandstone, pebbly sandstone, and conglomerate; thin carbonate units
AWeq	Quartzite, green fuchsitic quartzite, chert, banded chert, and intercalated ultramafic schist
AWeu	Talc-chlorite schist (mylonitic fabric), pods of altered komatiitic basalt (spinifex texture locally), and carbonate-talc-fuchsite rock
AWe	Basalt, pillow basalt, high-Mg basalt, and intercalated thin-bedded chert; metamorphosed
AWes	Serpentinite (after peridotite) and tremolite-chlorite-serpentine-carbonate rock (after komatiite); sheared
AWec	Thin-bedded chert, ferruginous chert, and banded chert; metamorphosed
AWea	Sandstone, siltstone, shale, and tuffaceous sandstone; metamorphosed
AWpc	Thin-bedded chert, banded chert, and interlayered felsic tuff; metamorphosed
AWp	Felsic volcanic rocks; mainly rhyolite, quartz-feldspar porphyry, and felsic tuff; metamorphosed
AWac	Grey-white banded chert and green-grey fuchsitic quartzite; metamorphosed
AWa	Mixed, massive and pillowed basalt, high-Mg basalt, and thin intercalated chert; metamorphosed
AWau	Tremolite-serpentine-talc-carbonate rock; after peridotite and komatiite
AWaf	Felsic volcanic flows and tuff; mainly rhyolite; metamorphosed
AWoh	Hornblende-plagioclase schist; after dolerite intrusions; restricted to Duffer Formation
AWd	dacitic, rhyodacitic and andesitic lava, tuff, and agglomerate; metamorphosed
AWdd	Fine-grained amphibolite; after basalt and dolerite; metamorphosed
AgEco	Massive to seriate, cream to pinkish, biotite granodiorite, and tonalite; weakly foliated
AgEcox	Granitoid rock with mafic and ultramafic xenoliths